Synthesis and Characterization of Anti-Perovskite Structured Li^+ Conducting Solid State Electrolyte

SUGUMAR MANOJ KRISHNA

2021

TABLE OF CONTENTS

Chapter 1

Introduction

1.1 Challenges in energy storage and consumption

Energy is one of the most important requirements to ensure day-to-day human activities. The major source of global energy production is fossil fuels, out of which coal, natural gas, and petroleum are the most commonly used fuels to generate energy. The recent statistical review of world energy reports shows that the global energy demand grew by 2.9%, and carbon emissions grew by 2.0% faster than the previous year [1]. Coal-fired power generation has fallen in the last few years, as the cheapest fossil fuel will continue to play an essential role as a significant source of energy generation in the world. However, coal as end-use energy will result in low energy efficiency and increased environmental pollution.

Further, the oil and natural gas resources show different trends with oil entering into the steady-state, and the natural gas is heading to an end. According to the statistics reports, the primary energy source contributing to the global energy consumption (Figure. 1.1) was oil (33.1%), whereas coal (27.2%) and natural gas (23.9%) being the second and third prominent sources of energy generation. Issues on global warming and recent climate changes connected with high toxic emissions from fossil fuel combustion and other non-renewable energy sources have forced the researchers to emphasize sustainable energy production from wind, solar, biomass, and hydroelectricity as auxiliary to the polluting oil resources [2]. Therefore, renewable resources as an alternative energy source for automotive applications are prime focuses of research worldwide. Nevertheless, these renewable sources of electricity pose technical challenges when integrated into a large-scale transmission network and storage. The dependence and increased consumption of fossil fuels create concerns regarding depleting fuel reserves, the need for reduced CO_2 emissions, and rising oil prices.

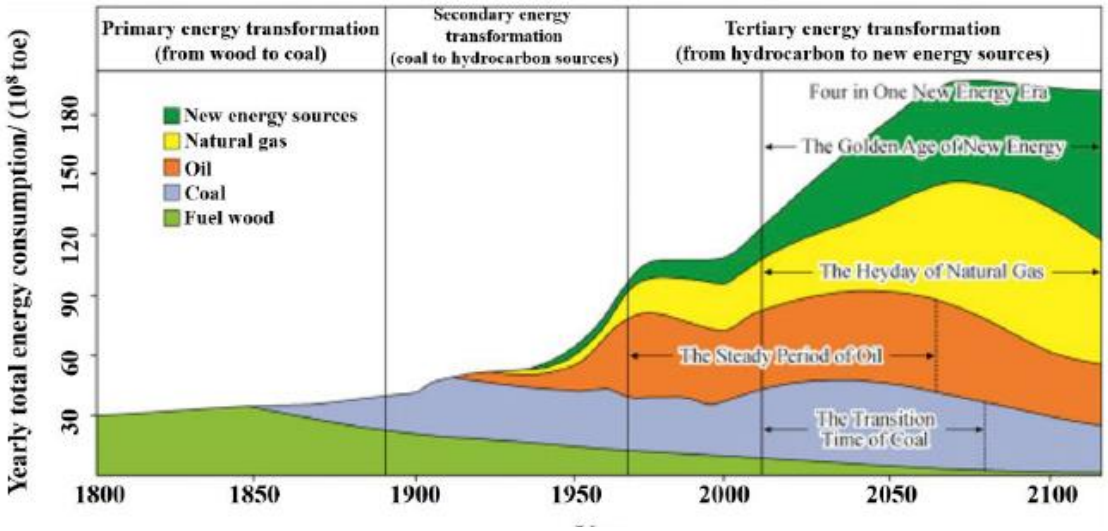

Figure 1.1 Trends and forecasts of global energy consumption. [1].

Some of these concerns can be solved through the development of electric vehicles. However, the successful implementation of electric vehicle technologies is dependent on the development of advanced rechargeable batteries with improved energy densities and performances. In addition to enabling electric transportation systems, the advancement of energy storage can also aid in developing renewable energy technologies such as wind and solar. Advanced rechargeable batteries can hence be envisioned to play a significant role in securing our future energy needs.

Figure 1.2 shows the volumetric energy density against gravimetric energy density for commercially available rechargeable batteries, that is, lead-acid, nickel/cadmium (NiCd), nickel-metal hydride (Ni/MH), and lithium-ion (Li^+) batteries (LiBs). Among them, LiBs have the highest gravimetric and volumetric energy densities. These advantages lead to lightweight and small-sized energy storage, and then LiBs have been widely used in various devices such as smartphones, laptop PC, electric vehicles, etc. The data in Fig. 1.2 is reported in 2013, and the energy density of LiBs has been improved year by year. For example, Tesla Model 3 has applied a 2170-type cylindrical type battery (diameter: 21 mm, length: 70 mm) manufactured by Panasonic, and the volumetric energy density of the cell is over 700 Wh L^{-1}. Further improvement of the energy density has been carried out by manufacturing a larger-sized 4680-type battery. Of course, it is important to develop alternative electrode and electrolyte materials to improve the energy density of LiBs [4,5].

1.2 Introduction to Li-ion batteries and all-solid-state Li-ion batteries

LiBs uses Li-insertion electrodes for both cathode and anode materials. The typical cathode material is $LiMO_2$ (M = Co, Ni, Mn), and the typical anode one is graphite. The charge-discharge reactions of LiBs are back and forth of Li^+ movement between the two electrode materials. At the charging process, Li^+ is extracted from the cathode via the oxidation process of Li-host material and the reduction process of graphite. At the discharging process, a reverse

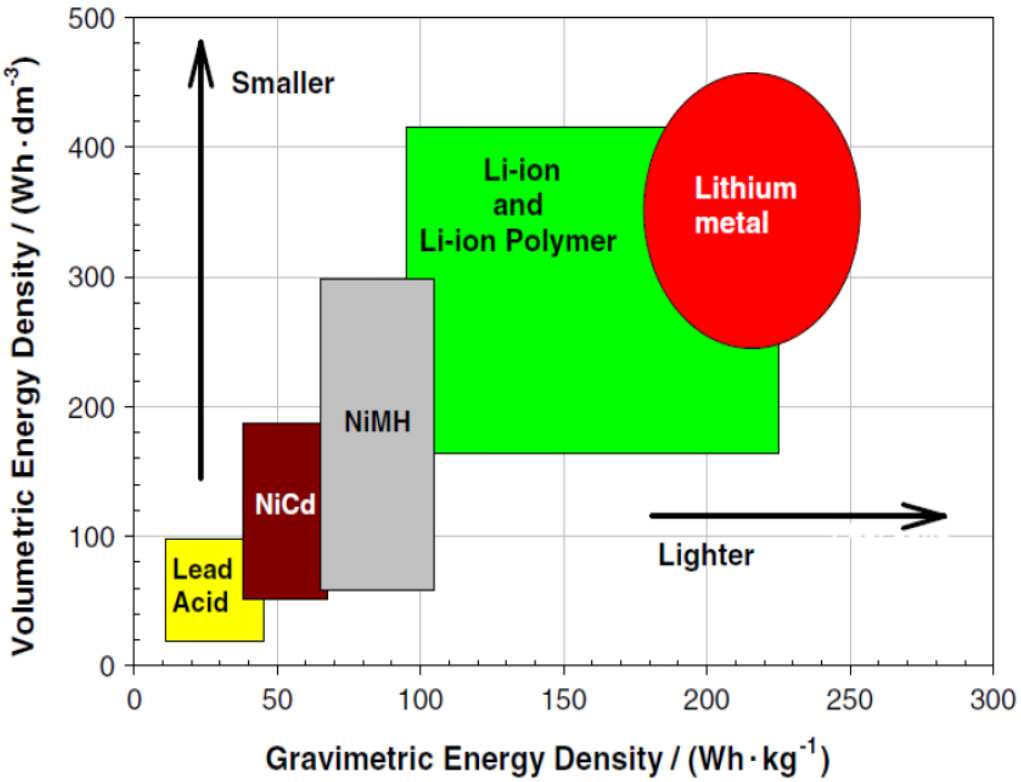

Figure 1.2 Volumetric energy density vs gravimetric energy density of commonly used rechargeable batteries [3].

reaction takes place. During those oxidation/reduction processes, the electron flow external circuit is shown in Fig. 1.3.

Commercialized LiBs apply volatile liquid electrolytes, where lithium salts such as lithium tetrafluoroborate ($LiBF_4$), lithium hexafluorophosphate ($LiPF_6$), etc., are dissolved in organic liquid solvents such as ethylene carbonate (EC), dimethyl carbonate (DMC), etc. [6]. Thus, the LiBs must be sealed tightly in packages to protect the liquid leakage, which inevitably increases the weight and the volume of materials unrelated to the charge and discharge reactions of the battery. Therefore, it is reasonable to enlarge the battery pack size to improve the energy density mentioned above. However, the liquid electrolyte is flammable, and then safety problems always remain unsolved. In fact, we often see news about accidents caused by the ignition of Li-ion batteries. In addition, liquid electrolyte easily reacts with the electrode material and then degrade the battery performance, and this side reaction is accelerated at a higher temperature. This is a crucial problem for the LiBs used in electric vehicles because electric vehicles flow large currents for the charging and discharging process and then provide significant Joule heating. Thus, a cooling system is always required for the LiBs module in electric vehicles. However, the energy density of the battery system decreases with the installation of a cooling system.

Due to all the drawbacks of the LiBs, all-solid-state Li-ion batteries (ASSBs) using oxide-based solid electrolytes have been expected as next-generation rechargeable batteries. Three essential advantages of ASSBs attract people's attention. The first advantage is safety because the oxide-based solid electrolyte is basically non-flammable. The second advantage is energy density. Usage of the solid electrolyte can simplify battery packing. A typical example is a multilayered battery package, which reduces the amount of current collector, thus making it higher energy density. Also, solid electrolyte itself can work as a hard separator. Then, there is a possibility of applying high-capacity electrode materials such as Li metal and Si, which

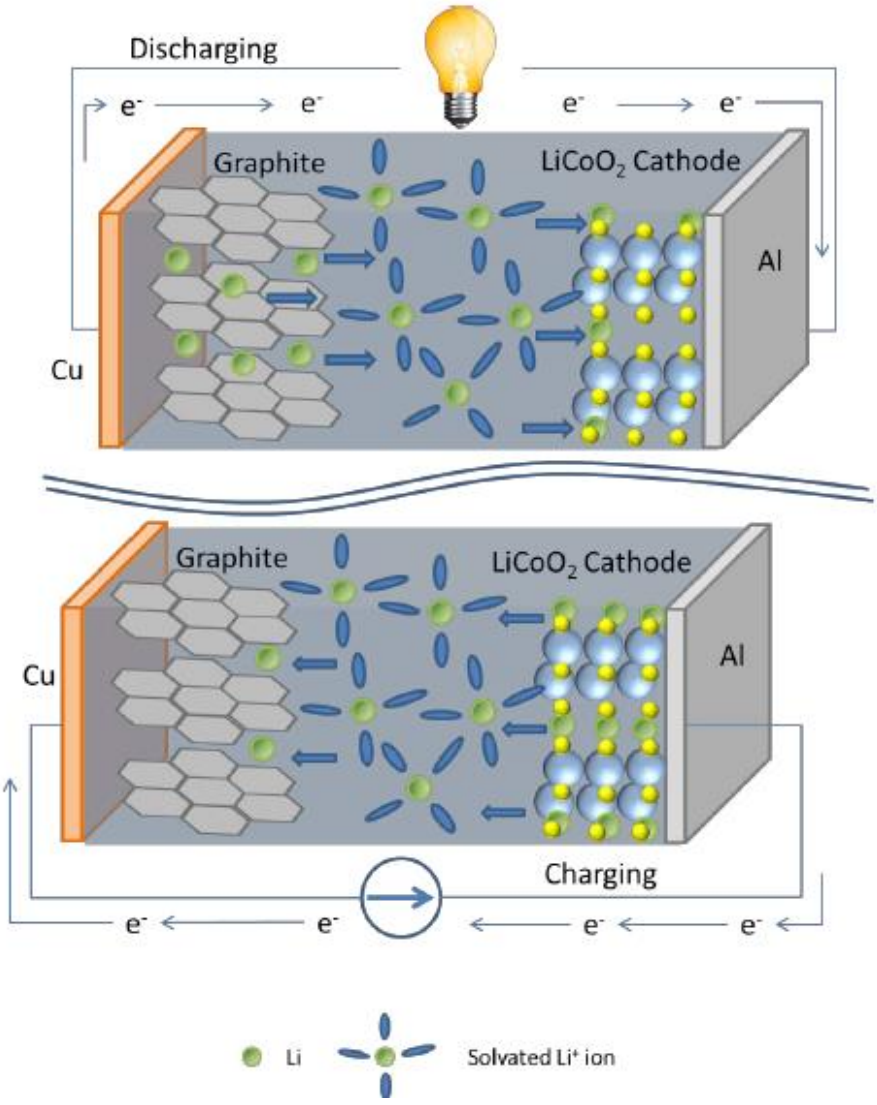

Figure 1.3 Schematic reaction image of LiB [7].

are difficult to use in LiBs. The third is stability. The solid electrolyte does not react with electrode material easily as compared with the liquid electrolyte. This advantage improves the lifetime of the battery even at a higher temperature. For example, thin-film type ASSBs can repeat over 10,000 times charge-discharge reactions without apparent capacity degradation.

1.3 Li^+ conduction in solid electrolyte

Two kinds of conduction typically influence ion conduction in the solid electrolyte: in-grain conduction and grain boundary conduction.

1.3.1 In-grain conduction

According to Ohm's law, the ionic conductivity relates the current density i_0 to the applied electric field **E**. The mobile-ion current density in the different principal crystallographic directions can be expressed in a scalar form as

$$i_0 = \sigma_i \mathbf{E} = c_i q v \quad (1)$$

Where v is the mean velocity of the mobile ions of charge q and c_i is their concentration. From the definition of the charge-carrier mobility $u \equiv v/\mathbf{E}$,

$$\sigma_i = c_i q u_i \quad (2)$$

According to the Nernst-Einstein relationship, u is related with diffusion constant, D, as follows

$$u_i = qD/kT \quad (3)$$

where k is Boltzman constant. As a consequence, (2) is rewrite as follows

$$\sigma_i = c_i q u_i = c_i q(qD/kT) \quad (4)$$

The diffusion coefficient is written as follows

$$D = D_0 \exp(-\Delta G_m/kT) \quad (5)$$

Here, D_0 is a pre-exponential factor, and ΔG_m is energy for ion migration between the sites in the crystal. The ΔG_m is related to motional enthalpy (ΔH_m) and vibrational enthalpy (ΔS_{vib})

$$\Delta G_m = \Delta H_m - T\Delta S_{vib} \quad (6)$$

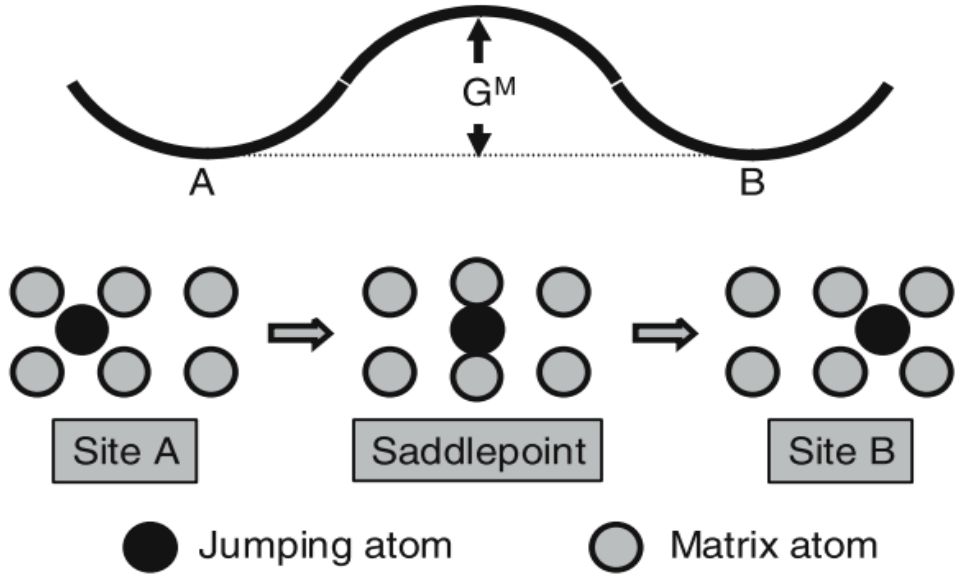

Figure 1.4 Atomic jump process in a crystalline solid: the black atom moves from an initial configuration (left) to a final configuration (right) pushing through a saddle point configuration (middle) [9].

Substitution of equations (6) and (5) into (4) gives

$$\sigma_i = D_0 (c_i q^2/kT) \exp(\Delta S_{vib}/k) \exp(-\Delta H_m/kT) = A \exp(-E_a/kT) \quad (7)$$

Here, ΔH_m is experimentally observed activation energy, E_a, for ion conduction. The ΔH_m is

$$\Delta H_m = E_m + P\Delta V \quad (8)$$

E_m is elastic strain energy where the ion needs to strain the lattice for the migration, especially around the saddle point, and $P\Delta V$ is the energy for the volume change due to the expanding the framework for ion migration. Besides the saddle point, an open space for Li^+ conduction is presented, generally called a bottleneck. This bottleneck size depends on the framework structure and lattice constant. Figure 1.5 shows the relationship between the lattice volume per lithium against both ionic conductivity and E_a for various LISICON-structured $Li_{3.5}M_{0.5}M_{0.5}O_4$ estimated by DFT calculation [8]. The larger lattice volume per lithium provides a larger bottleneck size and then increases the ionic conductivity due to the reduction of E_a.

1.3.2 Grain boundary conduction

There are two types of ion conduction pathways in grain boundary (GB) conduction. Figure 1.6 shows the schematic image of granular conduction (Fig. 1.6(a)) that considers conduction across GB (GB⊥) and along with GB (GB∥) (Fig. 1.6 (b)). This ion conduction across/along GB has still been unclear, but theoretical calculation suggests the value of ΔG_m for a typical GB.

In general, the resistance can be written as the product of conductivity (σ) and geometric parameters length (l) and area (A):

$$R = \frac{l}{\sigma A} \quad (9)$$

The total resistance, R_{Total}, related to the ionic conductivity is equal to:

$$R_{total} = \left(\frac{1}{R_{GB\perp} + R_{Bulk}} + \frac{1}{R_{GB\parallel}} \right)^{-1} \quad (10)$$

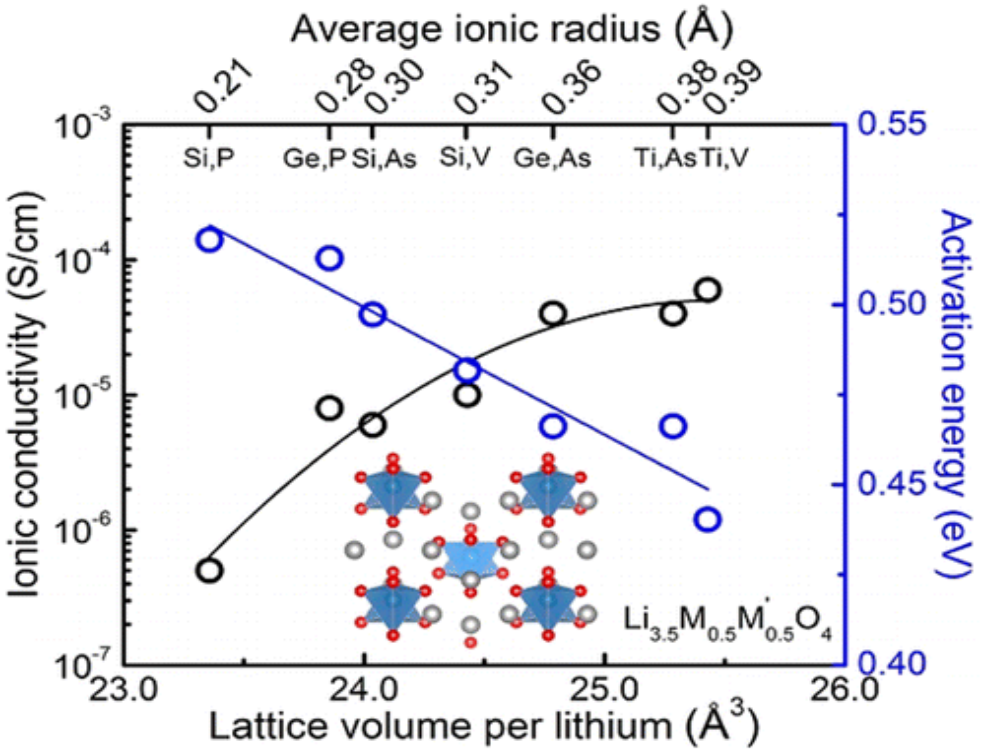

Figure 1.5 Variation ionic conductivity and activation energy based on the lattice volume and ionic radius in $Li_{3.5}M_{0.5}M_{0.5}O_4$ [8].

As such, Eq. (10) becomes:

$$\frac{l_{Total}}{\sigma_{Total}A_{Total}} = \left(\frac{1}{\frac{l_{GB\perp}}{\sigma_{GB\perp}A_{GB\perp}} + \frac{l_{Bulk}}{\sigma_{Bulk}A_{Bulk}}} + \frac{1}{\frac{l_{GB\parallel}}{\sigma_{GB\parallel}A_{GB\parallel}}} \right)^{-1} \quad (11)$$

At this point two assumptions are made:

1) The length l that an ion needs to cross in the bulk material is the same regardless of mechanism used. Therefore, the tortuosity effects are not considered and the ions travel on a straight line parallel to the current applied. Under this assumption $l_{Total} = l_{Bulk} = l_{GB\parallel}$.

2) In the first mechanism, the ion has to cross a GB (of thickness l_{GB}) every time it reaches the end of a grain, meaning for every distance d travelled, where d is the grain size,

$$l_{GB\perp} = l_{GB}\frac{l_{Total}}{d}$$

It should be noted that both of these assumptions are beneficial for the total ionic conductivity. In other words, the ionic conductivity calculated this way might be slightly overestimated. Under these assumptions, Eq. (11) becomes independent of the macroscopic sample length:

$$\sigma_{Total}A_{Total} = \frac{1}{\frac{l_{GB}}{d}\frac{1}{\sigma_{GB\perp}A_{GB\perp}} + \frac{1}{\sigma_{Bulk}A_{Bulk}}} + \frac{1}{\frac{1}{\sigma_{GB\parallel}A_{GB\parallel}}} \quad (12)$$

A parameter, y_{Bulk}, is introduced that controls the volume fraction of crystalline domains that exhibit the first mechanism of conduction ("Granular"). Analogously, y_{GB}(=1-y_{Bulk}) is the volume fraction of GB domains that exhibit the second mechanism of conduction ("GB"). These parameters reflect the microstructure of a polycrystalline sample in terms of densification. In a real sample, these would be linked to the specific processing, e.g., melt-quenching vs. solid-state reaction, annealing/sintering regime and so on.

Assuming an isotropic microstructure, the areas of conduction for each mechanism depend on the volume fraction of grains compared to GBs, as captured by the parameters y_{Bulk}

and y_{GB}. As such, $A_{GB\perp} = A_{Bulk} = y_{Bulk}A_{Total}$ and $A_{GB\parallel} = y_{GB}A_{Total}$. This leads to the final geometry-independent relation for the total ionic conductivity of a polycrystalline sample:

$$\sigma_{Total} = y_{Bulk}\left(\sigma_{Bulk} + \frac{d}{l_{GB}}\sigma_{GB\perp}\right) + y_{GB}\sigma_{GB\parallel} \quad (13)$$

where σ_{Bulk} is equal to the bulk conductivity of the crystalline material, while $\sigma_{GB\perp}$ and $\sigma_{GB\parallel}$ are the components of the GB conductivity across and along the grain boundary, respectively. Here, d is the grain size, l_{GB} is the length of the GB, and y_{bulk} and y_{GB} control the volume fraction of the grain and GB domains.

The grain sizes of the solid electrolytes can also influence the ionic conductivity as they can influence the grain boundary conductivity. The increase in the grain size will result in a decrease in the number of grain boundaries. Therefore, the grain boundary resistance decreases and the ionic conductivity increases; vice versa, the reduction in grain size will increase the number of grain boundaries, increasing the grain boundary resistance and decreasing the ionic conductivity. For small grain sizes of <100 nm, the influence of GB resistance is strong and the total conductivity is dominated by the GBs (Figure 1.6 (b)).

1.4 Oxide-based Li^+ conductive solid electrolytes - advantages and problems

The most important material in ASSBs is inorganic Li^+ conductive solid electrolyte. Table 1.1 lists the typical examples of oxide-based Li^+ conductive solid electrolytes. Generally, Li^+ conductivity in crystalline materials is higher than amorphous Li^+ conductive materials because the Li^+ can move smoothly through the bottleneck formed in the periodic potential in a crystal. This bottleneck size and the Li^+ conduction pathway depend on the crystal structure of the framework structure, and the typical framework structure is NASICON (Na superionic conductor), LISICON (Li superionic conductor), perovskite, and garnet. Some of the compounds applying those structures have exceeded their Li^+ conductivity over 1×10^{-3} S cm^{-1}. Considering that common Li^+ conductive organic liquid

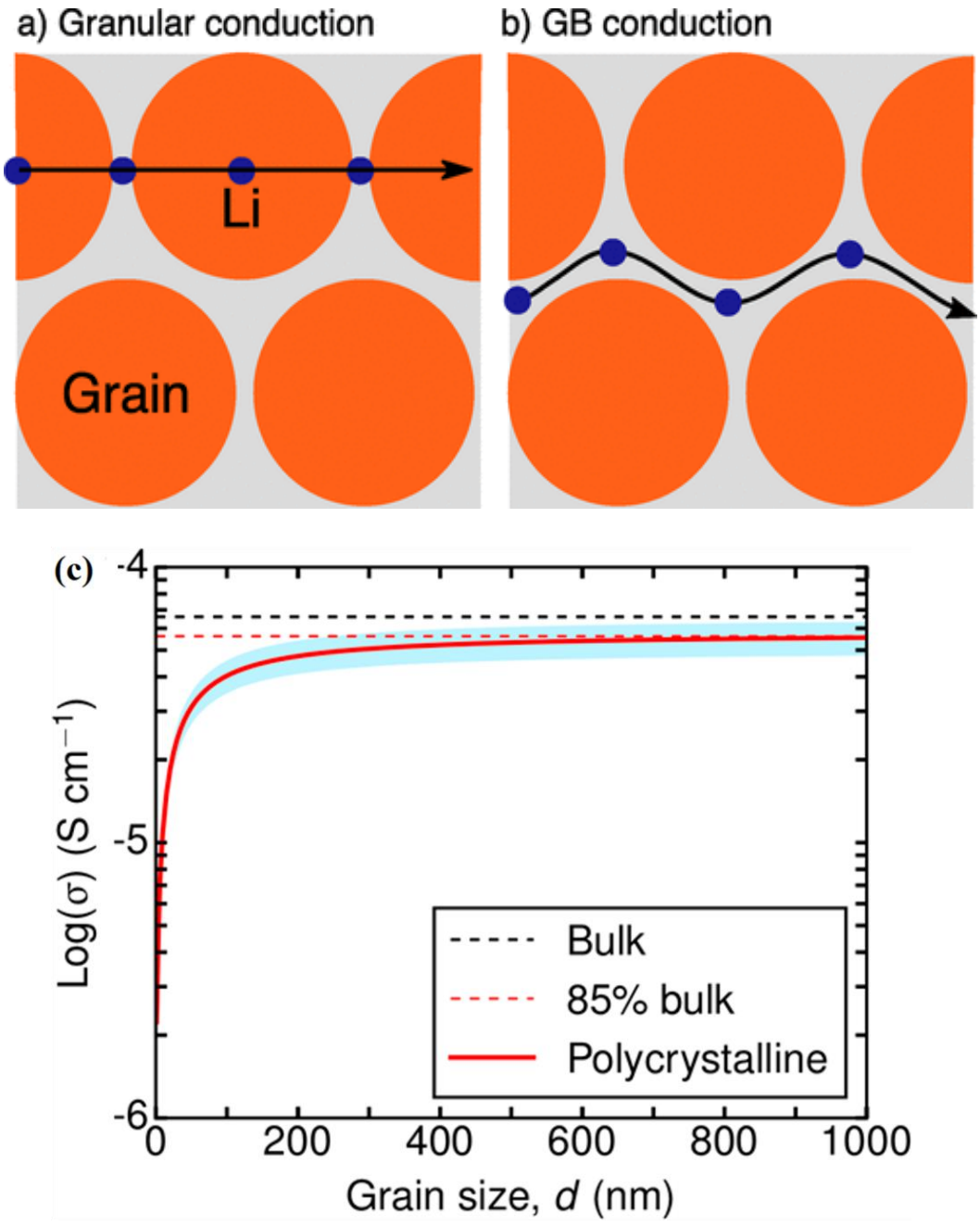

Figure 1.6 Schematic of ion conduction pathway. (a) granular conduction and (b) GB conduction and (c) Evolution of the total conductivity (bulk + polycrystalline) as a function of grain size, d (in nm). The black dashed line is the calculated bulk conductivity. The red curve is the total conductivity of the polycrystalline material, with the blue band representing its upper and lower limits. The red dashed line is the maximum average polycrystalline conductivity [10].

electrolyte has an ionic conductivity of 1×10^{-2} S cm^{-1}, but the Li^+ transfer number is 0.3 in the typical cases. Because the Li^+ transfer number in the solid electrolyte is almost 1, practical Li^+ conductivity in both conventional organic liquid electrolyte and high Li^+ conductive solid electrolyte is almost comparable. Those oxide-based solid electrolytes are non-flammable and leakage-free, and then they are great advantages to develop high energy density rechargeable batteries with a safety guarantee. Nevertheless, those solid electrolytes have just started to be applied in a small-sized ASSB. They are hard and fragile ceramics, and the sintering process is inevitably required for the battery fabrication process. To apply solid electrolytes for large-sized devices, typically electric vehicles, the solid electrolyte is desirable to have both high Li^+ conductivity and ductile properties as with sulfide-based solid electrolytes. Of course, the solid electrolyte will be better to keep safety aspects.

Recently, lithium-rich anti-perovskite structured material, commonly known as LiRAP, has been extensively investigated based on structure, preparation, composition, ionic conductivity, etc. This is because the LiRAP is a possible candidate to realize high Li^+ conductivity, ductile properties in addition to safer properties. The melting point of LiRAP is ca. 300 °C, and its Young's modulus is 100 GPa. This Young's modulus is almost comparable with sulfide-based material and much lower than conventional high Li^+ conductive oxide-based solid electrolyte shown in Table 1.1. Therefore, the LiRAP can be densified just by pressing at RT, the same as a sulfide-based solid electrolyte.

Table 1.1. Summary of the oxide-based crystalline solid electrolyte

Electrolyte structure (abbreviations)	**m.p. (°C)**	**Typical composition**	**RT ionic conductivity (S cm^{-1})**	**E_a (eV)**	**Reference**
NASICON	1250	$Li_{1.3}Al_{0.3}Ti_{1.7}(PO_4)_3$	10^{-3}	0.3-0.5	[11,12]
LISICON	1300	$Li_{14}ZnGe_4O_{16}$	10^{-6}	0.4-0.6	[13-16]
Perovskite	1200	$La_{2/3-x}\ \square_{1/3-2x}Li_{3x}TiO_3$	10^{-3}	0.3-0.4	[17-21]
Garnet	>1500	$Li_7La_3Zr_2O_{12}$	10^{-3}	0.4-0.6	[22-26]
Anti-perovskite (This work)	254-285	Li_2OHBr, Li_3OBr	10^{-3} – 10^{-7}	0.3- 1.0	[27-40]

1.5 Lithium Rich Anti-Perovskite (LiRAP) solid electrolytes

1.5.1 Structure

Cubic phased LiRAP has general formula $Li_{3-x}OH_xX$ (X = Cl, Br). $Li_{3-x}OH_xX$ (X = Cl, Br) possesses the typical anti-perovskite structure by changing the normal perovskite ABO_3 to inverted charge $A^-B^{2-}X^+_3$. This new promising family of structurally-inverted anti-perovskites, $Li_{3-x}OH_xX$ (X = Cl, Br), was reported with the same space group 221 (Pm-3m) and structure as conventional perovskites but with inverted anion and cation sub-lattices. In the dehydrated Li_3OX anti-perovskites, the corner sites of the unit cell are occupied by X^- ions, the body-centered sites are occupied by O^{2-} ions and Li^+ from the octahedral structure around the oxygen. Therefore, the A anion has a coordination number of 12, while the B anion occupies the center of an octahedron with a coordination number of 6. The report from Ceder's group suggests that this arrangement of Li^+ ions in a BCC sub-lattice is optimal for fast Li^+ ion conduction [41].

According to the theoretical calculation, both Li_3OBr and $Li_7O_2Br_3$ have meta-stable phases. When compared, $Li_7O_2Br_3$ is even less stable than the Li_3OBr. The $Li_7O_2Br_3$ was formed as a secondary phase during the Li_3OBr synthesis process. $Li_7O_2Br_3$ is a layered anti-perovskite structured compound, which is thermodynamically unstable when compared to Li_3OBr. Hence, synthesizing pure samples is very difficult, and it can be prepared only in mixed-phase [33].

The structure of $Li_5(OH)_2Br_3$ is characterized by anti-perovskite-like double layers consisting of 2 x Li_2OHBr, which alternate with rock-salt-like layers of LiBr. In this case, the Li_2OHBr is the common building unit in both structures. Hence, intergrowth might be possible. $Li_5(OH)_2Br_3$ is metastable whereas, Li_2OHBr is considered as highly stable [42].

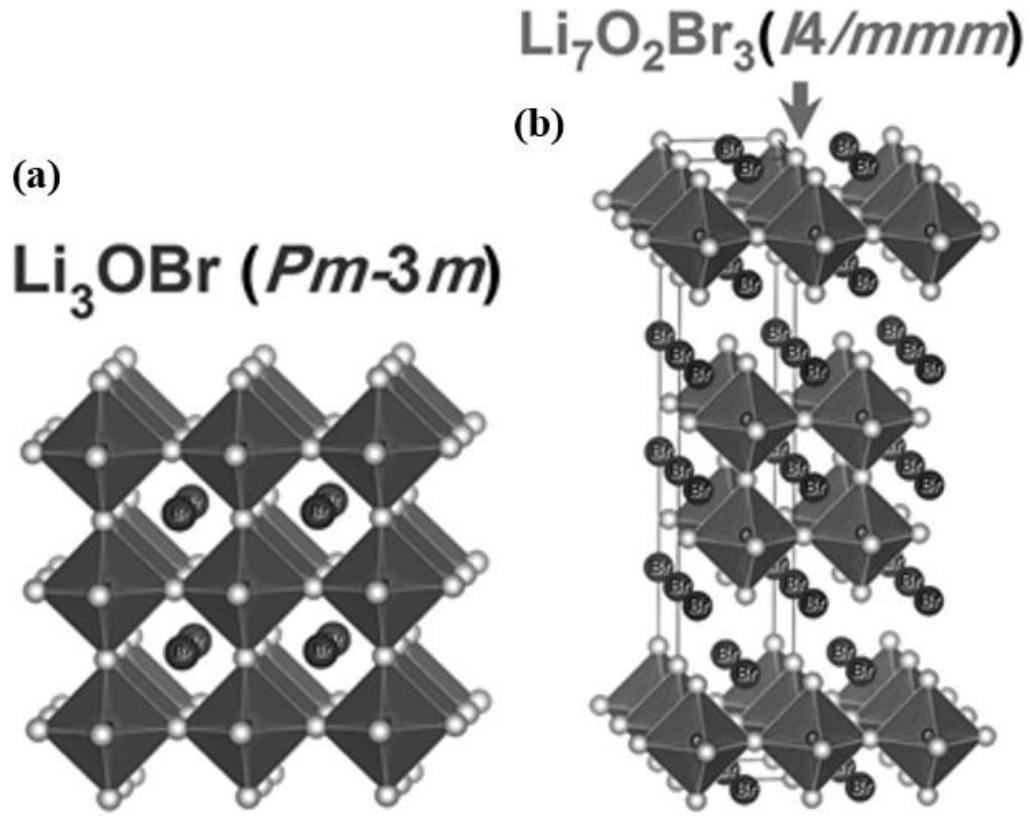

Figure 1.7 (a) Crystal structure of anti-perovskite cubic Li_3OBr **(b)** Anti-perovskite structure of tetragonal $Li_7O_2Br_3$ [33].

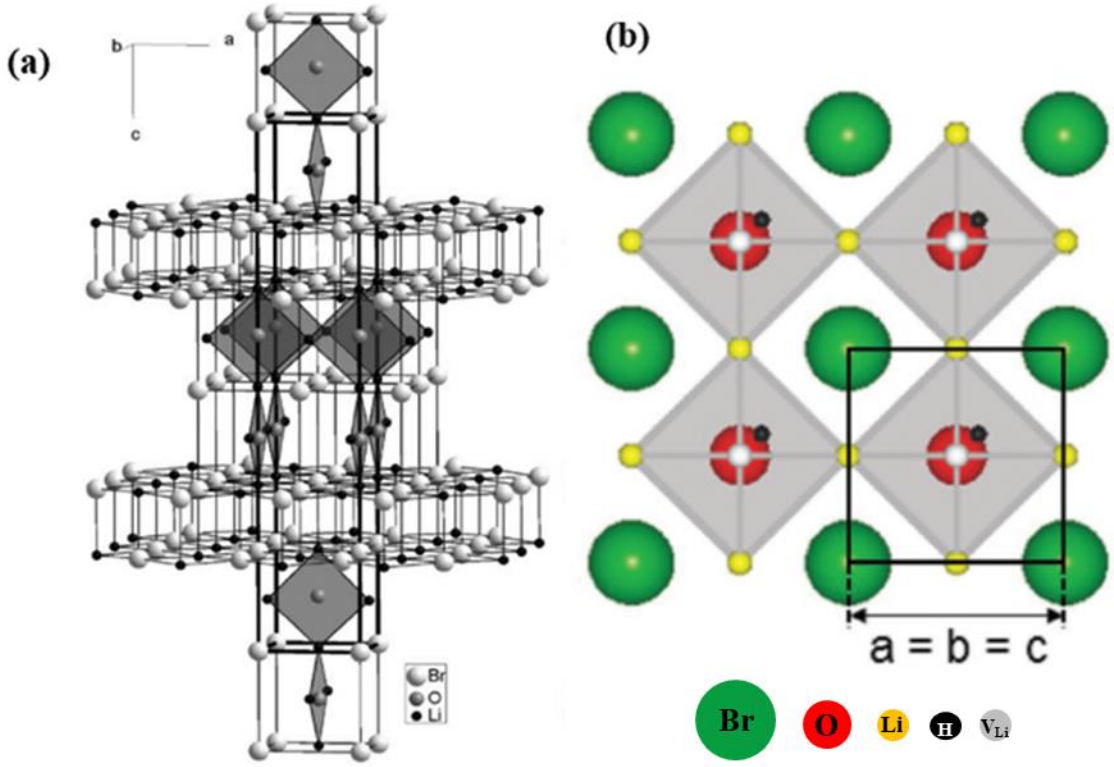

Figure 1.8 (a) Crystal structure of anti-perovskite tetragonal $Li_5(OH)_2Br_3$ (K. Friesse *et al.*) [42] **(b)** Anti-perovskite structure of cubic Li_2OHBr. Green, red, yellow, grey, and black spheres are Br^-, O_2^-, Li^+, vacancy, and H^+, respectively [36].

1.5.2 Synthesis and Composition

In anti-perovskites system, the structure can be modified by chemical substitution, like substituting Cl^- with larger Br^- or I^- anions or by substituting divalent cations for Li, to improve the ionic conductivity. LiRAP are reported to have very good electrochemical stability against lithium metal anode, but they are highly sensitive to moisture. Zhang et al. and Emly et al. reported that anti-perovskites such as Li_3OCl, Li_3OBr, and the mixed halogen compounds are thermodynamically metastable from the density functional theory calculations (DFT). A glass transition was expected to take place at ~ 150 ˚C. The molecular dynamics (MD) simulations showed that perfect crystal structured anti-perovskites are poor Li^+ conductors, whereas the ones with, Li vacancies and structural disorder promote Li^+ diffusion by reducing activation energy barriers. The strategy to optimize the composition for increasing the Li^+ conductivity in the LiRAP was predicted by a combination of first-principles calculations and percolation theory. The low mixing energies in the Li_3OCl-Li_3OBr pseudo-binary system indicate that halide disorder is likely at room temperature. Nudged elastic band (NEB) calculations show that a Cl-rich channel with Br-rich endpoints tends to lower the vacancy migration barriers in the LiRAP structure. By incorporating the NEB barriers in a bond percolation model, it was found that higher Li^+ conductivity in $Li_3OCl_{1-x}Br_x$ structures near $0.235 \leq x \leq 0.395$ was possible. Further, this theory was confirmed using AIMD simulations, which predict a higher Li^+ conductivity for $Li_3OCl_{0.75}Br_{0.25}$ compared to $Li_3OCl_{0.5}Br_{0.5}$, the highest conductivity composition in the anti-perovskite chemistry identified experimentally thus far. Further, by theoretical calculations, P. Jena et al. explored the possibilities of using cluster ions, i.e., super halogens with larger ionic radii in the lithium-rich anti-perovskites structure, which can enlarge the channel size and lead to fast Li^+ conduction. It also shows that partially replacing the larger super halogen with another halogen can further increase the ionic conductivity, and the mixed phase of $Li_3S(BF_4)_{0.5}Cl_{0.5}$ is estimated to exhibit an ultra-high ionic conductivity [43]. Even

Table 1.2. Previous works reported on LiRAP synthesized by different techniques

Year	Author	Sample	Synthesis condition				Physical properties	
			BM	Temp ˚C	Atm	Heating substrate	Purity, Phase	Lattice constant Å
1981	P. Hartwig et al [27]	Li_2OHBr	×	500 1h	Ar	Mo crucible	Impure, Cubic	4.056
2003	G. Schwering et al [28]	Li_2OHBr	×	350 72h	Ar	Ag crucible	Pure, Cubic	4.046
2012	Y. Zhao et al [29]	Li_3OBr	×	360	vac	Quartz tube	Impure, Cubic	4.020
2014	M.H. Braga [30]	Li_3OCl	×	240 96h	vac	Teflon reactor	Impure, Mixed phase	3.910
2014	X. Lu et al [31]	Li_3OCl	×	300 48h	vac	Quartz tube	Pure, Cubic	3.910
2016	S. Li et al [32]	Li_3OBr	2h	500	Ar	Al crucible	Pure, Cubic	3.916
2016	J. Zhu et al [33]	Li_3OBr	1 h after heat	480 48h	Ar	Al crucible	Impure, Mixed phase	4.035
2016	Y. Li et al [34]	Li_2OHBr	×	350 30mins	Ar	Al crucible	Pure, Cubic	4.056
2016	Z.D. Hood et al [35]	Li_2OHCl	×	350 30mins	Ar	Ni crucible	Pure, Orthor-hombic	-
2018	A-Y. Song et al [36]	Li_2OHBr	×	650	Ar	Graphite crucible	Pure, Orthor-hombic	a = 3.8945 b = 3.9937 c = 7.6634
2018	M. Dondelinger et al [37]	Li_3OCl	×	350 10mins	Ar	Ni foil	Impure, cubic	3.910
2020 (This work)	M. K. Sugumar Et al [38]	Li_2OHBr	700 RPM, 48h	×	Ar	×	Pure, Cubic	4.046

BM – Ball-Milling; Temp – Temperature; Atm – Atmosphere; Ar – Argon; Vac – Vacuum

though the theoretical calculations predict high conductivity, there are no experimental results reported to support the theory until now. The diversity of solid-state electrolytes (SSEs) with tunable structures and compositions and advanced theoretical techniques have accelerated the search for appropriate SSEs with high ionic conductivity, the fast development of halide SSEs with superionic conductivities is expected in the near future. Moreover, crystallographic studies and atomic-level characterization to explore the local structures and ionic conduction mechanisms are also required as they provide guidelines for the development of new SSEs.

1.5.3 Li^+ conductivity in LiRAP and their mechanism

Figure 1.9 shows the schematic of a vacancy migration in the LiRAP structure in which each Li^+ is coordinated by two O^{2-} and four halide ions X^-. The nearest neighboring Li^+ share three coordinated anions out of which one is O^{2-} and two are X^-. During a vacancy hop, the vacancy migrates from a Li^+ site to the nearest Li^+ site via a triangular channel made of three shared anions. The letters i, c, and f represent "initial", "channel", and "final", respectively [44]. The anti-perovskite structured Li^+ conductors like Li_3OCl and Li_3OBr have mobile cation and immobile anion in the lattices. The oxygen and halide anions (Cl^-, Br^-) are bcc packed in the lattice. The Li interstitials lower the activation energy as they activate a path connecting energy-equivalent tetrahedral sites. Figure 1.9 shows that, in the bcc lattice, the Li^+ migrates with a remarkably low barrier along the path connecting two face-sharing positions. The Li^+ migration barrier in bcc-type anion frameworks is low in lattices formed by O^{2-} or halide anions (Cl^-, Br^-) than that of other close-packed types. In the case of sulfur based solid electrolytes like $Li_{10}GeP_2S_{12}$, $Li_{10}SnP_2S_{12}$, $Li_{10}SiP_2S_{12}$, $Li_7P_3S_{11}$, Li_2S, Li_4GeS_4 and γ-Li_3PS_4, the activation barrier is large for small volumes because large energy is required for the Li^+ to pass through a small bottleneck. Further, when the volume increases, the activation energy decreases as the size of the bottleneck increases. Hence, volume plays an important role in the

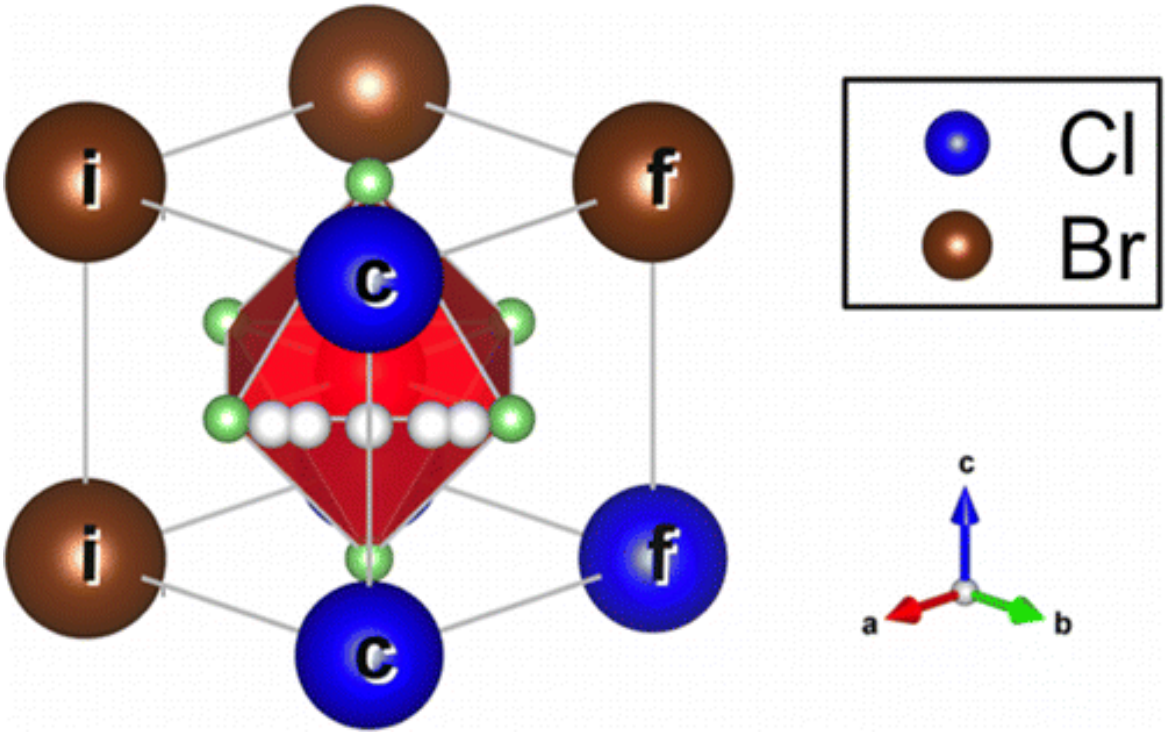

Figure 1.9 Schematic of BB-CC-BC Li^+ conduction pathway. Li^+ (green) form the octahedral structure around the oxygen (red). The letters i, c, and f represent "initial", "channel", and "final" sites, respectively [44].

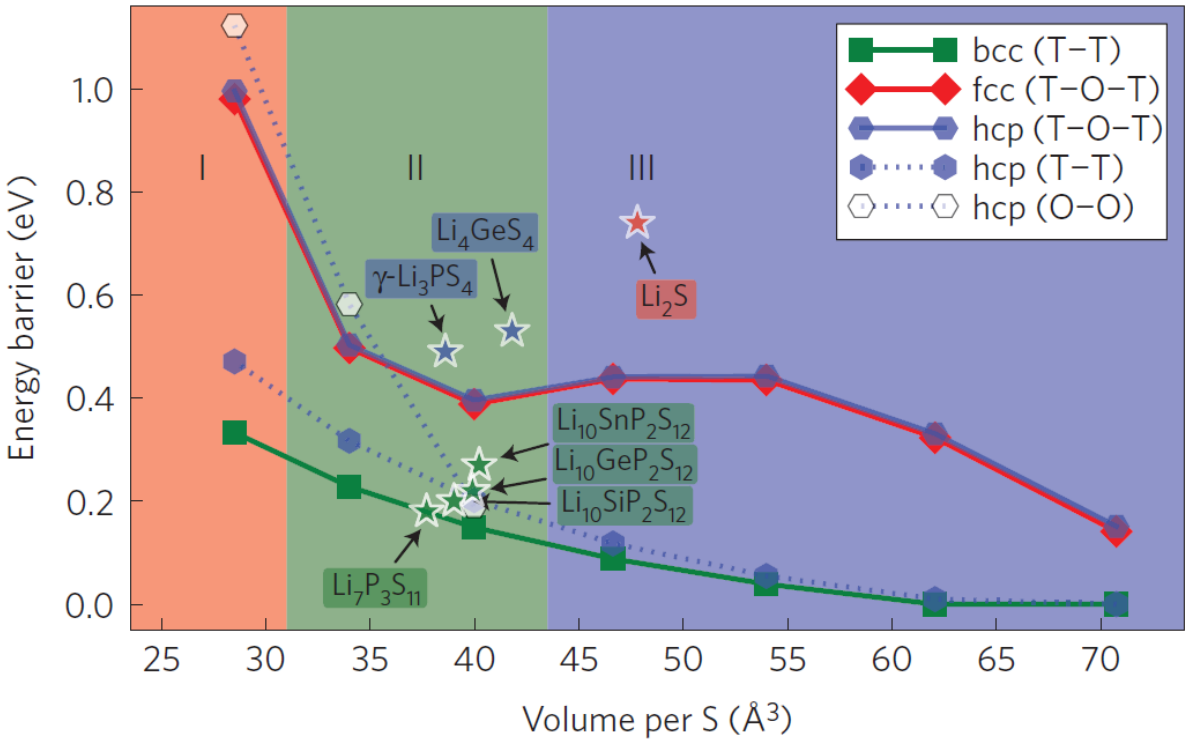

Figure 1.10 Activation barrier for Li^+ migration versus lattice volume. Activation barrier calculated for the Li^+ migration pathways in the bcc/fcc/hcp S^{2-} lattices at different volumes. Solid and dotted lines are guides to the eye. Experimental activation energies for $Li_{10}GeP_2S_{12}$, $Li_{10}SnP_2S_{12}$, $Li_{10}SiP_2S_{12}$, $Li_7P_3S_{11}$, Li_2S, Li_4GeS_4 and γ-Li_3PS_4 are marked by a star symbol for comparison. The underestimate of the activation energy for Li_2S is due to fact that the experimental value contains contributions from defect formation energy [41].

Li^+ mobility. According to Figure 1.10, almost for all the volumes, the bcc arrangement is optimal for Li^+ mobility with low activation barrier. Since, LiRAP are considered to be soft in nature like sulfur based solid electrolytes, this same principle can be applied to anti-perovskite structured solid electrolytes like Li_3OCl and Li_3OBr where, the oxygen and halide anions are bcc packed. Even though the presence of Li interstitials, can lower the activation energy for oxides with bcc oxygen framework, in some cases, the small volume and reduced polarizability can increase the electrostatic interactions between the migrating ion which can result in higher activation energy. The Li^+ migration barrier monotonically decreases as volume increases in the bcc-type lattice. So, the bcc arrangement remains optimal for Li^+ mobility.

The LiRAP solid electrolytes include both lithium-oxide halides Li_3OX, lithium-hydroxide halides Li_2OHX (Figure 1.11). The Li_2OHX adopts the $A^-B^{2-}X^+_3$ structure, where only two-thirds of the Li^+ positions are occupied, leaving the others vacant. Li_3OX has a highly ordered structure with high lithium content with no defects in the lattice. This limits the mobility of Li^+ and leads to low Li^+ conductivity in this kind of material. Whereas, in Li_2OHX it was reported that short and fast rotating O–H bonds provide extra space and help in the formation of Frenkel defects, which in turn helped to achieve fast, correlated Li^+ transport in this kind of materials [45]. Figure 1.12 shows that the OH^- groups point towards Li vacancies. Li^+ hopping occurs *via* these vacancies, denoted by the blue dashed arrows. Rotation of the OH^- groups occurs as a result of a nearby Li^+ hopping to an adjacent site, denoted by the black dashed arrow.

The DFT calculations were carried out to study the role of cation doping. The Li hopping in the Ca-doped structure suggest that the lattice dynamics cause further disorder. Li vacancies are created in the cation sub-lattice by doping with high valency cations like, Ca^{2+}, Mg^{2+} and Ba^{2+} which lowers the activation energy for Li^+ conduction. The mixed halogen $Li_3OCl_{0.5}Br_{0.5}$ sample showed an improved ionic conductivity of 1.94×10^{-3} S cm^{-1} and the

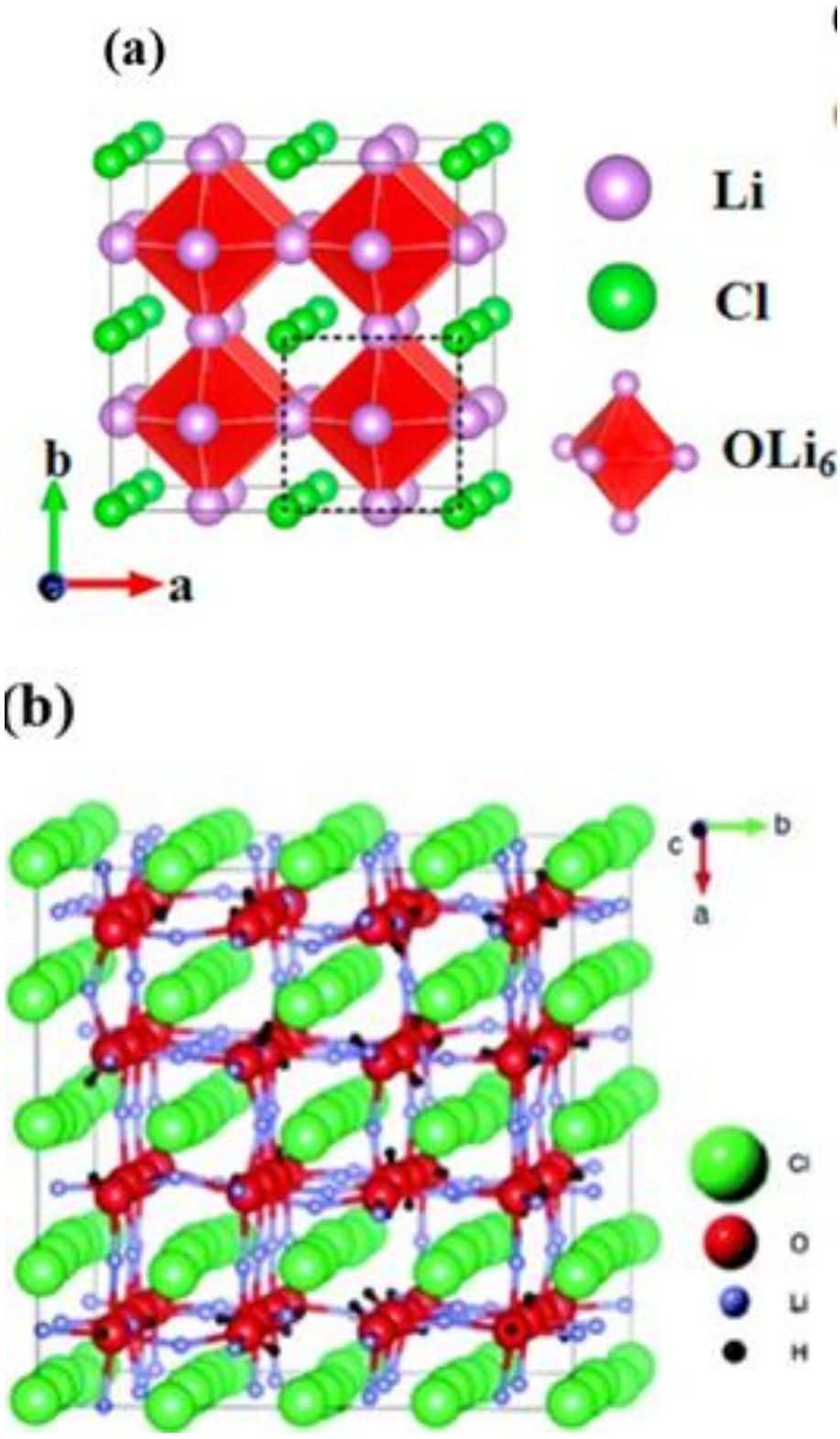

Figure 1.11 (a) Crystal structure of anti-provskite Li_3OCl **(b)** Anti-perovskite structure of cubic Li_2OHCl [45].

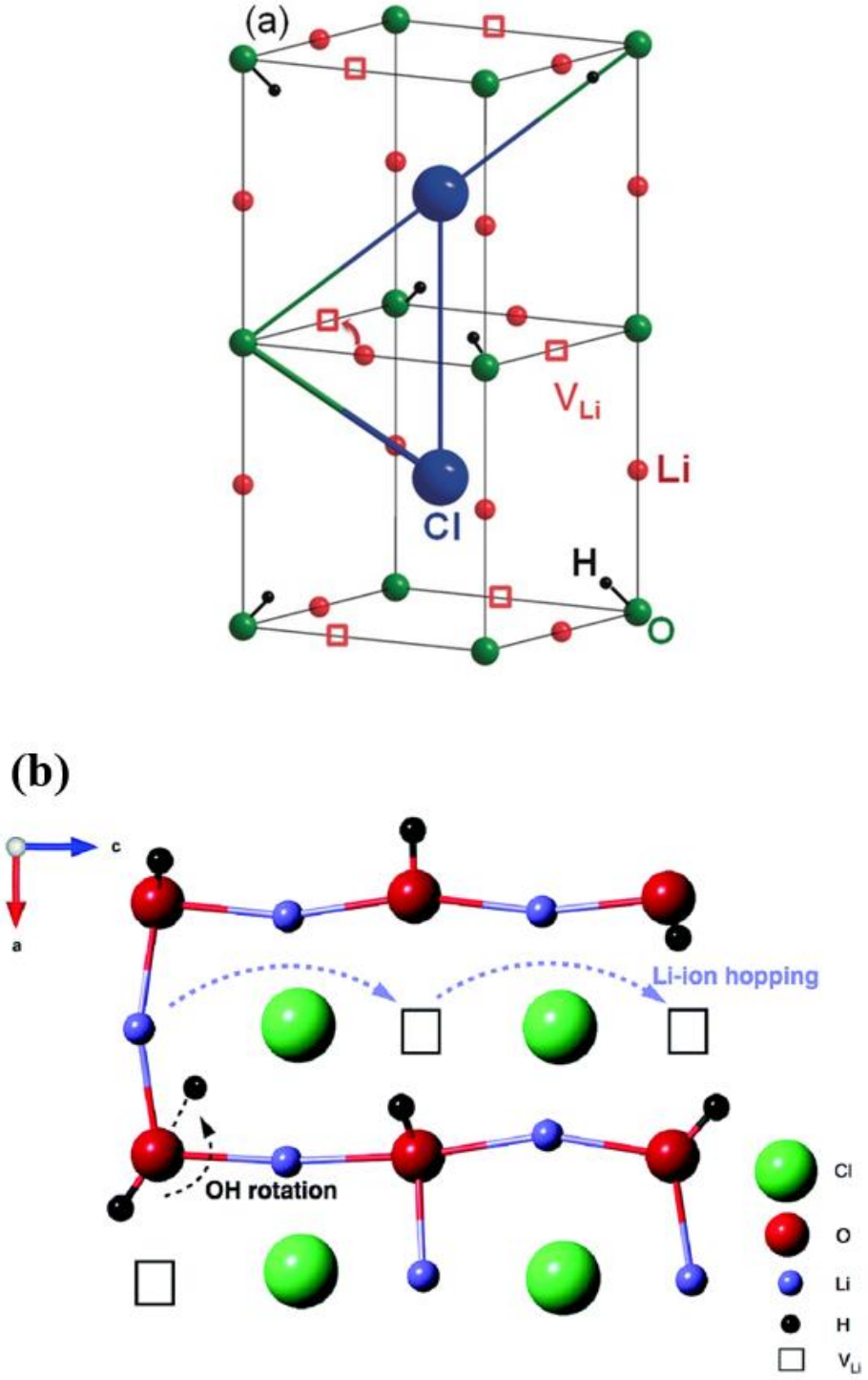

Figure 1.12 (a) Crystal structure of cubic Li_2OHCl; H^+ is on the axis of a O−Cl bond and forms an OH^- bond; the triangle is the Cl-O-Cl plane in the path of Li-ion transport. Red open squares indicate Li vacancies [34]. **(b)** Schematic representation of the Li^+ hopping mechanism in the cubic $Pm\bar{3}m$ phase of Li_2OHCl [45].

cation-substituted $Li_{3-2x}M_xHalO$ glassy electrolytes (M = Ca, Mg, or Ba; Hal = Cl^-, Br^- or I^-), which were prepared by Braga et al., exhibited an unusually high ionic conductivity of 2.5×10^{-2} S cm^{-1} at 25 ˚C was reported for $Li_{3-2x}Ba_xOCl$ (x = 0.005). In comparison to other solid electrolytes, which includes oxide perovskite such as $La_{0.5}Li_{0.5}TiO_3$; hydroxides containing Li and halides, lithium nitride, glassy material such as $Li_2S–SiS_2–Li_3PO_4$ and α, β AgI, the glassy phase, $Li_{3-2x}M_xHalO$, offers higher ionic conductivity and superior chemical stability (Figure 1.13). Further, unlike Ti and Ge containing materials, $Li_{3-2x}M_xHalO$ are stable with lithium-metal and offers a wide window of electrochemical stability. The ionic conductivity and the activation energy of different LiRAP from the past reports have been tabulated in Table 1.3. The discrepancies are due to the different sample preparation method listed in Table 1.2. Based on the sample synthesis method and how the pellets are prepared for EIS measurements, a wide range of results are observed due to differences in stoichiometry and grain boundary structure. These differences have resulted in different ionic conductivity ranging between 10^{-6} – 10^{-3} S cm^{-1} with activation energy varying between 0.26 – 0.97 eV. The reports of Li et al. suggest that there is the possibility of the as-prepared "Li_3OX" to be Li_2OHX instead of Li_3OX [32]. In addition, Braga et al. reported that the existence of H^+ was beneficial for the formation of an amorphous glassy phase, and very high ionic conductivity of 10^{-2} S cm^{-1} at 25 ˚C was reported [30].

Figure 1.14 (a) shows the atomic-scale image of the above-mentioned conduction in anti-perovskite-structured Li_3OCl with Σ3 grain boundary, where the V pathway represents the Li^+ conduction across the GB and the P pathway along with the GB. Figure 1.14 (b) shows the estimated ΔG_m for each case, and the P-path has a smaller value than that of the V-path. In the case of Li_3OCl, E_a of in grain has been expected to be 0.31 eV by DFT, which is smaller than that of GB. Thus, it has been proposed that Li^+ conduction at GB is the dominant resistance in Li_3OCl [46]. Generally, the GB increase in the high Li^+ conductive solid electrolyte provides

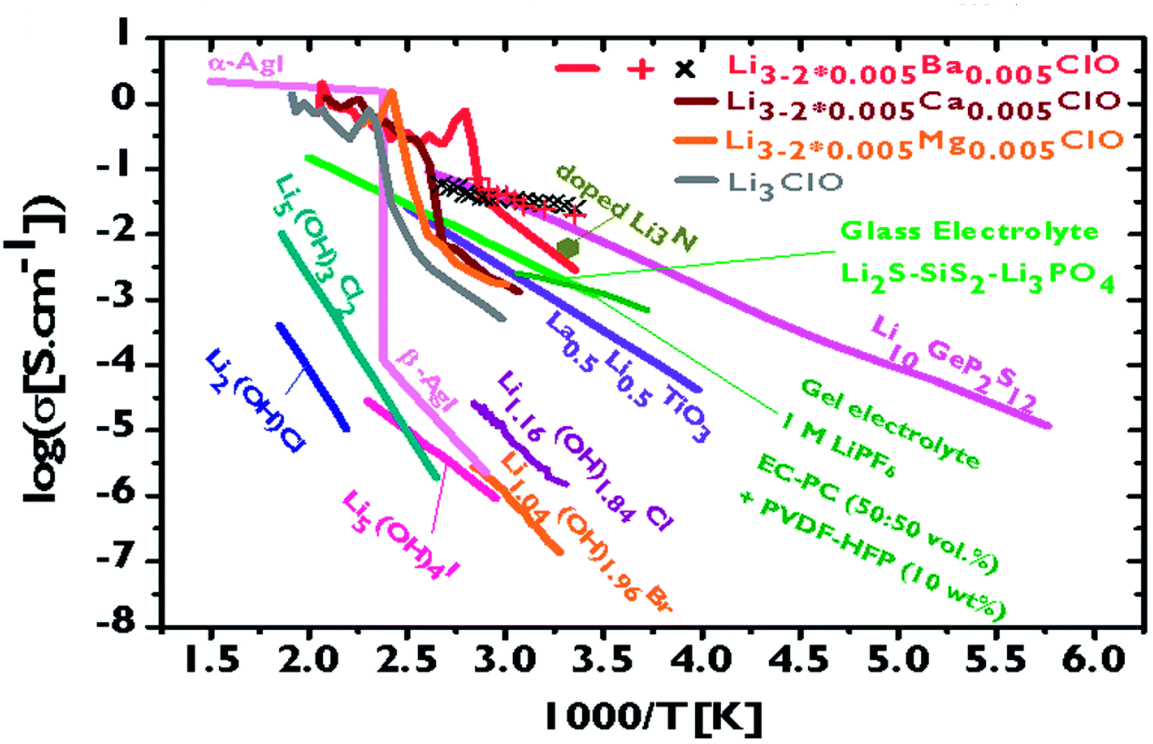

Figure 1.13 Comparison between the logarithm of the ionic conductivities of hydroxides that are formed during $Li_{3-2x}M_xHalO$ synthesis; some known solid electrolytes and a gel electrolyte commonly used in Li-ion batteries; Li_3ClO and $Li_{3-2\times0.005}M_{0.005}ClO$ (M ¼ Mg, Ca and Ba) during heating. Line and symbols +, × for $Li_{3-2\times0.005}Ba_{0.005}ClO$ glassy samples in their 2nd, 3rd and 4th heating/cooling cycles, respectively [30].

Table 1.3. Ionic conductivity and activation energy of different LiRAP from past reports

Sample	**Conductivity (S cm^{-1}) 25 ˚C**	***E*$_a$ (eV)**	**Author**
Li_2OHBr	10^{-7}	0.97	P. Hartwig et al [27]
Li_2OHBr	10^{-6}	0.84	G. Schwering et al [28]
Li_3OBr	10^{-5}	0.26	Y. Zhao et al [29]
Li_3OCl	10^{-3}	0.49	M.H. Braga [30]
Li_3OCl	10^{-7}	0.59	X. Lu et al [31]
Li_3OBr	10^{-6}	0.74	S. Li et al [32]
Li_3OBr	10^{-6}	0.70	J. Zhu et al [33]
Li_2OHBr	10^{-6}	0.75	Y. Li et al [34]
Li_2OHCl	10^{-6}	0.56	Z.D. Hood et al [35]
Li_2OHBr	10^{-6}	0.26	A-Y. Song et al [36]
Li_3OCl	10^{-7}	0.31	M. Dondelinger et al [37]
Li_2OHBr (This work)	10^{-6}	0.54	M. K. Sugumar et al [38]

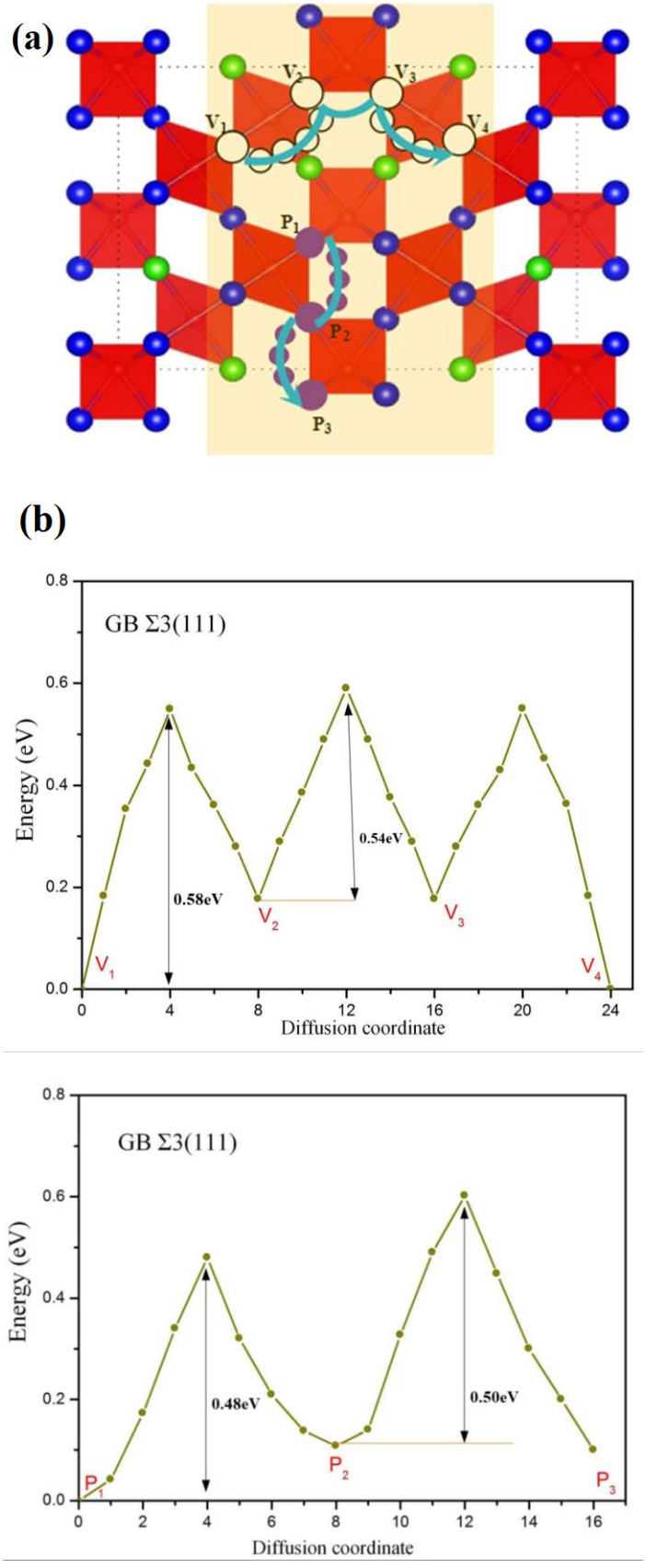

Figure 1.14 (a) Schematic of Li migration pathway with GB structures **(b)** Energy profile of Li^+ in GB structures based on first-principle simulations [46].

a serious energy barrier of Li^+ solid electrolyte, leading to the reduction of total Li^+ conductivity.

1.6 Purpose of this thesis

A series of LiRAP is a candidate considered as a superior oxide-based Li^+ conductive solid electrolyte because they are soft and possibly high Li^+ conductive materials. As introduced in the previous chapter, researches for improving total ionic conductivity of LiRAP will be classified as follows.

1. Cation doping
2. Halogen species control including mixed halogen effects
3. H amount

Among them, the most serious problem will be the control of hydrogen amount in LiRAP. Most of the preparation method apply heating process for fabricating LiRAP and then it will not be easy to suppress the removal of H during the fabrication. Thus, a better way will be to fabricate LiRAP at lower temperature, and then we can systematically clarify how the total ionic conductivities are influenced on other factors considering the H amount. Based on the above motivations, the author has focused on the preparation of LiRAP at room temperature and then investigate their ionic conductivities.

In chapter 2, cubic-phase anti-perovskite-structured Li_2OHBr is synthesized at room temperature just by a dry ball-milling process. The resultant lattice constant of 4.046 Å and ionic conductivity of 1.1×10^{-6} S cm^{-1} is in good agreement with the past work, and the synthesis process is a very simple method to fabricate Li_2HOBr. This is an effective method to control the hydrogen amount, as discussed in chapter 5 in detail.

In chapter 3, Li_2OHCl is synthesized by room temperature dry ball-milling process. Li_2OHCl generally forms an orthorhombic phase at room temperature, but the resultant

material forms a cubic phase and then shows higher conductivity than previous reports. This metastable cubic-phase formation will originate from the smaller-sized crystallites uniquely formed through mechanochemical synthesis.

In chapter 4, anion-exchanged LiRAP are prepared to improve total Li^+ conductivity. $Li_2OHBr_{1-x}X_x$ (X = Cl, I) mixed halogen samples are prepared at room temperature by dry ball-milling process, and both the solid solution formation range and total ionic conductivity are studied. The $Li_2OHBr_{0.9}I_{0.1}$ sample has the largest lattice constant of 4.060 Å with the highest total ionic conductivity of 4.9×10^{-6} S cm^{-1} at room temperature.

In chapter 5, Li-excess and Li-deficient anti-perovskite structured $Li_{2+x}OH_{1-x}Br$ are prepared at room temperature by dry ball-milling process, and their effects on total ionic conductivity are discussed. The $Li_{2.2}OH_{0.8}Br$ sample with a lattice constant of 4.056 Å has a total ionic conductivity of 3.6×10^{-6} S cm^{-1} at room temperature. Rotational assistance of OH for improving total Li^+ conductivity will not play an important role in Li_2OHBr probably because of the larger lattice constant compared with Li_2OHCl.

References

1) C. Zou, Q. Zhao, G. Zhang and B. Xiong, Natural Gas Industry B 3 (2016) 1.
2) BP Energy Outlook, 2019 edition, London, United Kingdom, 2019.
3) Z. H. C. Daud, D. Chrenko, F. D. Santos, E. H. Aglzim and L. L. Moyne, Proc. of the Int. Workshop on Simulation for Energy, Sustainable Development & Environment 2013.
4) R. Malini, U. Uma, T. Sheela, M. Ganesan and N. G. Renganathan, Ionics 15 (2008) 301.
5) W. V. Schalkwijk and B. Scrosati, Advances in Lithium-Ion Batteries, 1st edition. Springer, 2002.

6) V. Thangadurai, S. Narayanan and D. Pinzaru, Chem. Soc. Rev. 43 (2014) 4714.

7) B. Dunn, H. Kamath and J. M. Tarascon, Science 334 (2011) 928.

8) J. C. Bachman, S. Muy, A. Grimaud, H. H. Chang, N. Pour, S. F. Lux, O. Paschos, F. Maglia, S. Lupart, P. Lamp, L. Giordano and Y. S. Horn, Chem. Rev. 116 (2016) 140.

9) H. Mehrer, Diffusion in Solids, 155 (2007) 64.

10) J.A. Dawson, P. Canepa, T. Famprikis, C. Masquelier and M. S. Islam, J. Am. Chem. Soc. 140 (2018) 362.

11) P. K. Jha, O. P. Pandey and K. Singh, Silicon 9 (2017) 411.

12) M.Guin and F.Tietz, J. Power Sources 273 (2015) 1056.

13) P. G. Bruce and A. West, Mat. Res. Bull. 15 (1980) 379.

14) P. G. Bruce and A. West, J. Solid State Chem. 44 (1982) 354.

15) R. Kanno, T. Hata, Y. Kawamoto and M. Irie, Solid State Ionics 130 (2000) 97.

16) M. Murayama, R. Kanno, M. Irie, S. Ito, T. Hata, N. Sonoyama and Y. Kawamoto, J. Solid State Chem. 168 (2002) 140.

17) A. Belous, G. N. Novitskaya, S. V. Polyanetskaya and Y. I. Gornikov, Inorg. Mater. 23 (1987) 470.

18) S. Stramare, V. Thangadurai and W. Weppner, Chem. Mater. 15 (2003) 3974.

19) O. Bohnke, Solid State Ionics 179 (2008) 9.

20) H. Hyooma and K. Hayashi, Mat. Res. Bull. 23 (1988) 1399.

21) V. Thangadurai and W. Weppner, Adv. Funct. Mater. 15 (2005) 107.

22) V. Thangadurai and W. Weppner, Ionics 12 (2006) 81.

23) E. J. Cussen, J. Mater. Chem. 20 (2010) 5167.

24) E. J. Cussen, Chem. Commun. 4 (2006) 412.

25) R. Murugan, V. Thangadurai and W. Weppner, Angew. Chem. Int. Ed. 46 (2007)

7778.

26) R. Murugan, S. Ramakumar and N. Janani, Electrochem. Commun. 13 (2011) 1373.

27) P. Hartwig, A. Rabeau and W. Weppner, J. Less Common Met. 78 (1981) 227.

28) G. Schwering, A. Honnerscheid, L. V. Wullen and M. Jansen, ChemPhysChem 4 (2003) 343.

29) Y. Zhao and L. L. Daemen, J. Am. Chem. Soc. 134 (2012) 15042.

30) M. H. Braga, J. A. Ferreira, V. Stockhausen, J. E. Oliveira and A. El-Azab, J. Mater. Chem. A 2 (2014) 5470.

31) X. Lü, G. Wu, J. W. Howard, A. Chen, Y. Zhao, L. L. Daemena and Q. Jia, Chem. Commun. 50 (2014) 11520.

32) S. Li, J. Zhu, Y. Wang, J. W. Howard, X. Lü, Y. Li, R. S. Kumar, L. Wang, L. L. Daemen and Y. Zhao, Solid State Ionics 284 (2016) 14.

33) J. Zhu, S. Li, Y. Zhang, J. W. Howard, X. Lü, Y. Li, Y. Wang, R. S. Kumar, L. Wang and Y. Zhao, Appl. Phys. Lett. 109 (2016) 101904.

34) Y. Li, W. Zhou, S. Xin, S. Li, J. Zhu, X. Lu, Z. Cui, Q. Jia, J. Zhou, Y. Zhao and J. B. Goodenough, Angew. Chem. Int. Ed. 55 (2016) 9965.

35) Z.D. Hood, H. Wang, A.S. Pandian, J.K. Keum and C. Liang, J. Am. Chem. Soc. 138 (2016) 1768.

36) A.-Y. Song, Y. Xiao, Dr. K. Turcheniuk, P. Upadhya, A. Ramanujapuram, J. Benson, A. Magasinski, M. Olguin, L. Meda, O. Borodin and G. Yushin, Adv. Energy Mater. 8 (2018) 1700971.

37) M. Dondelinger, J. Swanson, G. Nasymov, C. Jahnke, Q. Qiao, J. Wu, C. Widener, A.M. Numan-Al-Mobin and A. Smirnova, Electrochim. Acta 306 (2019) 498.

38) M. K. Sugumar, T. Yamamoto, M. Motoyama and Y. Iriyama, Solid State Ionics 349 (2020) 115298.

39) X.J. Lu, G. Wu, J.W. Howard A.P. Chen, Y.S. Zhao, L.L. Daemen and Q.X. Jia, Chem. Commun. 50 (2014) 11520.

40) I. Hanghofer, G. J. Redhammer, S. RohdeIlie, I. Hanzu, A. Senyshyn, H. M. R. Wilkening and D. Rettenwander, Chem. Mater. 30 (2018) 8134.

41) Y. Wang, W.D. Richards, S.P. Ong, L.J. Miara, J.C. Kim, Y. Mo and G. Ceder, Nat. Mater. 14 (2015) 1026.

42) K. Friese, A. Honnerscheid and M. Jansen, Kristallogr. 218 (2003) 536.

43) P. Jena and H. Fang, PNAS, 114 (2017) 11046.

44) Z. Deng, B. Radhakrishnan and S. P. Ong, Chem. Mater. 27 (2015) 3749.

45) J. A. Dawson, T. S. Attari, H. Chen, S. P. Emge, K. E. Johnston and M. S. Islam, Energy Environ. Sci. 11 (2018) 11, 2993.

46) B. Chen, C. Xu and J. Zhou, J. Electrochem. Soc. 165 (2018) A3946.

47) Y. Inaguma and M. Itoh, Solid State Ionics 86 (1996) 257.

Chapter 2

Room temperature synthesis of anti-perovskite structured Li_2OHBr

2.1. Introduction

Oxide-based all-solid-state rechargeable lithium batteries (Ox-SSBs) have been expected as next-generation rechargeable batteries with high energy density, long-life performances, and high safety. High Li^+ conductive solid electrolytes (SEs) are the key materials to improve the SSB, and some of oxide-based SEs such as NASICON-structured $Li_{1.3}Al_{0.3}Ti_{1.7}(PO_4)_3$ (LATP) [1], perovskite-structured $Li_{0.34}La_{0.55}TiO_3$ (LLT) [2], garnet structured $Li_7La_3Zr_2O_{12}$ (LLZ) [3], and newly developed structured $LiTa_2PO_8$ [4], have been reported to obtain ionic conductivity over 10^{-4} S cm^{-1} at 25 ˚C. However, all these SEs are hard and fragile ceramics and synthesized at a high-temperature range. Therefore, Ox-SSBs using these SEs require a high-temperature sintering process, which provides difficulty for developing large-scale Ox-SSBs system as have been realized in sulfide-based SSBs by mixing and pressing process at room temperature [5]. Also, most of the oxide-based SEs are unstable with lithium metal anode, and few of the SEs, LLZ and LiPON, are experimentally stable with lithium metal (Li) anode.

Among the oxide-based SEs, cubic-phase lithium-rich anti-perovskite (LiRAP: $Li_{3-x}OH_xX$ (X = Cl, Br), including $x = 0$) compounds have the potentials to overcome some of the above-mentioned problems ; that is, they are soft, stable against Li, and will have high Li^+ conductive materials (10^{-3} S cm^{-1} for Li_3OCl) [6]. Table 2.1 summarized some of the reported data on starting materials, synthesis temperature, ion conductivity, and activation energy about various LiRAP. As can be seen in Table 2.1, LiRAP have been synthesized by the sintering method above 300 ˚C with starting materials of LiOH (or Li_2O) and LiX. Sintering temperature

Table 2.1. Summary of previous reported LiRAP.

Sample	Starting Materials	Synthesis Temperature (˚C)	Ionic Conductivity (S cm^{-1})	Activation Energy (eV)	Ref.
Li_3OBr	Li_2O + LiBr	500	10^{-6} (25 ˚C)	0.74	7
Li_2OHBr	LiOH + LiBr	350	10^{-6} (25 ˚C)	0.75	9
Li_2OHBr	LiOH + LiBr	300	10^{-5} (200 ˚C)	0.97	17
Li_3OCl	LiOH + LiCl	360	10^{-3} (25 ˚C)	0.26	10
Li_2OHCl	LiOH + LiCl	400	10^{-6} (25 ˚C)	0.56	16

ca. 500 ˚C is necessary for the reaction of Li_2O and LiX, and reaction temperature can be decreased by using LiOH and LiX as starting materials.

In this chapter, I report that the Li^+ conducting anti-perovskite structured Li_2OHBr is synthesized at room temperature just by dry ball milling method using LiOH and LiBr as starting materials. The sample also has an ionic conductivity in the order of 10^{-6} S cm^{-1}, showing good agreement with some of the already reported values of Li_2OHBr synthesized through the heating process above 300 ˚C. The advantages of this solid-state reaction are its very simple and moisture-free easy process, which makes an advantage for scale-up production and reduction of cost.

2.2 Experimental

Li_2OHBr used in this work was synthesized by solid-state dry ball milling technique. The inorganic precursors were lithium bromide (LiBr, > 99 %, Kanto Chemical) and lithium hydroxide monohydrate ($LiOH{\cdot}H_2O$, > 99 %, Fluka). $LiOH{\cdot}H_2O$ was heated at 200˚C for 20 hours under Ar atmosphere to form LiOH. Both LiOH (9.0 mmol) and LiBr (9.0 mmol) were loaded into a 12 mL zirconia ball milling jar with 15 g of 5 mm (in diameter) zirconia balls and sealed inside the glove box. The ball-milling (Fritsch, planetary micro mill Pulverisette 7) was carried out at room temperature for 48 hours at 700 RPM, to expect the following chemical reaction,

$$LiOH + LiBr = Li_2OHBr \ldots (1)$$

The author had tried to prepare the crystalline LiRAP under more mild conditions, (24 hours at 350 RPM, 24 hours at 700 RPM) but they remained impurity phase and then this mixing condition was optimized as the mildest condition in our experimental setup.

The crystal structure of the prepared samples was analyzed by synchrotron powder X-ray diffraction (PXRD) measurements (BL5S2 of Aichi Synchrotron Radiation Center) with

wavelength λ = 1.033 Å between 10˚ and 40˚ using two-dimensional detector PILATUS 100K. During the measurements, samples were stored in soda-lime glass capillaries (0.5 mm in diameter) sealed in an Ar-filled glove box (dew point < –80 °C). The lattice constant of the sample was calculated by Rietveld analysis. Differential scanning calorimetry (DSC) measurement (Hitachi DSC, 7000X) was carried out to investigate the melting point of the Li_2OHBr. Powders of Li_2OHBr were sealed in an aluminum pan inside an Ar-filled glove box, and the measurement was conducted at 5 ˚C min^{-1} between 200 ˚C and 300 ˚C. Fourier transform infrared (FT-IR: Thermo Scientific Nicolet iS50) spectra were measured to investigate the existing state of hydrogen inside the Li_2OHBr, where the equipment was located inside a dry room facility (typical dew point is below –50 ˚C) at the National Institute for Materials Science (NIMS), and all the samples were treated in it.

Electrochemical impedance spectroscopy (EIS) was carried out using an impedance analyzer (BioLogic, VMP3) to investigate the ionic conductivity of the Li_2OHBr. Powders of the Li_2OHBr were pressed into a pellet with a diameter of 7 mm at 5.1×10^2 MPa for 5 minutes inside an Ar-filled glove box (dew point < –80 °C), where gold foils (2.5 μm in thickness) were set on both sides as current collectors. Typical pellet thickness was 0.7–1.0 mm. EIS of the resultant Au/Li_2OHBr/Au symmetrical blocking electrodes cell was measured in the frequency range of 500 kHz–100 mHz with an AC amplitude of 25 mV at 25, 50, 75, 100, 125, and 150˚C. Also, Li/Li_2OHBr/Li symmetrical non-blocking electrodes cell was prepared to investigate conductive carrier species inside the sample and the stability of Li_2OHBr against Li plating/stripping reactions. Initially, pellets without gold foils were made by the above-mentioned conditions. Then, thin films of Li were deposited on both sides of the pellets by vacuum evaporation attached in an Ar-filled grove box, and then Li foils (1 mm in thickness) were further mounted on the Li films. Lithium plating/stripping reactions of the resultant Li/Li_2OHBr/Li cells were carried out at 25 ˚C with 5 μA cm^{-2} or 60 ˚C with 50 μA cm^{-2} for

100 cycles inside an Ar-filled glove box (dew point < –80 °C). The plating/stripping thickness in each reaction was 10 nm, assuming that uniform plating/stripping reaction takes place in each cycle.

2.3 Results and Discussion

Figure 2.1(a) shows the synchrotron PXRD patterns of the resultant sample and starting materials (LiOH and LiBr) in addition to the simulated data of cubic-phase Li_2OHBr. The resultant sample provided diffraction peaks at 2θ = 14.6, 20.8, 25.5, 29.6, 33.1, and 36.4˚. All the peaks were in good agreement with the simulated data of Li_2OHBr, and other peaks were not detected. This indicates that the starting materials are well reacted to form cubic-phase anti-perovskite Li_2OHBr, and there are no impurities. The lattice constant of the sample was calculated to be 4.046 Å, which is consistent with the reported value of 4.046 Å [7]. Figure 2.1(b) shows the FT-IR spectra of the resultant sample, LiOH, and $LiOH{\cdot}H_2O$. A broad peak derived from the crystalized water was observed in $LiOH{\cdot}H_2O$ around 2800 cm^{-1} (Figure 2.1(b)). On the other hand, such a broad peak was not observed in LiOH, indicating that crystallized water was successfully removed by heating at 200 ˚C for 20 hours. The resultant sample also did not show such a broad peak, and only sharp O-H stretching peaks were observed at 3600 cm^{-1} [8, 9]. This result indicates that the sample is not dehydrated Li_3OBr and that H is contained only as the crystal.

Figure 2.2 shows the DSC curve of the sample. During the heating process, two peaks were observed. To our best knowledge, there are no reports about the phase behavior of Li_2OHBr in this temperature region, so details of phase behavior are still unclear. However, according to the previous report about other LiRAP, it is suggested that the first peak at 247 ˚C corresponds to phase transition and the second peak at 254 ˚C corresponds to melting point [10]. It was confirmed that the sample was melted on a hot plate at 254 ˚C. During the cooling

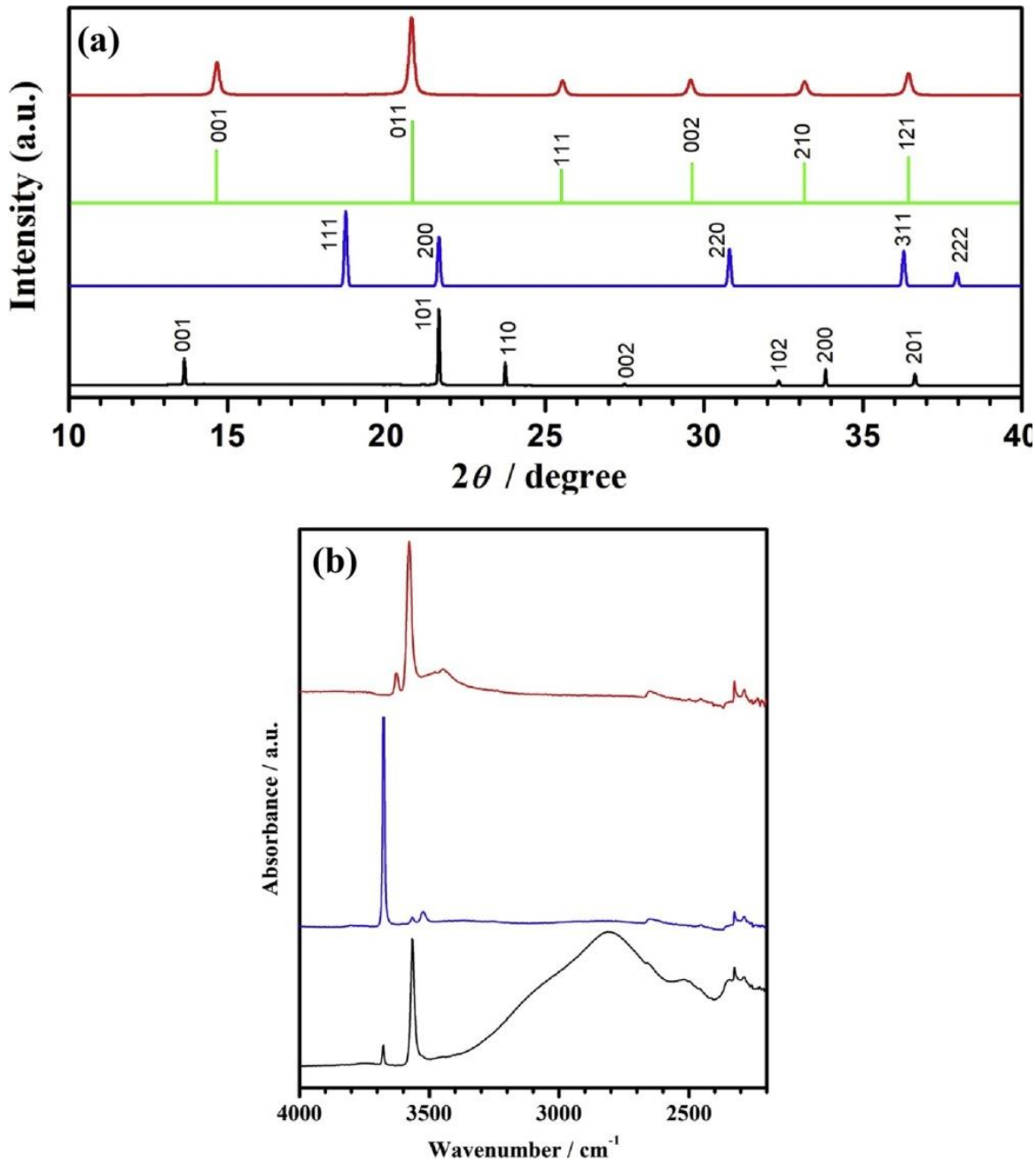

Figure 2.1 (a) Synchrotron PXRD patterns of the synthesized sample (red), simulation of cubic Li_2OHBr with space group *Pm-3m* from JCPDS card no. 35-241 (green), LiOH (blue) and LiBr (black). (b) FT-IR spectra of the synthesized sample (red), LiOH (blue) and $LiOH \cdot H_2O$ (black).

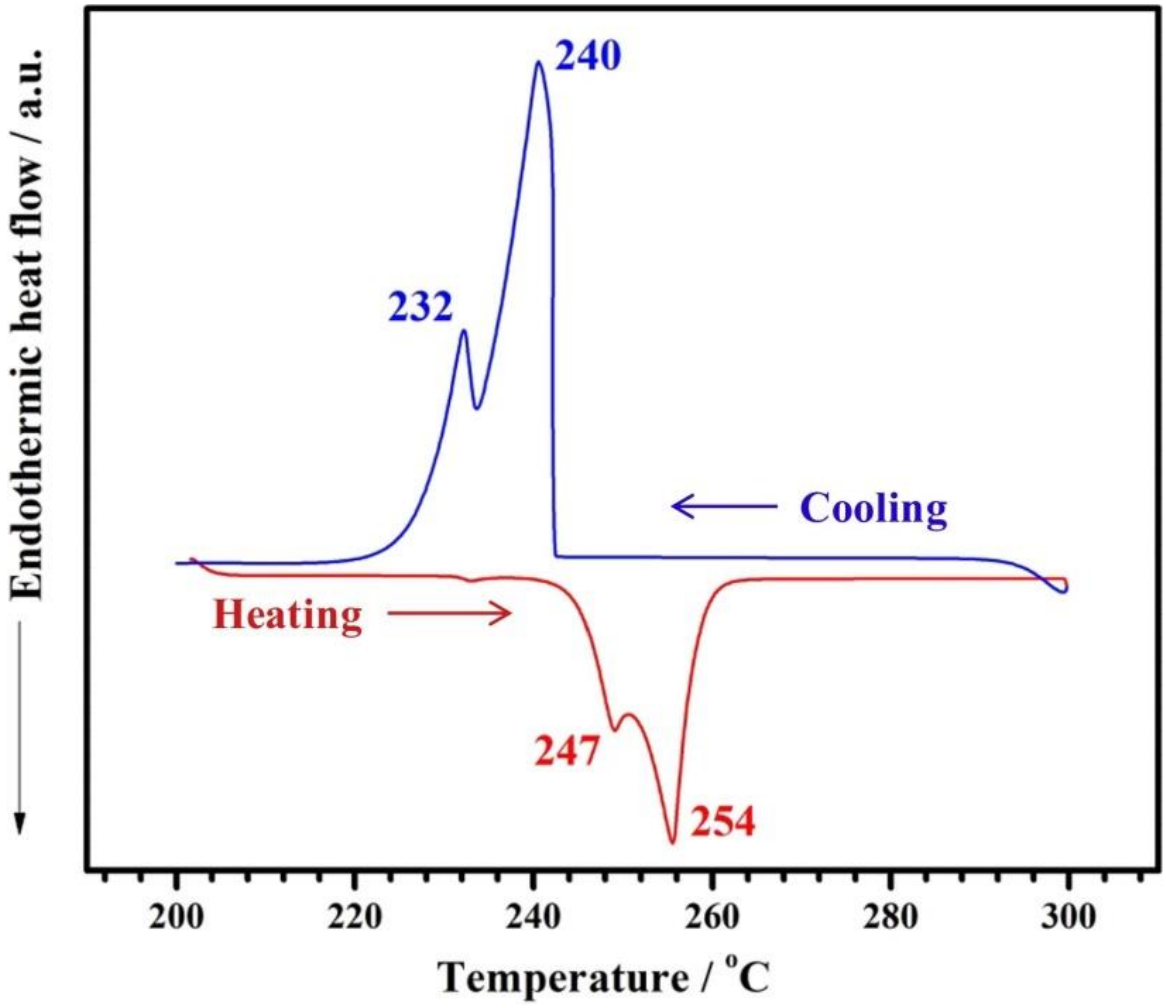

Figure 2.2. Differential scanning calorimetry (DSC) curves of Li_2OHBr sample during heating (red) and cooling (blue), at 5 °C min^{-1}.

process, two peaks were observed at 240 ˚C and 232 ˚C, which has been assigned to nucleation and crystallization peak, respectively [10]. These results indicate that the sample has a low melting point as with previous LiRAP and reversible melting/crystallization reaction takes place between 200 ˚C and 300 ˚C.

Figure 2.3(a) shows the Nyquist plots of Au/Li_2OHBr/Au symmetrical blocking electrodes cell measured at 25˚C. The relative density of Li_2OHBr pellets was estimated to be 95 %, which is comparable to sulfide-based SEs [11]. The Nyquist plot showed only one semicircular arc in the higher frequency range, followed by a capacitive straight line to the real axis. In past, authors have claimed that the LiRAP has relatively large grain boundary resistance and the grain boundary contribution dominates the total Li^+ conductivity [7, 12]. Unfortunately, the semicircular arc was not separated into in-grain and grain boundary resistance and appeared only as one semicircular arc. This situation was the same even after the sample was recrystallized after heating the sample to 300 ˚C. Also, the capacitance of the semicircular arc was calculated to be ca. 500 pF and such large capacitance value is considered to originate from grain boundary resistance [13]. The author speculates that this semicircular arc mainly originates from grain boundary resistance. The total ionic conductivity was estimated from the diameter of this semicircular arc, and the value was calculated to be1.1×10^{-6} S cm^{-1} at 25 ˚C, which was consistent with the reported value of Li_2OHBr [14]. The resistance decreased with increasing the temperature as shown in the inset of Figure 2.3(a), and the values followed Arrhenius-type temperature dependency as shown in Figure 2.3(b) between 25 and 150˚C. The apparent activation energy was evaluated from the slope to be 0.54 eV. Based on first-principles simulations [12] and experimental [13] values, the activation energy of this order is considered to originate from the grain boundaries which is due to the large migration energy. Both the ionic conductivity and activation energy of recrystallized sample was almost similar value of 1.1×10^{-6} S cm^{-1} at 25 ˚C and 0.55 eV, respectively. Thus,

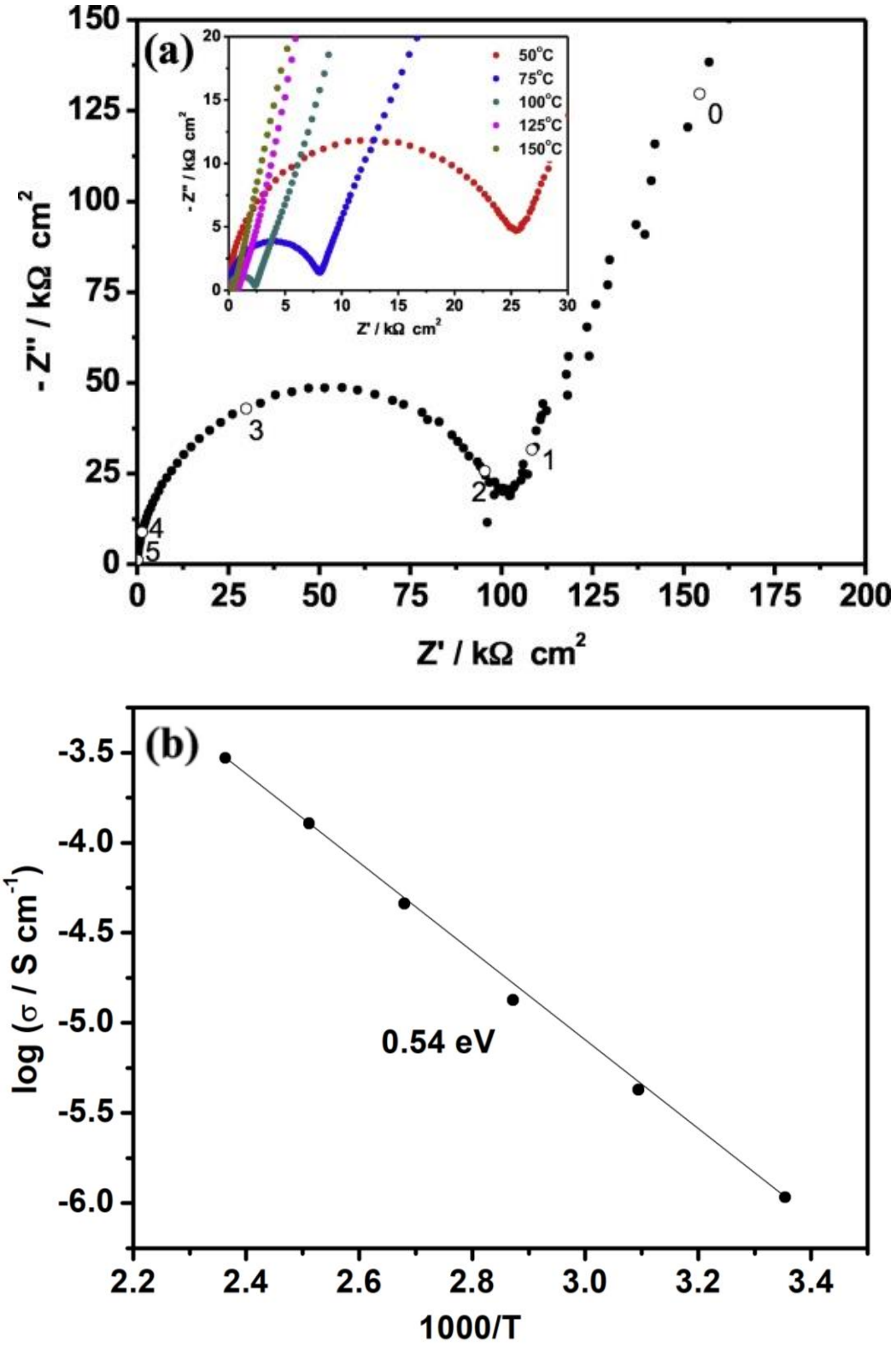

Figure 2.3 (a) EIS Nyquist plot of Au/Li_2OHBr/Au symmetrical cell measured at 25 °C. The inset shows the EIS measured at different temperatures between 25 and 150 °C. (b) Arrhenius plot of log(σ) versus 1000/T of Li_2OHBr during heating. The slope from the plot was used to estimate the activation energy E_a.

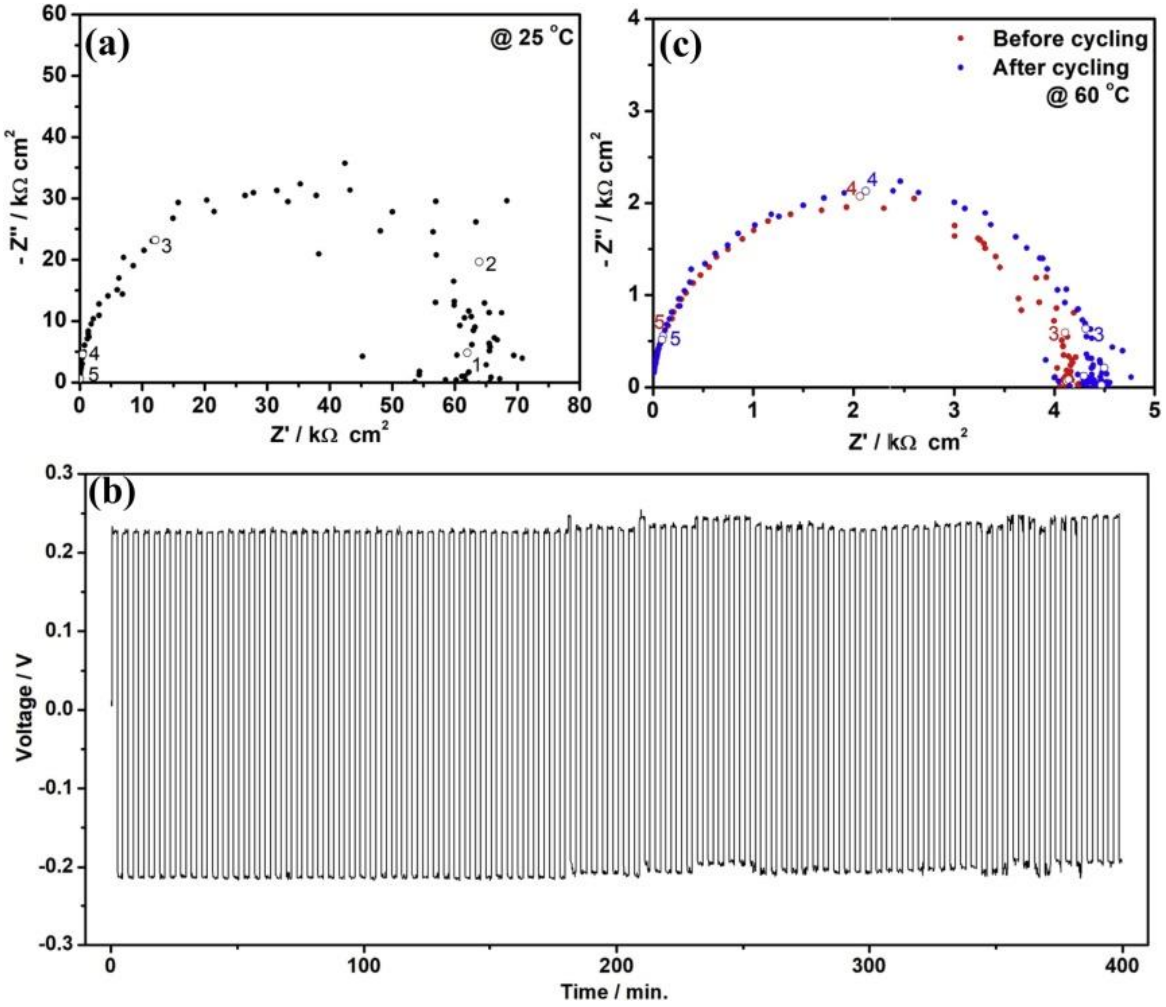

Figure 2.4. (a) EIS Nyquist plot of Li/Li_2OHBr/Li symmetrical cell measured at 25 °C. (b) Li plating/stripping cycles at a current density of 50 μA cm^{-2} for 100 cycles at 60 °C. (c) EIS Nyquist plot of Li/Li_2OHBr/Li symmetrical cell measured at 60 °C before (red) and after (blue) 100 cycles of Li plating/stripping reactions.

Li_2OHBr prepared by room temperature ball milling process will be basically formed as an equilibrium state.

Figure 2.4(a) shows the Nyquist plots of Li/Li_2OHBr/Li symmetrical non-blocking electrodes cell measured at 25 ˚C. One semicircular arc was observed, and the spectrum settled on the real axis at the lower frequency region, and Li/Li_2OHBr interfacial resistance was not observed as a separated semicircular arc. Assuming that this one semicircular arc originates from ionic conductivity, the value was estimated to be 1.1×10^{-6} S cm^{-1}, which is consistent with the value measured by using Au/Li_2OHBr/Au symmetrical cell. Therefore, it is expected that interfacial resistance at Li/Li_2OHBr is not large. Figure 2.4(b) shows the lithium plating/stripping curves at 60 ˚C with a current density of 50 μA cm^{-2}. The plating/stripping reactions were repeated for 100 cycles. The average value of the overvoltage during the Li plating/stripping reactions was ca. 0.22 V, while the ohmic resistance of the Li_2OHBr in a unit area is 4.3 kΩ cm^2. Thus, this overvoltage almost originates from the ohmic resistance of Li_2OHBr, and then the main carrier ions in Li_2OHBr will be Li^+. Figure 2.4(c) shows the Nyquist plot before and after Li plating/stripping reactions shown in Figure 2.4(b). The diameter of the semicircular arc increased by ca. 7 % after the cycles. On the other hand, when the plating/stripping reactions were carried out at 25 ˚C with a current density of 5 μA cm^{-2}, such an increase was not observed at all. Because lithium plating/stripping amount was very thin of 10 nm in each measurement, this increase in interfacial resistivity may arise from the formation of a reaction layer around Li/Li_2OHBr rather than mechanical contact loss due to void formation around the Li/Li_2OHBr, as the case of Li/Li_3OCl interface [15].

2.4 Conclusion

Cubic-phase anti-perovskite-structured Li_2OHBr was synthesized at room temperature just by the ball milling method. Both PXRD and FT-IR measurements revealed that the resultant

Li_2OHBr is a single phase and containing H in the crystal. The ionic conductivity of the Li_2OHBr was 1.1×10^{-6} S cm^{-1} at 25 ˚C with the activation energy of 0.54 eV, and the main conductive carrier was confirmed to be Li^+. Also, Li plating/stripping reactions were carried out at 60 ˚C with a current density of 50 μA cm^{-2}, and stable Li plating/stripping reactions were repeated for 100 cycles through the formation of the reaction layer was suggested because of a slight increase of resistance. Our proposing preparation method provides partially hydrated LiRAP very simply under dry conditions, which will be effective in investigating ion-conductive properties in detail.

References

1) M. Monchak, T. Hupfer, A. Senyshyn, H. Boysen, D. Chernyshov, T. Hansen, K. G. Schell, E. C. Bucharsky, M. J. Hoffmann and H. Ehrenberg, Inorg. Chem. 55 (2016) 2941.
2) Y. Inaguma, C. Liquan, M. Itoh, T. Nakamura, T. Uchida, H. Ikuta and W. Wakihara, Solid State Commun. 86 (1993) 689.
3) R. Murugan, V. Thangadurai and W. Weppner, Angew. Chem. Int. Ed. 46 (2007) 7778.
4) J. Kim, J. Kim, M. Avdeev, H. Yun and S.-J. Kim, J. Mater. Chem. A. 6 (2018) 22478.
5) Z. Gao, H. Sun, L. Fu, F. Ye, Y. Zhang, W. Luo and Y. Huang, Adv. Mater. 30 (2018) 1705702.
6) X.J. Lu, G. Wu, J.W. Howard, A.P. Chen, Y.S. Zhao, L.L. Daemen and Q.X. Jia, Chem. Commun. 50 (2014) 11520.
7) S. Li, J. Zhu, Y. Wang, J. W. Howard, X. Lü, Y. Li, R. S. Kumar, L. Wang, L. L. Daemen and Y. Zhao, Solid State Ionics 284 (2016) 14.

8) G. Schwering, A. Honnerscheid, L. V. Wullen and M. Jansen, ChemPhysChem 4 (2003) 343.

9) Y. Li, W. Zhou, S. Xin, S. Li, J. Zhu, X. Lu, Z. Cui, Q. Jia, J. Zhou, Y. Zhao and J. B. Goodenough, Angew. Chem. Int. Ed. 55 (2016) 9965.

10) Y. Zhao and L. L. Daemen, J. Am. Chem. Soc., 134 (2012) 15042.

11) A. Sakuda, A. Hayashi and M. Tatsumisago, Sci. Rep. 3 (2013) 2261.

12) B. Chen, C. Xu and J. Zhou, J. Electrochem. Soc. 165 (2018) A3946.

13) I. Hanghofer, G. J. Redhammer, S. RohdeIlie, I. Hanzu, A. Senyshyn, H. M. R. Wilkening and D. Rettenwander, Chem. Mater. 30 (2018) 8134.

14) A.-Y. Song, Y. Xiao, Dr. K. Turcheniuk, P. Upadhya, A. Ramanujapuram, J. Benson, A. Magasinski, M. Olguin, L. Meda, O. Borodin and G. Yushin, Adv. Energy Mater. 8 (2018) 1700971.

15) X. Lü, G. Wu, J. W. Howard, A. Chen, Y. Zhao, L. L. Daemena and Q. Jia, Chem. Commun. 50 (2014) 11520.

16) Z.D. Hood, H. Wang, A.S. Pandian, J.K. Keum and C. Liang, J. Am. Chem. Soc. 138 (2016) 1768.

17) P. Hartwig, A. Rabeau and W. Weppner, J. Less Common Met. 78 (1981) 227.

Chapter 3

Synthesis of the Metastable Cubic Phase of Li_2OHCl by a Mechanochemical Method

3.1 Introduction

Lithium-ion conductors have attracted broad interest due to their potential application to all-solid-state rechargeable lithium batteries [1]. The ionic conductivity of solid electrolytes strongly affects the performance of the battery. Although several crystalline oxide-based solid electrolytes such as $Li_7La_3Zr_2O_{12}$ [2], $Li_{1+x}Al_xTi_{2-x}(PO_4)_3$ [3], $La_{2/3-x}Li_{3x}TiO_3$[4], and LiTa2PO8[5] have achieved Li^+ conductivity of 10^{-4} S cm^{-1} at room temperature, they are hard and fragile ceramics prepared through high-temperature firing. Thus, it is not easy to form well-adhered interfaces between those solid electrolytes and electrode-active materials.

Recently, oxyhalide-based solid electrolytes $Li_{3-x}OH_xX$ (X = Cl and Br) with anti-perovskite-type structure have attracted attention due to relatively high ionic conductivity and soft nature [6]. In the anti-perovskite structure, anions are bcc-packed, and theoretical calculations suggest that such bcc-packed anion sub-lattice provides fast-ion conductivity [7]. However, there is still uncertainty for the improvement of the ionic conductivity of oxyhalide-based solid electrolytes. One reason arises from the difficulties to fabricate pure samples [8,9]. To overcome this problem, Li_2OHBr has been prepared by mechanochemical synthesis at room temperature as mentioned in chapter 2, which is a simple and easy method to control composition [10]. However, it is not clear how the crystalline phase is formed in the sample.

To understand this phenomenon in detail, the author has focused on the preparation of Li_2OHCl in this chapter. It has been reported that Li_2OHCl forms the cubic phase above 35 ˚C and shows the ionic conductivity of 6×10^{-5} S cm^{-1} at 37 ˚C [11] Below 35 ˚C, however, the

ionic conductivity drastically drops down to 2×10^{-9} S cm^{-1} due to the structural phase transition into the orthorhombic phase. The theoretical calculation also supports such phase transition between cubic *Pm*-3*m* structure and orthorhombic $Pmc2_1$ structure [12]. According to this calculation, the higher ionic conductivity of the cubic phase than the orthorhombic phase can be explained in terms of highly correlated Li ion motion associated with OH bond orientation. In this chapter, the cubic phase of Li_2OHCl is formed by mechanochemical synthesis as in chapter 2.

3.2 Experimental

Li_2OHCl used in this work was synthesized by a mechanochemical method using LiCl and LiOH as starting materials. LiCl (> 99 %) was purchased from FUJIFILM Wako Pure Chemical Corporation and used without further purification. LiOH was prepared by heating $LiOH \cdot H_2O$ (> 99 %, Fluka) at 250 ˚C for 6 h to remove water. 15.1 mmol of LiCl and 15.1 mmol of LiOH were mechanically milled in a 12-mL zirconia pot with 15 g of zirconia balls (5 mm in diameter) using a planetary ball mill (Fritsch, Pulverisette 7) at 700 RPM for 72 hours. All processes were carried out under a dry Ar atmosphere.

Variable-temperature synchrotron powder X-ray diffraction (PXRD) measurements were conducted at the BL5S2 of Aichi Synchrotron Radiation Center with synchrotron radiation of λ = 1.033 Å. The powdered sample was loaded into soda-lime glass capillaries (0.5 mm in diameter). The measurement temperature was controlled between 30 and 200 ˚C using a nitrogen gas flow. Rietveld analyses were performed using GSAS-II software [13]. The initial structural parameters of cubic *Pm*-3*m* structure and orthorhombic $Pmc2_1$ structure were taken from the previous experimental and theoretical reports [9,12]. The pseudo-Voight function was used to fit the diffraction peaks, and the background was generated using Chebyshev polynomial with 18 terms.

For alternating current (AC) impedance spectroscopy, pelletized sample sandwiched between gold foil (0.025 mm in thickness) was prepared by pressurizing powdered sample under 3.6×10^2 MPa for 3 min at room temperature. The typical thickness and diameter of the pellet were 1 and 7 mm, respectively. AC impedance spectroscopy was performed using an impedance analyzer (Bio-Logic, VMP3) in a frequency range of 500 kHz to 0.1 Hz at an applied voltage of 10 mV. The measurement temperature was controlled between 25 and 200 ˚C using a constant temperature dry-block bath (EYELA, MG-2200).

3.3 Result and Discussion

Figure 3.1a shows the result of Rietveld analysis on the synchrotron PXRD pattern of the as-prepared Li_2OHCl measured at 30 ˚C. The observed diffraction pattern could be well fitted with the cubic *Pm*-3*m* structure of Li_2OHCl with a lattice constant of a = 3.90317(2) Å, and other parameters are shown in Table 3.1. Occupancy factors of O and Cl were fixed to 1 due to unreliable refined values larger than 1 (1.08 and 1.06, respectively). Occupancy factors of Li and H were refined under constraint to maintain a chemical composition of $Li_{3-x}OH_xCl$, and the refined composition was $Li_{1.88}OH_{1.12}Cl$. Although a small discrepancy from the stoichiometry can be expected from the existence of a tiny amount of unreacted LiCl, it should be noted that the reliability of refinements for light-element parameters using XRD is relatively low, and neutron diffraction will be desirable to determine actual composition. However, it is worth noting that although Li_2OHCl usually forms the orthorhombic phase below 35 ˚C as mentioned above [11], Li_2OHCl synthesized by a mechanochemical method in this work forms the cubic phase at 30 ˚C.

Figure 3.2a and 3.2b show the results of variable-temperature synchrotron PXRD measurements. On the first cycle between 30 and 200 ˚C as shown in Figure 3.2a, the initial cubic phase remained during heating up to 200 ˚C and subsequent cooling down to 40 ˚C. On

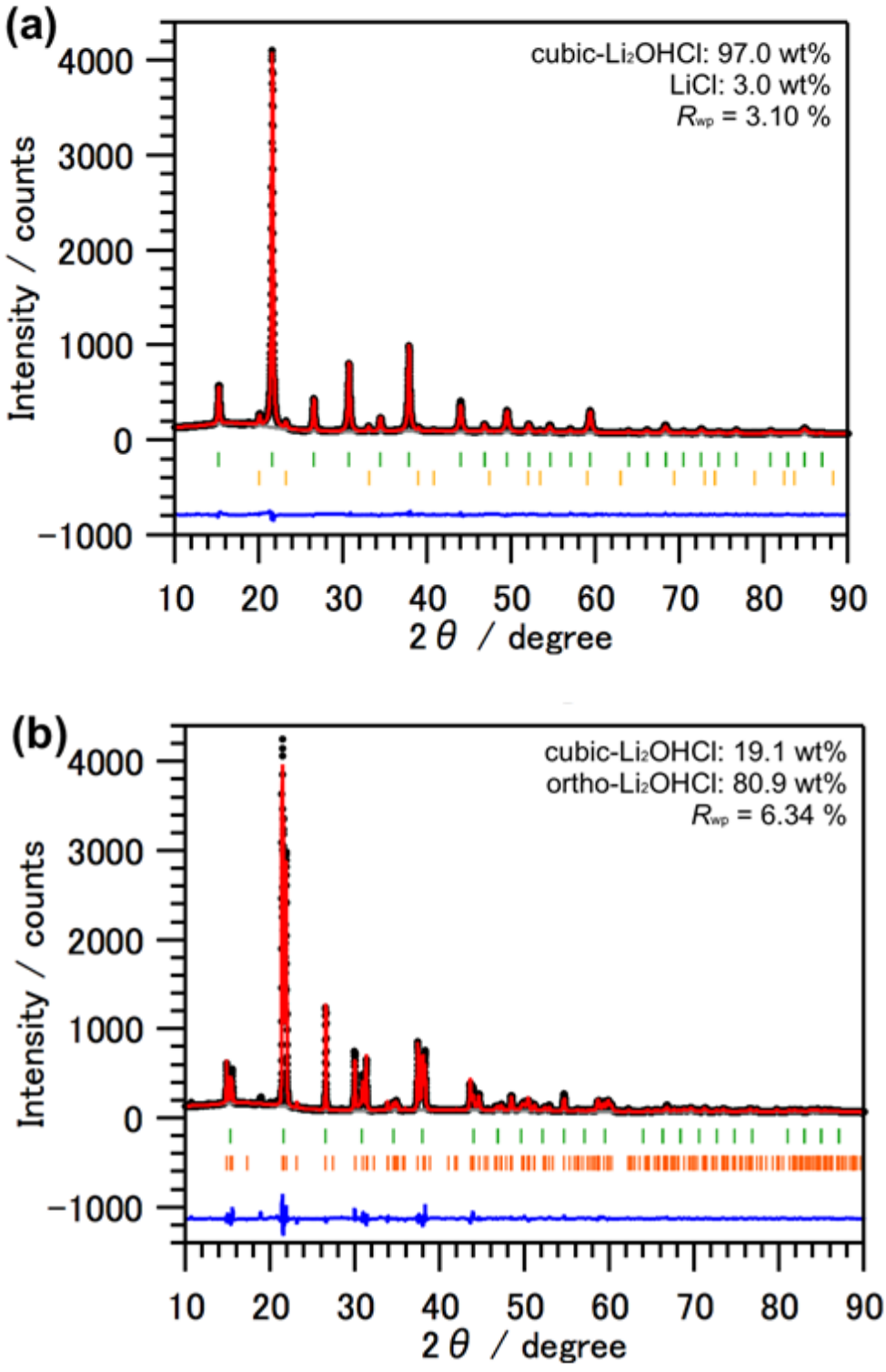

Figure 3.1. Rietveld refinements on the synchrotron PXRD patterns of Li_2OHCl measured at 30 ˚C (a) before and (b) after heating up to 200 ˚C. Black circles: experimental, red curves: fitting, blue curves: residual, gray curves: background, green bars: peak positions for the cubic phase Li_2OHCl, orange bars: peak positions for the orthorhombic phase Li_2OHCl, yellow bars: peak positions for LiCl.

Table 3.1. Fractional Coordinates, Isotropic Displacement, and Occupancy Factors for the Cubic Pm-3m (No. 221) Structure of the As-Prepared Li_2OHCl Measured at 30 °C by Synchrotron PXRD[a]

atom	Wyckoff	*x*	*y*	*z*	U_{iso}	occupancy
O	1a	0	0	0	0.0213(2)	1
Cl	1b	1/2	1/2	1/2	0.0191(1)	1
Li	3d	1/2	0	0	0.0691(8)	0.628(4)
H	8g	0.1279	0.1279	0.1279	0.025	0.140(2)

[a]The fractional coordinates of all of the atoms, occupancy factors of oxygen and chlorine,

Table 3.2. Fractional Coordinates, Isotropic Displacement, and Occupancy Factors for the Orthorhombic Pmc21 (No. 26) Structure of the Annealed Li_2OHCl Measured at 30 °C by Synchrotron PXRD[a]

atom	Wyckoff	*x*	*y*	*z*	U_{iso}	occupancy
O	2a	0	–0.024	0	0.0136(5)	1
Cl	2b	1/2	1/2	1/4	0.0138(3)	1
Li1	2a	0	0.001	1/4	0.0304(15)	1
Li2	2b	1/2	0.086	0	0.025	1
H	2a	0	0.699	0	0.025	1

[a]The fractional coordinates and occupancies for all of the atoms and isotropic displacements of Li2 and hydrogen were fixed in the refinement.

the other hand, the diffraction pattern drastically changed at 30 ˚C on the cooling process, suggesting a structural phase transition. Rietveld analysis on this newly observed diffraction pattern revealed that the orthorhombic $Pmc2_1$ structure of Li_2OHCl with lattice constants of a = 3.87601(6) Å, b = 3.82796(5) Å and c = 7.99425(11) Å formed at 30 ˚C after heating up to 200 ˚C (Figure 3.1b and Table 3.2). Atomic parameters of the minor cubic phase were fixed to the values in Table 3.1, and occupancy factors of the major orthorhombic phase were fixed to 1 due to unreliable refined values larger than 1. The detail of this phase transition was investigated on the second cycle of variable-temperature synchrotron PXRD measurements between 30 and 40 ˚C as shown in Figure 3.2b. On the heating process, the orthorhombic phase gradually changed to the cubic phase between 36 and 40 ˚C, whereas the cubic phase changed to the orthorhombic phase between 32 and 30 ˚C during the cooling process. From Rietveld analysis, the fractions of the cubic phase were calculated and plotted against temperature in Figure 3.2c. Figure 3.2c clearly shows that the transition temperature is between 30 and 40 ˚C. The small hysteresis between the heating and cooling processes is reasonable considering that this phase transition is thought to be in first order.

The resistance was estimated from the diameter of this semi-arc, and the total ionic conductivity was calculated from this resistance based on pellet thickness and diameter. The Arrhenius plots of total ionic conductivity of Li_2OHCl were plotted in Figure 3.3. The initial ionic conductivity was 2.6×10^{-6} S cm^{-1} at 25 ˚C before heating. The ionic conductivity increased with elevated temperature and reached 4.1×10^{-3} S cm^{-1} at 200 ˚C. The activation energy estimated from the Arrhenius equation was 0.54 eV between 25 and 200 ˚C, showing good agreement with the previous reports of the cubic phase of Li_2OHCl [11,14]. During cooling, the ionic conductivity decreased with an activation energy of 0.53 eV down to 40 ˚C and drastically dropped down to 1.4×10^{-7} S cm^{-1} at 25 ˚C. This sudden decrease of the ionic conductivity originates from the structural phase transition from the cubic to orthorhombic

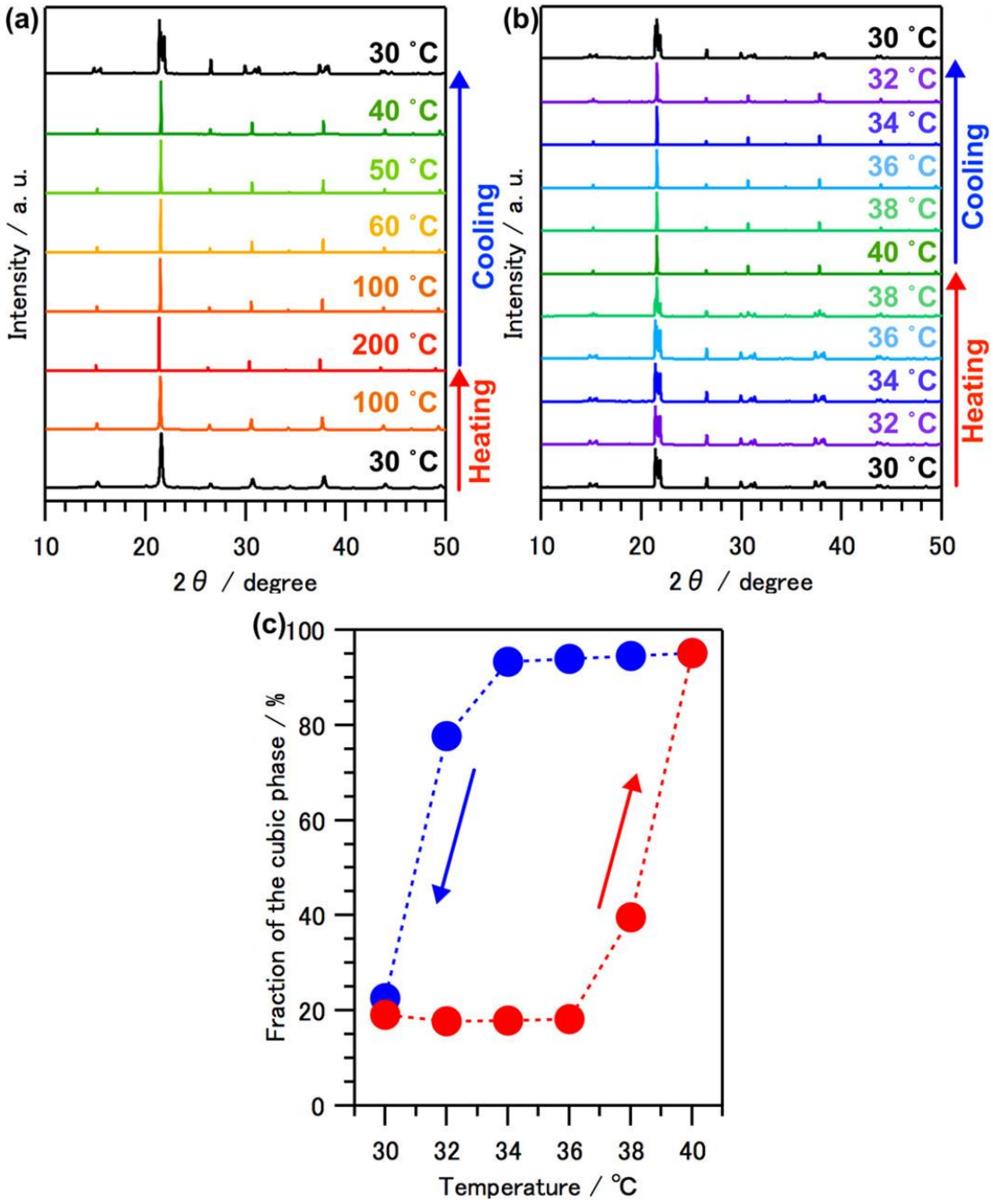

Figure 3.2. Variable-temperature synchrotron PXRD patterns (a) on the first cycle between 30 and 200 ˚C, and (b) on the second cycle between 30 and 40 ˚C. (c) Temperature dependence of cubic-phase fraction on the second heating-cooling cycle estimated by

phase observed in variable-temperature synchrotron PXRD measurements (Figure 3.2).

Both PXRD and AC impedance measurements clearly show that Li_2OHCl synthesized by mechanochemical method forms cubic phase at room temperature, although the orthorhombic phase is usually the most stable phase at room temperature [11]. It has been reported that the metastable phase is synthesized by a mechanochemical method in various materials, such as metal alloys [15], metal hydrides [16], and metal oxides [17]. Materials synthesized by the mechanochemical method generally have low crystallinity compared to those synthesized by the sintering process, and hence it can be expected that the crystallinity affects the phase behavior. The temperature dependence for the crystallite size of the cubic phase of Li_2OHCl during the first heating-cooling process was evaluated from 110 diffractions (around 21.5˚ in Figure 3.2a) using Scherrer's equation (1),

$$D = \frac{K\lambda}{\beta \cos\theta} \quad \ldots (1)$$

where D is crystallite size, K is the shape factor (here 0.9 is adopted), λ is the wavelength of radiated X-ray, β is full width at half the maximum of diffraction peak, and θ is Bragg angle. D was calculated to be 37 nm for the as-prepared Li_2OHCl, while the value increased to 176 nm after the first heating-cooling process. This indicates that crystallite size increase by the first heating-cooling process. It has been reported that materials with nano-sized crystallite less than 100 nm show different phase behavior from bulk materials, probably originating from their large surface energy [18]. In our Li_2OHCl case, stabilization of the cubic phase is thought to be derived from its small crystallite size. During the first heating process, crystal growth proceeds, and the resultant Li_2OHCl will behave as bulk material as have been reported in previous reports [11].

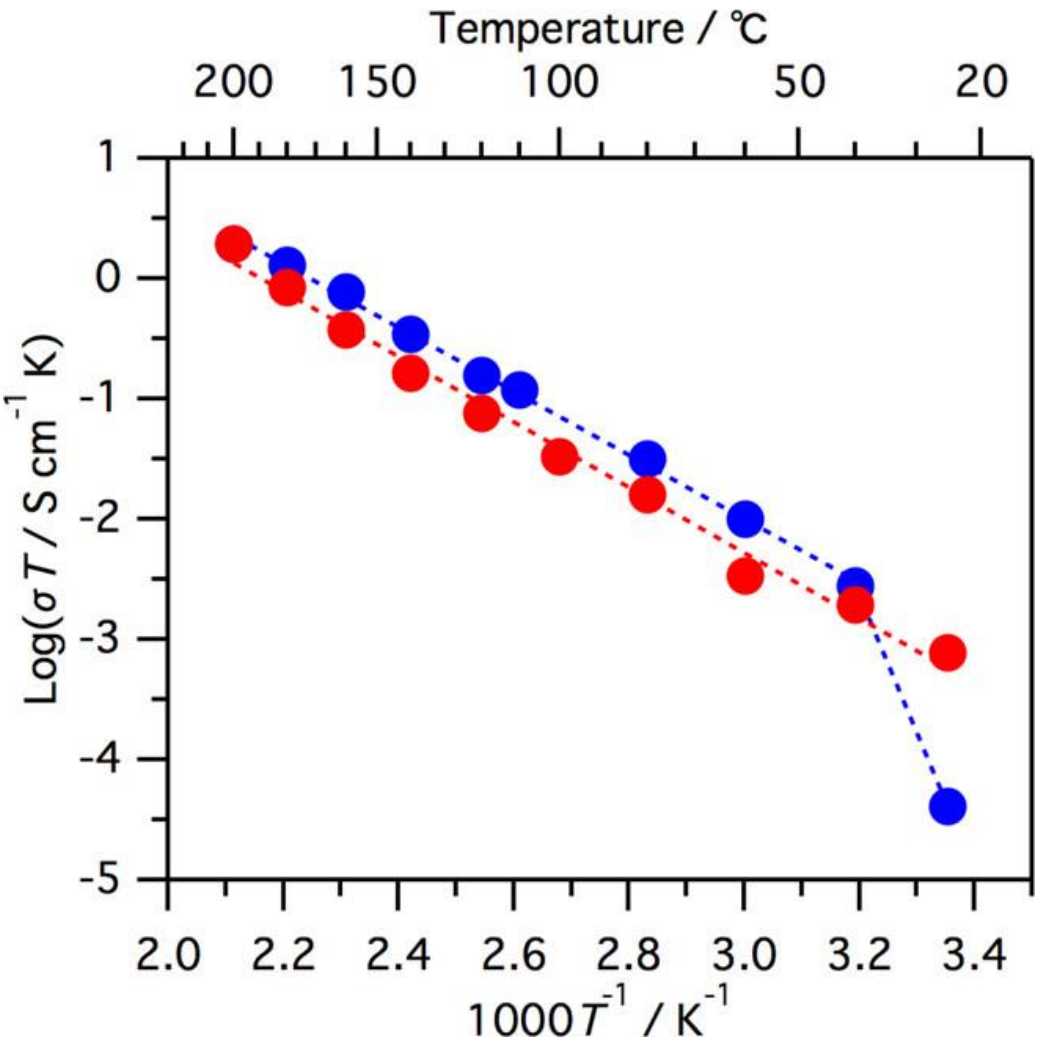

Figure 3.3. Arrhenius plots of total ionic conductivity of Li_2OHCl during first heating (red) and cooling (blue) cycle.

3.4 Conclusion

In summary, the author has formed cubic-phase Li_2OHCl at room temperature by mechanochemical synthesis and clarified that the cubic Li_2OHCl obtained one order higher ionic conductivity at 25 ˚C than that of the thermodynamically stable orthorhombic Li_2OHCl formed through heating-cooling cycle between 30-200 ˚C. This stabilization of the metastable phase will originate from smaller-sized crystallite uniquely formed through mechanochemical synthesis.

References

1) J. C. Bachman, S. Muy, A. Grimaud, H.-H. Chang, N. Pour, S. F. Lux, O. Paschos, F. Maglia, S. Lupart, P. Lamp, L. Giordano and Y. Shao-Horn, Chem. Rev. 116 (2016) 140. (b) F. Zheng, M. Kotobuki, S. Song, M. O. Lai and L. Lu, J. Power Sources 389 (2018) 198.
2) R. Murugan, V. Thangadurai and W. Weppner, Angew. Chem. Int. Ed. 46 (2007) 7778.
3) H. Aono, E. Sugimoto, Y. Sadaoka, N. Imanaka and G. Adachi, J. Electrochem. Soc. 136 (1989) 590.
4) Y. Inaguma, C. Liquan, M. Itoh, T. Nakamura, T. Uchida, H. Ikuta and M. Wakihara, Solid State Commun. 86 (1993) 689.
5) J. Kim, J. Kim, M. Avdeev, H. Yuna and S. J. Kim, J. Mater. Chem. A 6 (2018) 22478.
6) (a) Y. Zhao and L. L. Daemen, J. Am. Chem. Soc. 134 (2012) 15042. (b) Y. Li, W. Zhou, S. Xin, S. Li, J.Zhu, X. Lî, Z. Cui, Q. Jia, J. Zhou, Y. Zhao and J. B Goodenough, Angew. Chem. Int. Ed. 55 (2016) 9965.
7) Y. Wang, W. D. Richards, S. P. Ong, L. J. Miara, J. C. Kim, Y. Mo and G. Ceder, Nat. Mater. 14 (2015) 1026.

8) S. Li, J. Zhu, Y. Wang, J. W. Howard, X. Lü, Y. Li, R. S. Kumar, L. Wang, L. L. Daemen and Y. Zhao, Solid State Ionics 284 (2016) 14.

9) I. Hanghofer, G. J. Redhammer, S. Rohde, I. Hanzu, A. Senyshyn, H. M. R. Wilkening and D. Rettenwander, Chem. Mater. 30 (2018) 8134.

10) M. K. Sugumar, T. Yamamoto, M. Motoyama and Y. Iriyama, Solid State Ionics 349 (2020) 115298.

11) G. Schwering, A. Honnerscheid, L.V. Wullen and M. Jansen, ChemPhysChem 4 (2003) 343.

12) J. Howard, Z. D. Hood and N. A. Holzwarth, Phys. Rev. Materials 1 (2017) 075406.

13) B. H. Toby and R. B. Von Greele, J. Appl. Cryst. 46 (2013) 544.

14) Z. D. Hood, H. Wang, A. S. Pandian, J. K. Keum and C. Liang, J. Am. Chem. Soc. 138 (2016) 1768.

15) (a) H. J. Fecht, G. Han, Z. Fu and W. L. Johnson, J. Appl. Phys. 67 (1990) 1744. (b) E. Gaffet, C. Louison, M. Harmelin and F. Faudot, Mater. Sci. Eng. A, 134 (1991) 1380.

16) (a) J. Huot, G. Liang, S. Boily, A. V. Neste and R. Schulz, J. Alloys Compd. 293 (1999) 495. (b) M. S. El-Eskandarany, M. Banyan and F. Al-Ajmi, RSC Adv. 8 (2018) 32003.

17) (a) P. N. Kuznetsov, L. I. Kuznetsova, A. M. Zhyzhaev, G. L. Pashkov and V. V. Boldyrev, Appl. Catal. A-Gen. 227 (2002) 299. (b) K. O. Hara, E. Yamasue, H. Okumura and K. N. Ishihara, J. Phys.: Conf. Ser. 144 (2009) 012021.

18) (a) R. Makiura, T. Yonemura, T. Yamada, M. Yamauchi, R. Ikeda, H. Kitagawa, K. Kato and M. Takata, Nat. Mater. 8 (2009) 476. (b) S. Ohkoshi, Y. Tsunobuchi, T. Matsuda, K. Hashimoto, A. Namai, F. Hakoe and H. Tokoro, Nat. Chem. 2 (2010) 539.

Chapter 4

Tailoring the lithium-ion conductivity of Li_2OHBr by substitution of bromine to other halogens

4.1 Introduction

Oxide-based all-solid-state batteries (SSBs) are expected to be next-generation rechargeable batteries both with high energy density and safety. Although various kinds of high Li^+ conductive solid electrolytes have been reported, most of them are hard and fragile ceramics [1]. Therefore, a serious problem is hindering to develop advanced SSBs with a high power density and a low-resistive electrode-solid electrolyte interface. Conventional sintering often provides a resistive mutual diffusion layer around the interface during the sintering process because both electrodes and solid electrolytes are composed of different elements with different concentrations. Thus, the strategy is to develop a soft solid electrolyte.

Recently, Li-rich anti-perovskite (LiRAP) type Li^+-conductive solid electrolyte has been intensively investigated as a soft solid electrolyte [2,3]. It has been reported that the LiRAP, Li_2OHBr, was synthesized at room temperature just by a dry ball milling method in chapter 2. The resultant Li_2OHBr formed cubic-phase, and its total ionic conductivity at 25 ˚C (σ_{25}) was 1.1×10^{-6} S cm^{-1} with the apparent activation energy of 0.54 eV [4]. These data were in good agreement with the previous reports in which LiRAP were synthesized through grinding and heating at a temperature range of 300 - 500 ˚C and showed σ_{25} 1.0×10^{-6} S cm^{-1} and activation energy 0.56 eV [5-8].

Investigating halogen dependence (including mixed-halogen system) often gives great insight to improve the ionic conductivity of solid electrolytes [9,10]. The bottleneck size of the Li-conducting path, as well as lattice constant, plays an important role. Thus, mixing halogen, that is, tuning the lattice constant, would be one effective method to improve ionic conductivity

for LiRAP. Z. Deng *et al.* has investigated ionic conductivities of $Li_3OCl_{1-x}Br_x$ (x = 0, 0.25, 0.5, 0.75, and 1) by *ab initio* molecular dynamics simulations [11]. They have reported that bulk ionic conductivity depended upon the value of x and the maximum value of 4.0×10^{-2} S cm^{-1} was expected for $Li_3OCl_{0.75}Br_{0.25}$ with an activation energy of 0.34 eV. The increase in the ionic conductivity was due to the increase of lattice constant of $Li_3OCl_{0.75}Br_{0.25}$ to 3.970 Å from 3.890 Å, which corresponds to pristine Li_3OCl. A larger conduction path helped to lower the migration barriers between the Li vacancies thus, increasing the ionic conductivity. Also, a report from E. Ahiavi *et al.* shows that by using larger halide ions in the Na_3OX (X = Br, Cl, I, BH_4) system, the lattice constant increased and thereby helped to improve the ionic conductivity [12].

In this chapter, various types of mixed-halogen compounds, $Li_2OHBr_{1-x}X_x$ (X = Cl, I and x = 0–1), were synthesized by the dry ball milling process in order to investigate the relationship between lattice constant and ionic conductivity in this class of materials. First, solid-solution formation ranges and lattice constants were investigated based on synchrotron X-ray diffraction (SXRD) analysis. Then, the effects of mixed-halogen species on the total ionic conductivities were investigated by alternating current (ac) impedance measurements.

4.2 Experimental

The typical synthesis method was based on our previous report on Li_2OHBr [4]. The inorganic precursors used in this work were lithium bromide (LiBr, >99%, Kanto Chemical), lithium chloride (LiCl, >99%, Wako Chemical), lithium iodide (LiI, >99%, Wako Chemical), and lithium hydroxide monohydrate ($LiOH \cdot H_2O$, >99%, Fluka). $LiOH \cdot H_2O$ was heated at 200 ˚C for 20 hours to form LiOH. 10 mmol of LiOH and a total 10 mmol of a mixture of LiBr and LiX were loaded into a 12 mL zirconia ball milling jar with 15 g of 5 mm zirconia balls and sealed inside the glove box filled with dry Ar gas with a dew point lower than –70 ˚C. Here the

amounts of LiBr and LiX were controlled according to the following chemical reaction (1). The ball-milling (Fritsch, planetary micro mill Pulverisette 7) was carried out at room temperature for 48 hours at 700 RPM.

$LiOH + (1\text{-}x)\ LiBr + x\ LiX = Li_2OHBr_{1-x}X_x$ …… (1)
(X = Cl, I and x = 0–1)

The SXRD measurements were carried out at beamline BL5S2 of AichiSR with synchrotron radiation of 1.033 Å using the two-dimensional detector PILATUS 100K. The samples were sealed in soda-lime glass capillaries (0.5 mm in diameter) in a dry Air-filled glove box with a dew point lower than –70 ˚C. The lattice constants of the samples were calculated by the Le Bail method.

For electrochemical impedance spectroscopy (EIS) measurements an impedance analyzer (BioLogic, VMP3) was used. The powdered samples were pressed into a pellet with a diameter of 7 mm at 5.1×10^2 MPa for 5 minutes inside a dry Ar-filled glove box with dew point lower than –70 ˚C, with gold foils (2.5 μm in thickness) on both sides as current collectors. The EIS of this Au symmetrical blocking electrode cell was measured in the frequency range of 500 kHz–100 mHz with an ac amplitude of 25 mV at 25, 50, 75, and 100 ˚C.

4.3 Result and Discussion

Figure 4.1 shows the SXRD patterns of synthesized $Li_2OHBr_{1-x}X_x$. Li_2OHBr, the end member of Br, formed a single phase of the cubic anti-perovskite structure with a lattice constant of 4.046 Å as with our previous report[4]. In Cl-substituted samples ($Li_2OHBr_{1-x}Cl_x$), the diffractions from the cubic phase were observed up to x = 1, and the peaks shifted to a higher angle with increasing x due to the substitution of smaller Cl^- (1.81Å) with Br^- (1.96 Å) [13]. However, some unreacted starting materials of lithium halides were also observed in the Cl-rich region, especially in Li_2OHCl with the end member of Cl. To determine the solid solution range, lattice constants were calculated and plotted against x in Figure 4.2(a). The

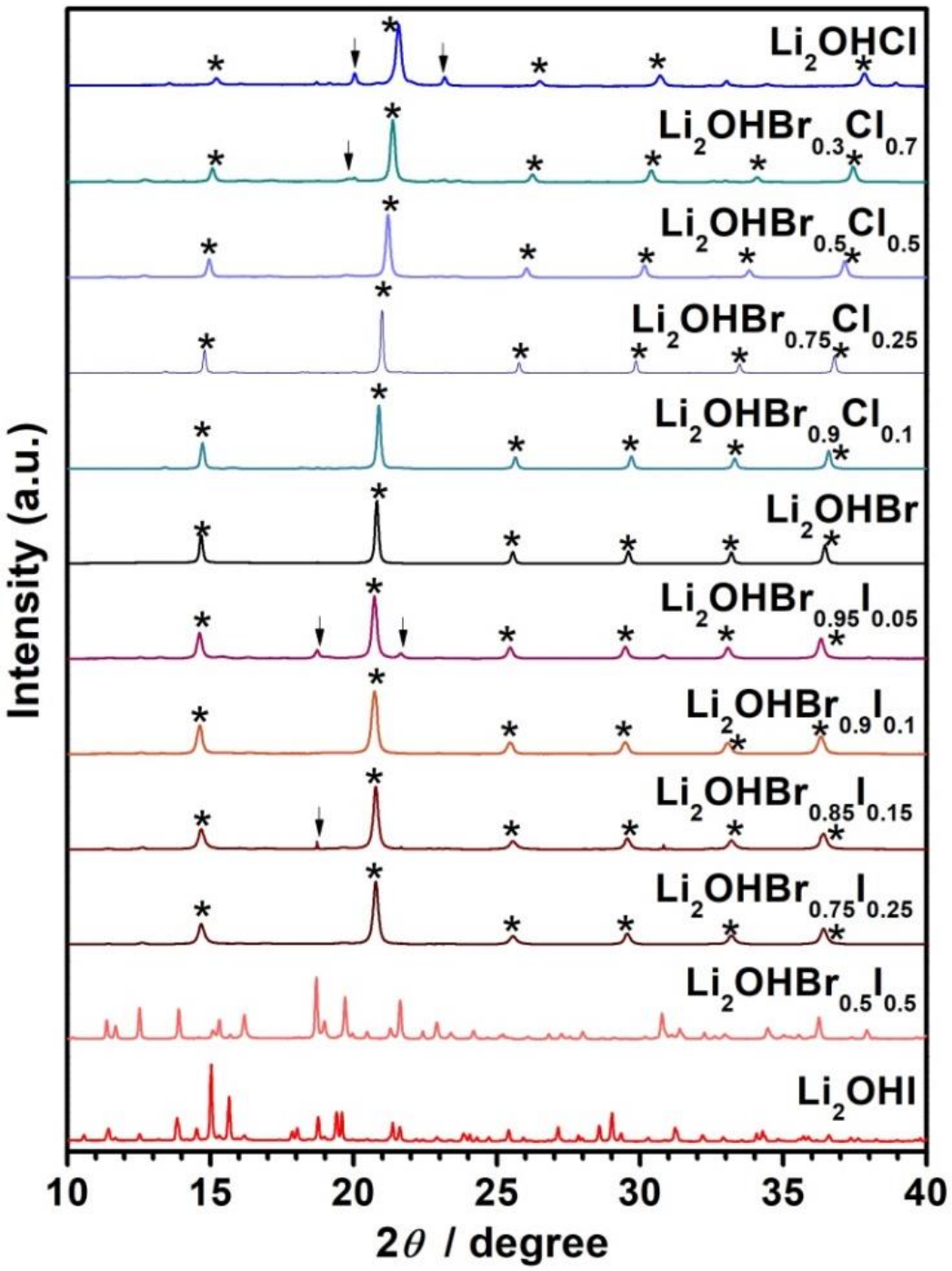

Figure 4.1 SXRD patterns of $Li_2OHBr_{1-x}X_x$ (X = Cl, I). * denotes the diffraction peaks from the cubic anti-perovskite structure and ↓ denotes the unreacted starting materials.

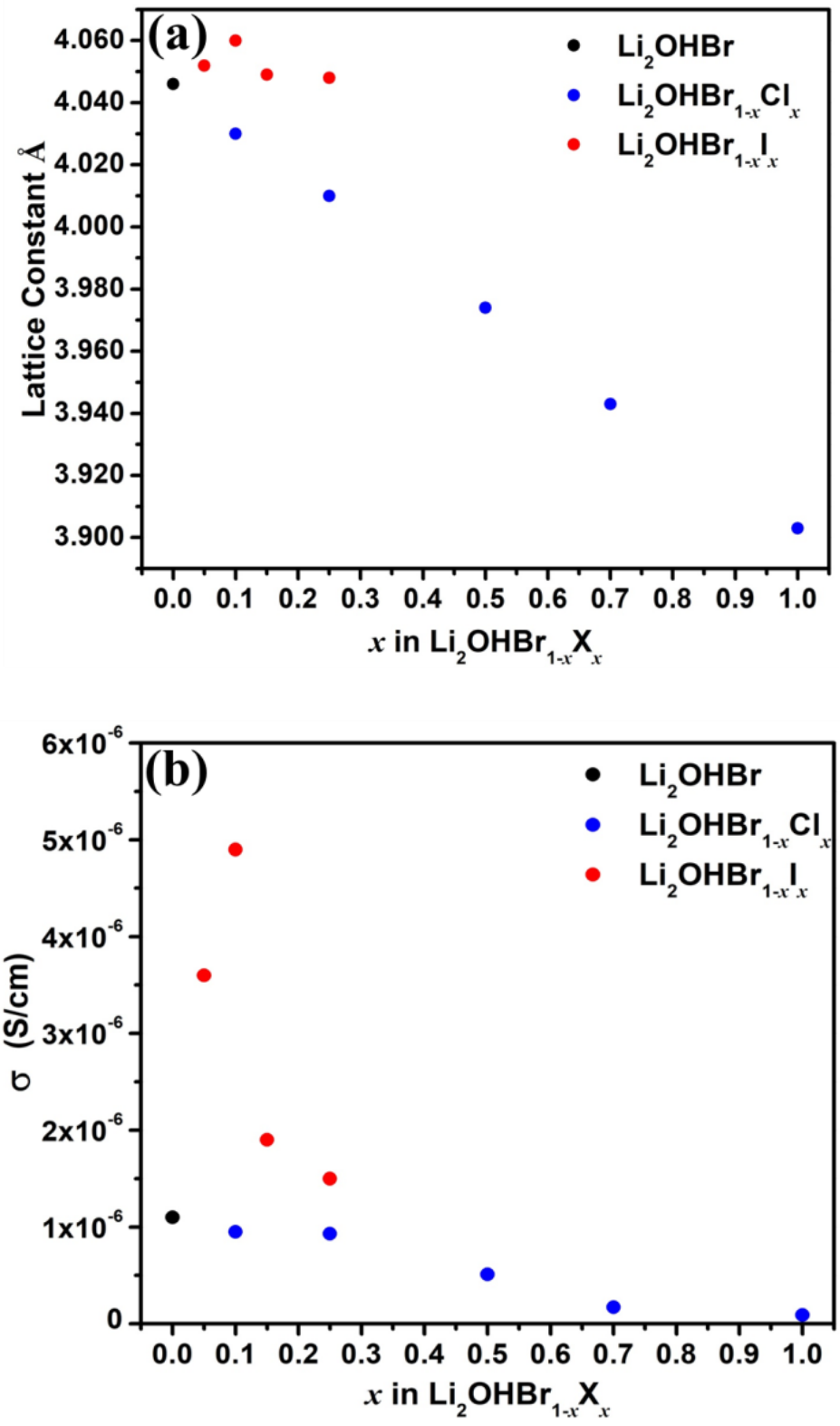

Figure 4.2 (a) Variation of the lattice constant and **(b)** total ionic conductivity (σ) at 25 ˚C with *x* in $Li_2OHBr_{1-x}X_x$ (X = Cl, I).

lattice constant of Li_2OHCl (3.903 Å) well fitted with the reported value [14], and the lattice constant change was linear against *x*. These results strongly suggest the formation of a solid solution of $Li_2OHBr_{1-x}Cl_x$ in the whole *x* range. The reason for the existence of unreacted starting materials in Cl-rich samples is speculated to be insufficient reaction time during the ball milling process.

In SXRD patterns of I-substituted samples ($Li_2OHBr_{1-x}I_x$), the cubic phase was observed up to $x = 0.25$, and complicated patterns were observed above $x = 0.5$ (Figure 4.1). This suggests the solid solution formation range was up to $x = 0.25$. Considering a larger ionic radius of I^- (2.20 Å) than that of Br^- (1.96 Å) [13], the lattice constant should be expanded with increasing *x*. However, according to Figure 4.2 (a), the lattice constant monotonically increased from $x = 0$ (4.046 Å) up to $x = 0.1$ (4.060 Å) whereas the lattice constants of $x = 0.15$ (4.049 Å) and 0.25 (4.048 Å) were smaller than $x = 0.05$ (4.052 Å). The origin of this unnatural shrinkage is still unclear at the current stage, but it can be concluded that the solid solution range was up to $x = 0.1$, and the samples with $x = 0.15$ and 0.25 do not form solid solution from the viewpoint of lattice constant.

To investigate the halogen-mixing effects on ionic conductivity, EIS measurements were conducted using Au/$Li_2OHBr_{1-x}X_x$/Au symmetrical cells, and the resultant Nyquist plots measured at 25 ˚C are shown in Figure 4.3(a). All the samples show one semicircular arc in the frequency range of 10^5–10^1 Hz, which can be regarded as total (bulk and grain boundary) resistance. The total ionic conductivity was calculated from this total resistance based on pellet thickness and diameter and plotted against *x* in Figure 4.2 (b). The total ionic conductivity decreased for the $Li_2OHBr_{1-x}X_x$ with X = Cl samples, whereas the total ionic conductivity increased for the $Li_2OHBr_{1-x}X_x$ with X = I when compared to the original Li_2OHBr. $Li_2OHBr_{0.9}I_{0.1}$ shows the highest total ionic conductivity of 4.9×10^{-6} S cm^{-1} at 25 ˚C among $Li_2OHBr_{1-x}Cl_x$ samples have a smaller lattice constant and lower ionic conductivity than

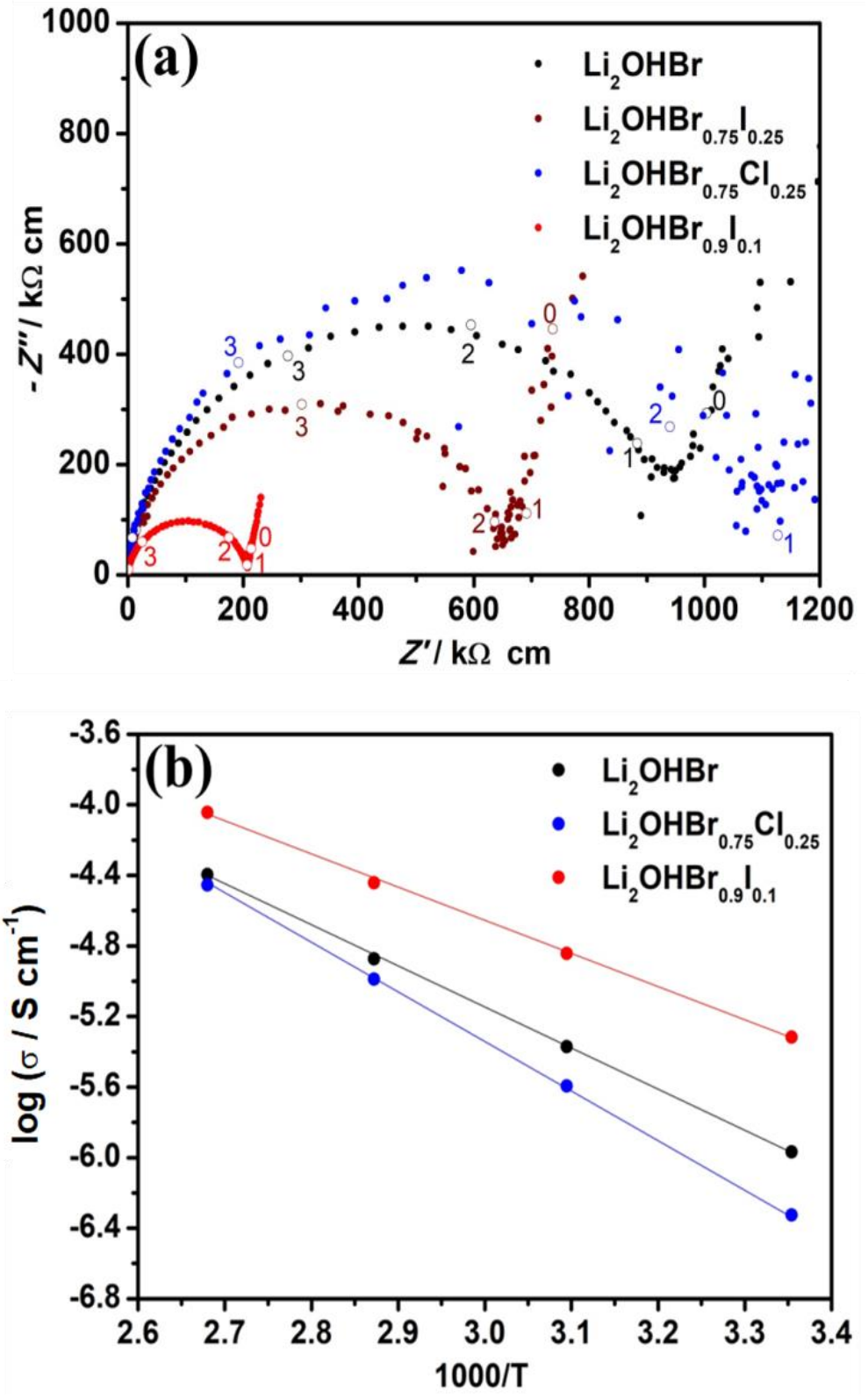

Figure 4.3 (a) Nyquist plots of Au / $Li_2OHBr_{1-x}X_x$ / Au symmetrical (X = Cl, I) cell measured at 25 ˚C. The numbers in the plot denotes the frequency 10^n and **(b)** Arrhenius plot of log (σ) versus 1000/T of $Li_2OHBr_{1-x}X_x$ (X = Cl, I).

pristine Li_2OHBr. Hence, it can be expected that the ionic conductivity of this class of materials is affected by a lattice constant. Figure 4.4 shows the variation of total ionic conductivity against lattice constant. A clear tendency was observed that samples with larger lattice constant showed higher ionic conductivity. To confirm this tendency from the viewpoint of activation energy, the apparent activation energies were calculated from the slope of the Arrhenius plots in Figure 4.3(b). The apparent activation energy of Li_2OHBr, $Li_2OHBr_{0.75}Cl_{0.25,}$ and $Li_2OHBr_{0.9}I_{0.1}$ samples were 0.54, 0.59, and 0.41 eV, respectively. Then, the apparent activation energy also follows the tendency of the ionic conductivity, which can be correlated to the variation of the lattice constant.

Halogen-mixing effects on $Li_3OCl_{1-x}Br_x$ were computationally investigated by Deng *et al*. [11]. According to their *ab initio* molecular dynamics simulation, higher Li^+ conductivity was expected by mixing a small amount of larger Br^-. Moreover, very recently, a similar tendency to our $Li_2OHBr_{1-x}X_x$ system was reported in sodium-ion conducting anti-perovskites Na_3OX (X = Cl, Br, I and BH_4) [12]. E. Ahiavi *et al.* also reported that lattice constant played an important role in ionic conduction in this class of materials. They explained this tendency by using halogens of different sizes to modify the lattice constant and improve the Na-ion conductivity. In this work, 10% substitution of Br with I in Li_2OHBr helped to increase the lattice constant, indicating the widening of the bottleneck of ion conduction channels [15]. Hence, a wider migration pathway resulted in an enhanced Li^+ conductivity with a lower activation barrier and thus improved the total ionic conductivity of the $Li_2OHBr_{0.9}I_{0.1}$ sample c.a. 4 fold when compared to the pristine Li_2OHBr sample.

The crystallinity of materials also often becomes one of the factors affecting ionic conductivity, so the crystallite sizes of $Li_2OHBr_{1-x}X_x$ were calculated using 110 diffraction peaks, observed around 21˚ in Figure 4.1 by Scherrer's equation. The positive correlation between crystallite size and total ionic conductivity was observed in both $Li_2OHBr_{1-x}Cl_x$ and

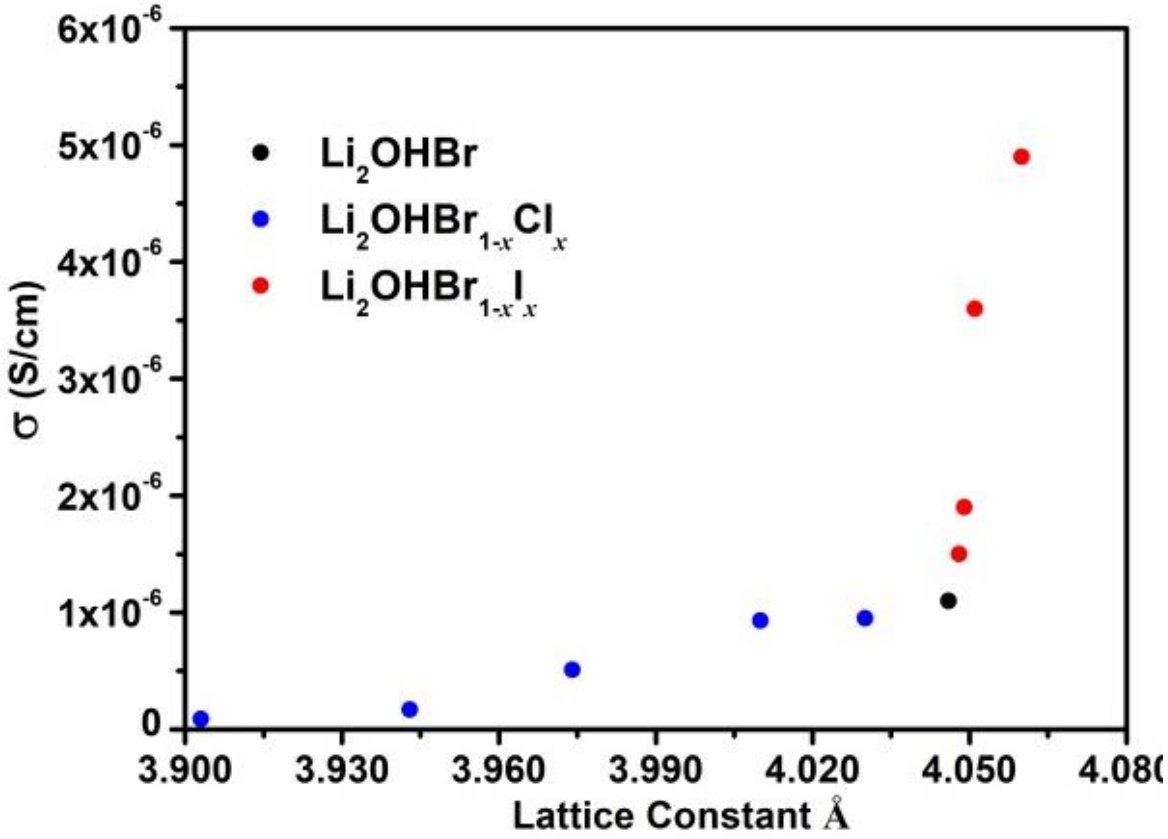

Figure 4.4 Change in total ionic conductivity (σ) at 25 ˚C with respect to the lattice constant (Å).

$Li_2OHBr_{1-x}I_x$ systems.However, comparing these two systems, $Li_2OHBr_{1-x}I_x$ samples have larger total ionic conductivity even when their crystallite sizes were smaller than those of $Li_2OHBr_{1-x}Cl_x$ samples. The author suggests that the effect of crystallinity is not a dominant factor for determining the total ionic conductivity of this class of material.

4.4 Conclusion

In summary, the author has investigated the solid solution formation range and ionic conductivity of $Li_2OHBr_{1-x}X_x$ (X = Cl, I) and found that $Li_2OHBr_{0.9}I_{0.1}$ had the largest lattice constant of 4.060 Å and σ_{25} of 4.9×10^{-6} S cm^{-1} which is an improvement from $\sigma_{25} = 1.1 \times 10^{-6}$ S cm^{-1} of pure Li_2OHBr sample. Therefore, the ionic conductivity was successfully improved by synthesizing mixed halogen $Li_2OHBr_{1-x}X_x$ samples by room temperature synthesis. Also, it was found that the lattice constant played a vital role in determining ionic conductivity. The larger the lattice constant was, the higher the ionic conductivity. This large lattice constant was achieved by mixing a small amount of larger monovalent anion I^- (2.20 Å) in the place of smaller Br^- (1.96 Å) in Li_2OHBr to form $Li_2OHBr_{1-x}I_x$. Further, more advanced characterization methods are required to study how lattice constant influence the tuning of ionic conductivity with higher accuracy and create a more comprehensive and accurate designing principle for ionic conductors.

References

1) Z. Zhang, Y. Shao, B. Lotsch, Y. S. Hu, H. Li, J. Janek, L. F. Nazar, C. W. Nan, J. Maier, M. Armand and L. Chen, Energy Environ. Sci. 11 (2018) 1945.
2) S. Li, J. Zhu, Y. Wang, J.W. Howard, X. Lü, Y. Li, R.S. Kumar, L. Wang, L.L. Daemen and Y. Zhao, Solid State Ionics 284 (2016) 14.

3) X. Lü, G. Wu, J. W. Howard, A. Chen, Y. Zhao, L. L. Daemen and Q. Jia, Chem. Commun. 50 (2014) 11520.

4) M. K. Sugumar, T. Yamamoto, M. Motoyama and Y. Iriyama, Solid State Ionics 349 (2020) 115298.

5) Y. Li, W. Zhou, S. Xin, S. Li, J. Zhu, X. Lu, Z. Cui, Q. Jia, J. Zhou, Y. Zhao and J.B. Goodenough, Angew. Chem. Int. Ed. 55 (2016) 9965.

6) Z.D. Hood, H. Wang, A.S. Pandian, J.K. Keum and C. Liang, J. Am. Chem. Soc. 138 (2016) 1768.

7) P. Hartwig, A. Rabeau and W. Weppner, J. Less Common Met. 78 (1981) 227.

8) A.-Y. Song, Y. Xiao, Dr. K. Turcheniuk, P. Upadhya, A. Ramanujapuram, J. Benson, A. Magasinski, M. Olguin, L. Meda, O. Borodin and G. Yushin, Adv. Energy Mater. 8 (2018) 1700971.

9) S. Yubuchi, M. Uematsu, M. Deguchi, A. Hayashi and M. Tatsumisago, ACS Appl. Energy Mater. 1 (2018) 3622.

10) Y. Wang, Q. Wang, Z. Liu, Z. Zhou, S. Li, J. Zhu, R. Zou, Y. Wang, J. Lin, and Y. Zhao, J. Power Sources 293 (2015) 735.

11) Z. Deng, B. Radhakrishnan, and S. P. Ong, Chem. Mater. 27 (2015) 37.

12) E. Ahiavi, J. A. Dawson, U. Kudu, M. Courty, M. S. Islam, O. Clemens, C. Masquelier and T. Famprikis, J. Power Sources 471 (2020) 1228489.

13) Y. Ida, Phys. Earth Planet. Inter. 13 (1976) 97.

14) T. Yamamoto, H. Shiba, N. Mitsukuchi, M. K. Sugumar, M. Motoyama and Y. Iriyama, Inorg. Chem. 59 (2020) 11901.

15) Z. Deng, M. Ou, J. Wan, S. Li, Y. Li, Y. Zhang, Z. Deng, J. Xu, Y. Qiu, Y. Liu, C. Fang, Q. Li, L. Huang, J. Zhu, S. Han, J. Han and Y. Zhao, Chem. Mater. 32 (2020) 8827.

Chapter 5

Preparation of Li-excess and Li-deficient anti-perovskite structured $Li_{2+x}OH_{1-x}Br$ and their effects on total ionic conductivity

5.1 Introduction

All-solid-state Li batteries (ASSBs) are considered to be promising rechargeable batteries compared to the conventional lithium-ion (Li^+) batteries using liquid electrolytes because the ASSBs have potential advantages on safety, thermal stability, and high energy density. Many efforts have been devoted to develop soft and high Li^+ conductive solid electrolytes (SEs) for ASSBs. This is because those SEs are processing friendly for developing large-sized ASSBs requiring charge-discharge reactions at high current densities. Various kinds of soft SEs have been investigated, such as oxide [1,2,3], sulfide [4,5,6], halide [7,8,9], etc., and some of them have superior ionic conductivity to conventional liquid electrolytes [10,11,12].

Among them, lithium-rich anti-perovskite (LiRAP) structured SEs, Li_3OY (Y = Cl, Br), has been reported as a high Li^+ conductive soft SE with 1×10^{-3} S cm^{-1} at 25 °C [13]. However, according to later works, these LiRAP can contain hydrogen, and practical compositions are $Li_{3-x}OH_xY$ in many cases [14]. Neutron diffraction analysis has revealed that H occupies beside O and forms rotating OH unit but does not occupy Li site in the hydrated LiRAP [15]. This hydrogen incorporation decreases the carrier density of Li^+. On the other hand, such an OH unit has been proposed to assist Li^+ conduction in LiRAP, where short and fast rotating O–H bonds provide extra space to form Frenkel defects and then improve Li^+ mobility [15]. Consequently, in Li_2OHCl, the total Li^+ conductivity (σ_t) depends on the Li-H exchanging

amount, and the σ_t increased with increasing the H amount [15]. Although the σ_t is affected by other factors, these results indicate that controlling the hydrogen amount is crucial in obtaining the highest Li^+ conductivity in LiRAP. However, most of the past reports show that the preparation method requires heating to a temperature ranging from 240 ˚C to 500 ˚C during the fabrication process of LiRAP, and then control of hydrogen amount was not easy because hydrogen can be removed as H_2O at high temperature [7,8,16-18].

We have previously reported that Li_2OHBr was successfully prepared just by dry ball-milling of LiOH and LiBr at room temperature [19]. This preparation method does not require any heating process, which will be beneficial to control hydrogen amount in the LiRAP. The resultant compound obtained σ_t of 1.1×10^{-6} S cm^{-1} at 25 ˚C with an apparent activation energy of 0.54 eV. We have applied this method to prepare halogen-exchanged Li_2OHBr and found that a larger lattice constant is an influential factor to improve σ_t [20].

This work reports that Li-H exchanged $Li_{2+x}OH_{1-x}Br$ samples are prepared by dry ball-milling of LiOH, $LiOH \cdot H_2O$, Li_2O, and LiBr at room temperature. Both Li-excess ($x > 0$) and Li-deficient ($x < 0$) samples are systematically synthesized, and the effect of x in $Li_{2+x}OH_{1-x}Br$ on σ_t is investigated focusing on the variation of lattice constant and average crystallite size. Series of Li-excess compounds show volcano-type conductivity changes against x, and $Li_{2.2}OH_{0.8}Br$ has the highest σ_t of 3.6×10^{-6} S cm^{-1}, which is three times larger value than that of Li_2OHBr. Neutron diffraction analysis confirms the hydrogen occupation in the lattice, and the refined composition is almost consistent with the prepared composition.

5.2 Experimental

The room temperature synthesis method was followed based on our previous report on Li_2OHBr [19]. Lithium hydroxide monohydrate ($LiOH \cdot H_2O$, >99%, Fluka), lithium bromide (LiBr, >99%, Kanto Chemical), and lithium oxide (Li_2O, >99%, Wako Chemicals) were used

as the starting material. $LiOH \cdot H_2O$ was heated at 200 ˚C for 20 hours under Ar atmosphere in a furnace attached to glove box (dew point < –80 °C) to prepare dehydrated LiOH. The starting materials were ball-milled (Fritsch, planetary micro mill Pulverisette 7) at room temperature in a zirconia bowl with 15 g of 5 mm zirconia balls at a rotation speed of 700 RPM for 48 hours in Ar atmosphere. Li-excess $Li_{2+x}OH_{1-x}Br$ (x = 0, 0.05, 0.1, 0.15, 0.2, 0.25, 0.3, 0.35, 0.4) were prepared by following scheme (1), while Li-deficient $Li_{2+x}OH_{1-x}Br$ (x = –0.5, –0.2) were prepared by following scheme (2).

$(1-x)LiOH + LiBr + x\ Li_2O \rightarrow Li_{2+x}OH_{1-x}Br$ …… (1)

$(1+2x)LiOH - x\ LiOH \cdot H_2O + LiBr \rightarrow Li_{2+x}OH_{1-x}Br$ …… (2)

The crystal structure of all the $Li_{2+x}OH_{1-x}Br$ samples was analyzed by synchrotron powder X-ray diffraction (SXRD) measurements (BL5S2 of Aichi Synchrotron Radiation Center) with wavelength λ = 1.033 Å. The powder samples were sealed in soda-lime glass capillaries (0.5 mm in diameter) in an Ar-filled glove box (dew point < –80 ˚C), and the measurements were carried out between 10–40˚ using two-dimensional detector PILATUS 100K. The lattice constant of each sample was calculated by the Le Bail method. Also, the average crystallite size of each sample was calculated by Scherrer's equation (3),

$$D = \frac{K\lambda}{\beta \cos\theta} \quad \ldots (3)$$

where D is average crystallite size, K is shape factor (here 0.9 is adopted), λ is the X-ray wavelength, β is full width at half a maximum of diffraction peak, and θ is Bragg angle. Also, the neutron diffraction patterns of both Li_2OHBr and $Li_{2.2}OH_{0.8}Br$ samples were collected at BL21 of the Materials and Life Science Experimental Facility in the Japan Proton Accelerator Research Complex (J-PARC). Each 180 mg of sample was filled in a cylindrical vanadium container (3.00 mm of diameter and 0.10 mm of thickness). The data was collected with a 500 kW beam for 6 h at RT. Averaged crystal structure refinements over a lattice spacing range of

0.7–4.5 Å for neutron diffraction at a backscattering detector bank were performed by Rietveld refinement using the computer program Z-Rietveld [21,22].

Electrochemical impedance spectroscopy (EIS) was carried out using an impedance analyzer (BioLogic, VMP3) to investigate σ_t of the $Li_{2+x}OH_{1-x}Br$ samples. The $Li_{2+x}OH_{1-x}Br$ powder samples were pressed into a pellet with a diameter of 7 mm at 5.1×10^2 MPa for 5 minutes inside a dry Ar-filled glove box (dew point < –80 °C), with gold foils (2.5 μm in thickness with a diameter of 7mm) on both sides as current collectors. The density of each pellet was estimated to be over 90% in each sample. The EIS of Au symmetrical cells was measured in the frequency range of 500 kHz–100 mHz with an AC amplitude of 25 mV at 25, 50, 75, and 100 ˚C.

5.3 Results and Discussion

Figure 5.1(a) shows the SXRD patterns of $Li_{2+x}OH_{1-x}Br$ (x = –0.5 ~ +0.4), where simulated diffraction peaks from Li_2OHBr are also plotted as a reference. Diffraction patterns from the samples with x = –0.5 ~ +0.35 were assigned to cubic-phased anti-perovskite structure, though a tiny amount of unreacted LiBr were detected as impurity peaks as shown by *. On the other hand, the sample with x = +0.4 provided distorted peaks indicating the formation of another phase. These results suggest that a single-phase is formed between x = –0.5 to +0.35. Figure 5.1(b) shows the magnified diffraction peaks of 2θ = 20 – 21.5°. The 011 diffraction peak has shifted to a lower angle with the increase in x, indicating that the lattice constant tends to increase with x.

Figure 5.2(a) summarizes the variation of lattice constant with x in $Li_{2+x}OH_{1-x}Br$. The lattice constant tends to increase with increasing the x. The lattice constant for the Li-excess samples followed a straight line against x, indicating that a solid solution is formed in these compounds. The lattice constant of the Li-deficient samples also followed a straight line, but the slope was

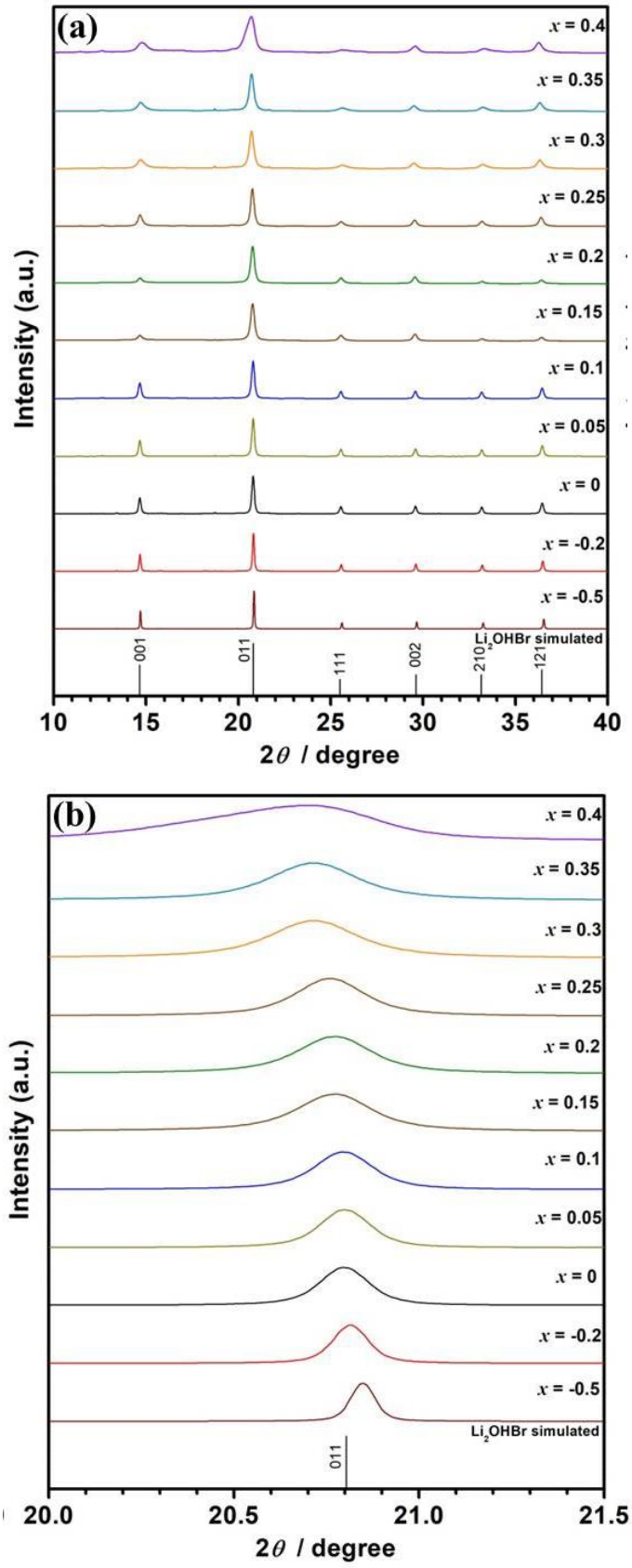

Figure 5.1 (a) Synchrotron PXRD patterns of $Li_{2+x}OH_{1-x}Br$ (x = –0.5 ~ +0.4) and **(b)** Synchrotron PXRD patterns of $Li_{2+x}OH_{1-x}Br$ between 2θ = 20 and 21.5. * denotes the diffraction peaks from LiBr.

different from those with Li-excess one, and then slight distortion to tetragonal or orthorhombic phase may take place in the Li-deficient samples. Figure 5.2(b) shows the variation of average crystallite size with x in $Li_{2+x}OH_{1-x}Br$. These crystallite sizes were calculated from the 011 diffraction peak by using Scherrer's equation. The crystallite size tended to decrease with the increase of x, and Li-excess samples were formed as a few tens of nano-sized grains. These results indicate that a larger amount of grain boundaries are included with an increase in x.

Figure 5.3(a) shows the Nyquist plots of Au/$Li_{2+x}OH_{1-x}Br$ (x = –0.5, –0.2, 0, +0.1, +0.2, and +0.3)/Au symmetrical cells measured at 25 ˚C. Each spectrum was composed of one semicircular arc at a higher frequency region (> 100 Hz) and a capacitive straight line at the lower frequency region. Here, both the real axis (Z') and imaginary axis (– Z'') were normalized with both electrode area and thickness of each pellet. The σ_t at 25 ℃ was estimated from the diameter of the semicircular arc, and the value was measured at different temperatures.

Figure 5.3(b) summarized the variation of σ_t for $Li_{2+x}OH_{1-x}Br$ (x = −0.5, −0.2, 0, +0.1, +0.2, and +0.3). The σ_t of Li_2OHBr (x = 0) was 1.1 ×10^{-6} S cm^{-1}. In the case of Li-excess samples, the σ_t sensitively varied with x. The σ_t increased with x up to x = +0.2 and achieved the maximum value of 3.6 × 10^{-6} S cm^{-1}, but further increasing of x, in turn, decreased the σ_t, and the value of $Li_{2.3}OH_{0.7}OBr$ 1.4 × 10^{-6} S cm^{-1}. On the other hand, in the case of Li-deficient samples, the σ_t decreased with decreasing the x, and the $Li_{1.5}OH_{1.5}OBr$ had the lowest σ_t of 3.4 × 10^{-7} S cm^{-1}. These results clarify that the σ_t depends on the Li-H exchange amount. Figure 5.3(c) shows the temperature dependency of σ_t for Li-excess and Li- deficient samples. All the samples showed Arrhenius-type variation, and the lowest apparent activation energy of 0.50 eV was achieved for $Li_{2.2}OH_{0.8}Br$, while the highest value of 0.59 eV for $Li_{1.5}OH_{1.5}Br$.

Figures 5.4(a) and (b) show the neutron diffraction patterns of Li_2OHBr and $Li_{2.2}OH_{0.8}Br$, respectively. Both samples contain a slight amount (less than 0.5 mol%) of impurities from unreacted LiBr, but most of the peaks were well-fitted to cubic-phase anti-

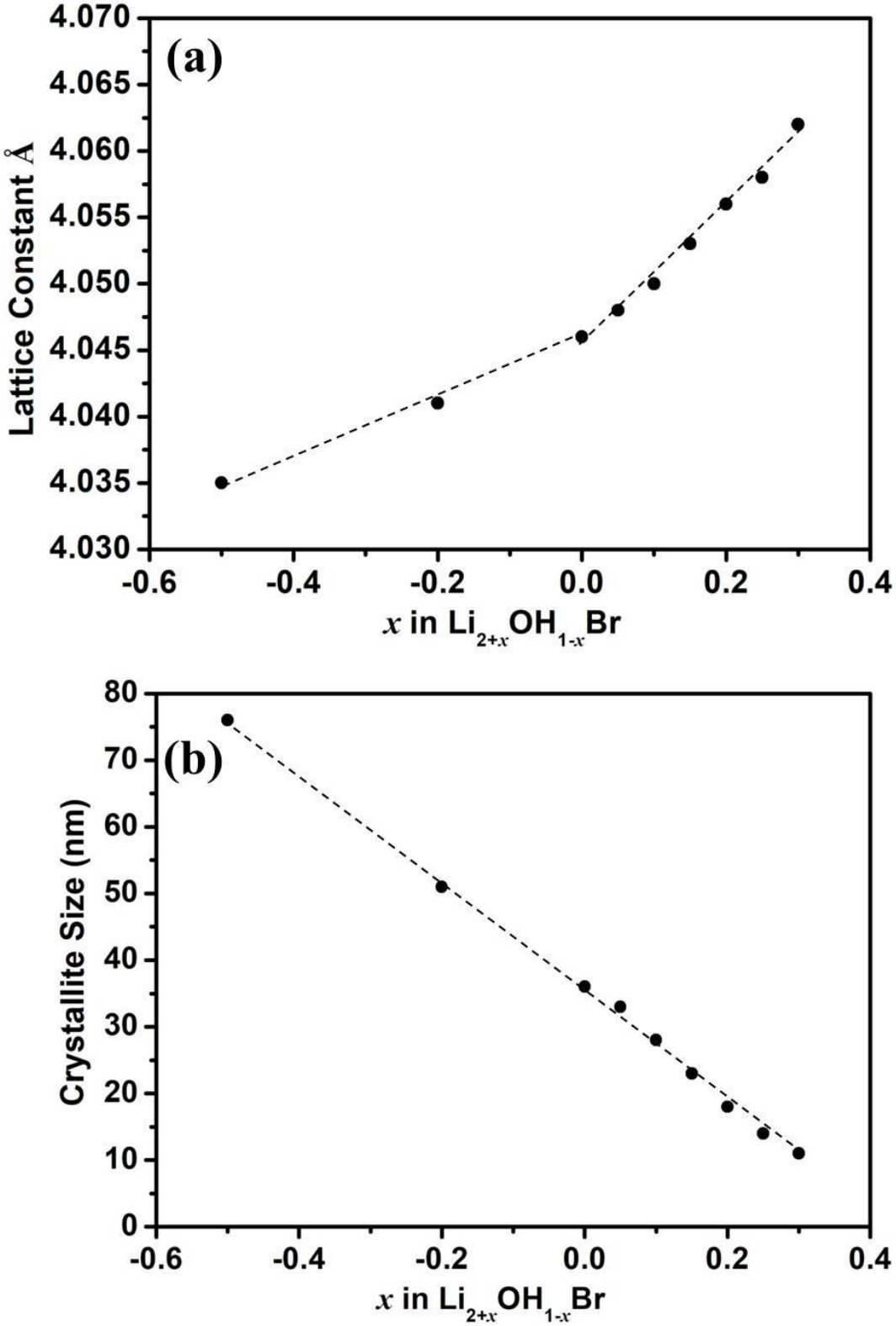

Figure 5.2 (a) Variation of lattice constant of $Li_{2+x}OH_{1-x}Br$ (x = –0.5 ~ +0.3) and **(b)** Variation of crystallite size of $Li_{2+x}OH_{1-x}Br$ (x = –0.5 ~ +0.3).

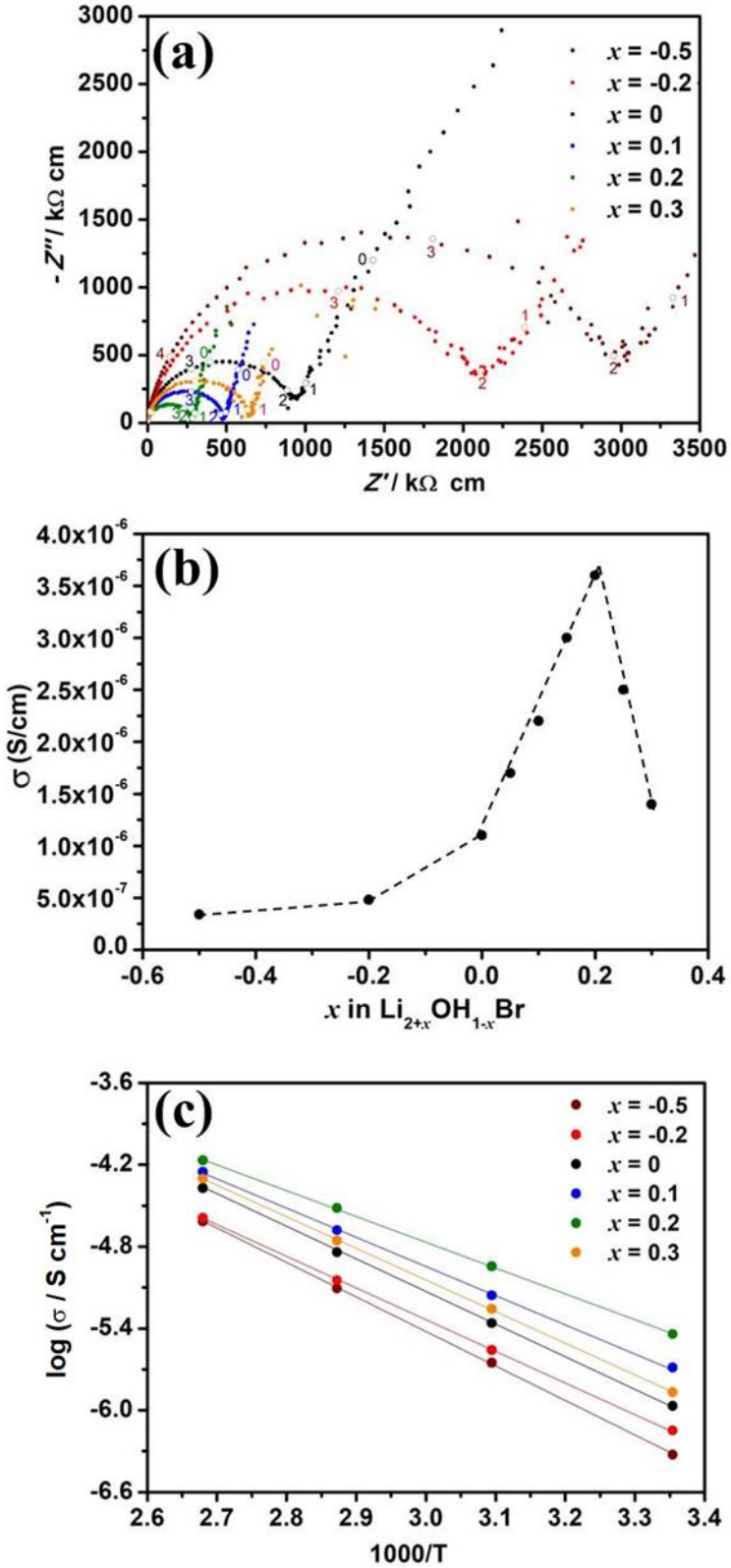

Figure 5.3 (a) Nyquist plots of $Li_{2+x}OH_{1-x}Br$ (x = –0.5, –0.2, 0, +0.1, +0.2 and +0.3) measured at 25 °C. The numbers in the plot denotes the frequency 10^n, **(b)** Variation of total ionic conductivity at 25 °C of $Li_{2+x}OH_{1-x}Br$ (x = –0.5 ~ +0.3) and **(c)** Arrhenius plots of $Li_{2+x}OH_{1-x}Br$ (x = –0.5, –0.2, 0, +0.1, +0.2 and +0.3).

perovskite structure (space group $Pm\bar{3}m$; No. 221). The refined compositions of pristine Li_2OHBr and $Li_{2.2}OH_{0.8}Br$ by Rietveld analysis were $Li_{1.9}OH_{0.9}Br$ and $Li_{2.2}OH_{0.7}Br$, respectively. These results indicate that the refined composition is almost consistent with the expected value from starting material. Also, these findings clarify that the hydrogen occupies beside O, which is in good agreement with the past report of Li_2OHCl [14]. A slightly deviated composition from electroneutrality in the refined composition may be derived from the experimental and analytical uncertainty using hydrogen (H) [15].

It was found that the Li-excess samples have advantages against Li-deficient samples to improve σ_t of $Li_{2+x}OH_{1-x}Br$. Li-excess samples increase both lithium carrier density and lattice constant linearly with x. These will be positive factors to increase σ_t based on the increased lithium carrier density in addition to reducing the activation energy for in-grain Li^+ conduction. On the other hand, Li-excess samples have negative factors in decreasing the σ_t based on reducing the number of OH rotational units in addition to increasing the grain boundary resistance due to its smaller crystallite size. The author considers that this trade-off provides a volcano-type dependency of ionic conductivity for x as shown in Fig. 3(b), and the $Li_{2.2}OH_{0.8}Br$ (x = +0.2) was optimized against σ_t. On the other hand, in the case of Li_2OHCl, σ_t has increased in the Li-deficient samples even though the lattice constant has been reduced [15]. Those opposite trends of σ_t against Li-H exchanging amount suggest that OH rotation assists to Li^+ conduction in LiRAP depend on the lattice constant and that this OH rotation assist does not play effectively in Li_2OHBr with a larger lattice constant. In fact, the $Li_{2.2}OH_{0.8}Br$ obtains σ_t of 3.6×10^{-6} S cm^{-1}, same with $Li_2OHBr_{0.95}I_{0.05}$, though the $Li_{2.2}OH_{0.8}Br$ has a slightly larger lattice constant of 4.056 Å than $Li_2OHBr_{0.95}I_{0.05}$, 4.054 Å, in addition to containing a larger OH unit concentration [20]. This OH-rotation has been reported to provide extra space to form Frenkel defects and then improve σ_t in Li_2OHCl, but that may not effectively assist Li^+ conductivity in Li_2OHBr due to its larger lattice constant. Therefore,

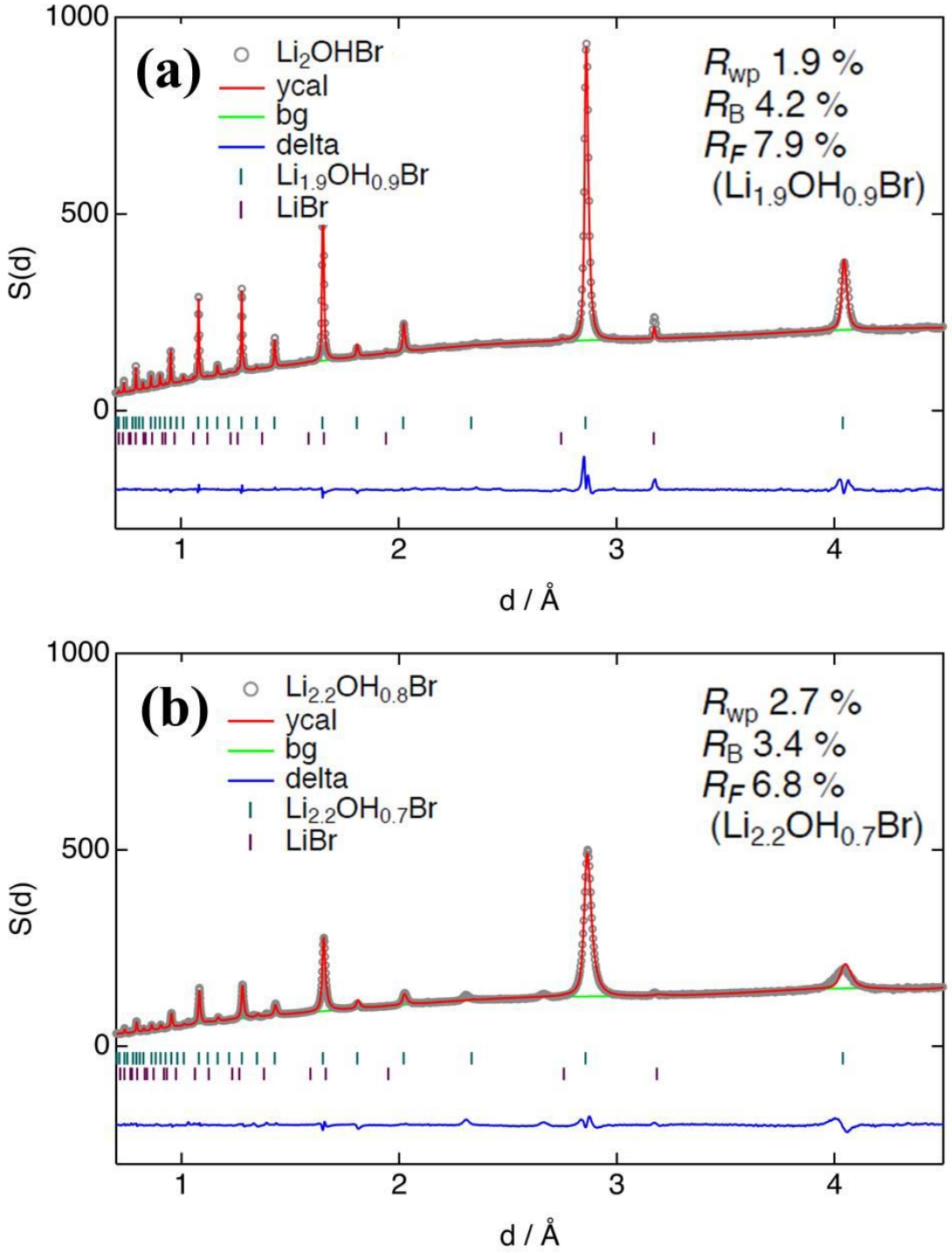

Figure 5.4 The Rietveld refinement results of **(a)** Li_2OHBr (R_{wp} = 1.9%) and **(b)** $Li_{2.2}OH_{0.8}Br$ (R_{wp} = 2.7%), which are normalized to the profiles of the vanadium standard sample and the background. The observed, calculated, background and difference between observed and calculated patterns are indicated as circles, red, green and blue lines, respectively. The Bragg reflection positions are shown for Li_2OHBr and LiBr.

it is understood that a vital factor in improving σ_t is the lattice constant in the case of Li_2OHBr, and Li-excess samples provide a larger lattice constant, improving the σ_t. Thus, the reduction of σ_t at $0.2 < x$ may arise from the increase of grain boundary resistance due to the decrease of crystallite size of LiRAP [23].

5.4 Conclusion

The author systematically synthesized Li-H exchanged $Li_{2+x}OH_{1-x}Br$ ($x = -0.5 \sim +0.4$) by applying the room temperature ball-milling method. The σ_t sensitively changed for Li-excess samples ($0 < x$), and the highest ionic conductivity of 3.6×10^{-6} S cm^{-1} was achieved at 25 ℃ for the composition of $Li_{2.2}OH_{0.8}Br$ ($x = +0.2$). This optimization will arise from the trade-off between positive effects (higher lithium carrier density and larger lattice constant) and negative effects (smaller amounts of OH rotating unit and larger amount of grain boundary resistance). Controlling the hydrogen amount will be an essential factor in improving the σ_t of LiRAP and ensuring structural stability.

References

(1) V. Thangadurai and W. Weppner, Ionics 12 (2006) 81.

(2) P. Knauth, Solid State Ionics 180 (2009) 911.

(3) S. Ohta, T. Kobayashi, J. Seki and T. Asaoka, J. Power Sources 202 (2012) 332.

(4) A. Sakuda, A. Hayashi and M. Tatsumisago, Sci. Rep. 3 (2013) 2261.

(5) X. Ji and L. F. Nazar. J. Mater. Chem. 20 (2010) 9821.

(6) F. Wu, W. Fitzhugh, L. Ye, J. Ning and X. Li, Nat. Commun. 9 (2018) 4037.

(7) T. Asano, A. Sakai, S. Ouchi, M. Sakaida, A. Miyazaki and S. Hasegawa, Adv. Mater. 30 (2018) 1803075.

(8) X. Ji, J. Liang, X. Yang, K. R. Adair, C. Wang, F. Zhao and X. Sun, Energy Environ. Sci. 13 (2020) 1429.

(9) K. H. Park, K. Kaup, A. Assoud, Q. Zhang, X. Wu and L. F. Nazar, ACS Energy Lett. 5 (2020) 533.

(10) N. Kamaya, K. Homma, Y. Yamakawa, M. Hirayama, R. Kanno, M. Yonemura, T. Kamiyama, Y. Kato, S. Hama, K. Kawamoto and A. Mitsui, Nat. Mater. 10 (2011) 682.

(11) Y. Sun, K. Suzuki, S. Hori, M. Hirayama and R. Kanno, Chem. Mater. 29 (2017) 5858.

(12) W. Huang, L. Cheng, S. Hori, K. Suzuki, M. Yonemura, M. Hirayama and R. Kanno, Mater. Adv. 1 (2020) 334.

(13) Y. Zhao and L.L. Daemen, J. Am, Chem. Soc. 134 (2012) 15042.

(14) S. Li, J. Zhu, Y. Wang, J.W. Howard, X. Lü, Y. Li, R.S. Kumar, L. Wang, L.L. Daemen and Y. Zhao, Solid State Ionics 284 (2016) 14.

(15) A.-Y. Song, Y. Xiao, Dr.K. Turcheniuk, P. Upadhya, A. Ramanujapuram, J. Benson, A. Magasinski, M. Olguin, L. Meda, O. Borodin and G. Yushin, Adv. Energy Mater. 8 (2018) 1700971.

(16) Y. Li, W. Zhou, S. Xin, S. Li, J. Zhu, X. Lu, Z. Cui, Q. Jia, J. Zhou, Y. Zhao and J.B. Goodenough, Angew. Chem. Int. Ed. 55 (2016) 9965.

(17) Z.D. Hood, H. Wang, A.S. Pandian, J.K. Keum and C. Liang, J. Am. Chem. Soc. 138 (2016) 1768.

(18) P. Hartwig, A. Rabeau and W. Weppner, J. Less Common Met. 78 (1981) 227.

(19) M. K. Sugumar, T. Yamamoto, M. Motoyama and Y. Iriyama, Solid State Ionics 349 (2020) 115298.

(20) M. K. Sugumar, T. Yamamoto, M. Motoyama and Y. Iriyama, Chem. Lett. 50 (2021) 448.

(21) R. Oishi, M. Yonemura, Y. Nishimaki, S. Torii, A. Hoshikawa, T. Ishigaki, T. Morishima, K. Mori and T. Kamiyama, Nucl. Instr. Meth. 600 (2009) 94.

(22) R. Oishi-Tomiyasu, M. Yonemura, T. Morishima, A. Hoshikawa, S. Torii, T. Ishigaki and T. Kamiyama, J. Appl. Crystallogr. 45 (2012) 299.

(23) J. A. Dawson, P. Canepa, T. Famprikis, C. Masquelier and M. S. Islam, J. Am. Chem. Soc. 140 (2018) 362.

6. General conclusion

ASSBs are promising options for next-generation batteries. In order to consider ASSBs as a suitable replacement for the current LIBs in electric vehicles, the energy density and other technical challenges must be resolved. The development of high-energy-density ASSBs requires advanced solid electrolytes for optimum performance with high safety features. The design of high Li^+ conductive SEs should consider both electrochemical stability and cost-effective easy preparation technique. The present work focuses on easy and simple synthesis techniques to prepare Li^+ conducting anti-perovskite structured solid electrolytes and different optimizations carried out to improve its Li^+ conductivity.

Initially, cubic-phase phased anti-perovskite-structured Li_2OHBr is synthesized successfully at room temperature by just the dry ball-milling method. The total ionic conductivity of the Li_2OHBr is estimated to be 1.1×10^{-6} S cm^{-1} at 25 ˚C. In addition, cubic-phased Li_2OHCl is formed at room temperature by just the dry ball-milling method, and it shows one order higher ionic conductivity at 25 ˚C than that of the thermodynamically stable orthorhombic Li_2OHCl formed through heating-cooling cycle between 30-200 ˚C. In order to improve the total ionic conductivity of Li_2OHBr, mixed halogen $Li_2OHBr_{1-x}X_x$ (X = Cl, I) is synthesized by the same room temperature process. $Li_2OHBr_{0.9}I_{0.1}$ shows a larger lattice constant of 4.060 Å with improved total ionic conductivity of 4.9×10^{-6} S cm^{-1} at 25 ˚C. The lattice constant increase is due to large I^- (2.20 Å) replacing the small Br^- (1.96 Å). In another attempt to increase the ionic conductivity, $Li_{2+x}OH_{1-x}Br$ samples are prepared by the same room temperature ball-milling process. The total ionic conductivity increased for the Li-excess $Li_{2.2}OH_{0.8}Br$ sample to 3.6×10^{-6} S cm^{-1} at 25 ℃. Thus, ionic conductivity optimization needs to consider the following parameters like lattice constant, lithium carrier density, and amount of OH. Controlling and tuning the above parameters plays an important role in improving the total ionic conductivity of LiRAP and ensures structural stability.

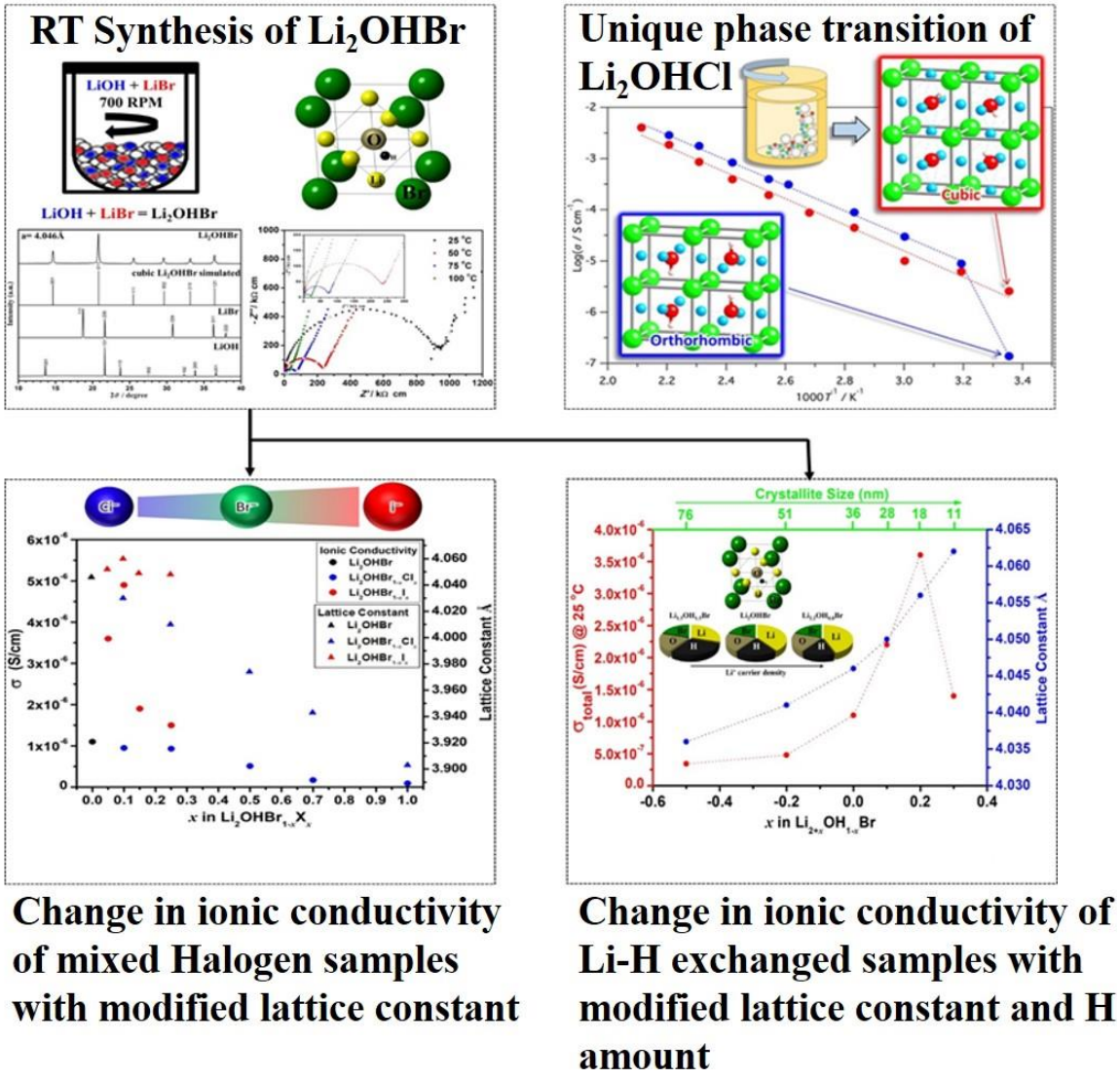

Change in ionic conductivity of mixed Halogen samples with modified lattice constant

Change in ionic conductivity of Li-H exchanged samples with modified lattice constant and H amount

Li_2OHBr forms stable cubic phase anti-perovskite structure whereas, in Li_2OHCl, there is a possibility of forming orthorhombic phase or mixed phase. Hence, further Li^+ conductivity improvement studies were carried out using Li_2OHBr.

7. Publications and Conferences list

Publications

1. Room temperature synthesis of anti-perovskite structured Li_2OHBr

M. K. Sugumar, T. Yamamoto, M. Motoyama and Y. Iriyama

Solid State Ionics, 2020, 349, 115298. (Chapter 2)

2. Synthesis of the Metastable Cubic Phase of Li_2OHCl by a Mechanochemical Method

T. Yamamoto, H. Shiba, N. Mitsukuchi, M. K. Sugumar, M. Motoyama and Y. Iriyama,

Inorganic Chemistry., 2020, 59, 11901–11904. (Chapter 3)

3. Tailoring the Lithium-ion Conductivity of Li_2OHBr by Substitution of Bromine with Other Halogens

M. K. Sugumar, T. Yamamoto, M. Motoyama and Y. Iriyama

Chemistry Letters, 2021, 50, 448–451. (Chapter 4)

4. Preparation of Li-excess and Li-deficient anti-perovskite structured $Li_{2+x}OH_{1-x}Br$ and their effects on total ionic conductivity

M. K. Sugumar, T. Yamamoto, K. Ikeda, M. Motoyama and Y. Iriyama

ACS Applied Energy Materials, under review (Chapter 5)

Conference presentations

1. Novel approach on room temperature synthesis of anti-perovskite structured Li_2OHBr

2nd World Conference on Solid Electrolytes for Advanced Applications: Garnets and Competitors

Shizuoka, Japan, 23-27 September 2019, poster

2. Room Temperature Synthesis of Anti-Perovskite Structured Li^+ - conductive Solid Electrolyte

The 87th Electrochemical Society of Japan Spring Meeting.

Nagoya (Online), Japan, 17-19 March 2020, oral

3. Mechanochemical Synthesis of Modified Li_2OHBr to Improve Ionic Conductivity

The Ceramic Society of Japan: The 33rd Fall Meeting

Sapporo (Online), Japan, 02-04 September 2020, oral

4. Mechanochemical Synthesis of Modified Li_2OHBr to Improve Ionic Conductivity

The Electrochemical Society: PRiME 2020

Hawaii (Online), USA, 04-09 October 2020, poster

8. Acknowledgement

I would like to express my deep gratitude to my research supervisor Prof. Yasutoshi Iriyama for giving me an opportunity to work in his research lab. His valuable guidance and constructive comments during the course of the period during my doctoral studies are greatly appreciable. I also thank my co-supervisor, Dr. Takayuki Yamamoto, Dr. Munekazu Motoyama, and Dr. Norikazu Ishigaki for their valuable inputs during my doctoral research. I would like to thank Prof. Takahisa Yamamoto and Prof. Tomokazu Fukutsuka for their guidance and support. I am grateful to all the office staff and my colleagues Mr. Yasuhiro Suzuki and Mrs. Miyuki Sakakura at Nagoya University, for their support during my doctoral course. It was also a great pleasure to work with my fellow labmates in Prof. Iriyama research lab, who have helped me in one way or another: Mr. Yuki Tanaka, Mr. Kota Urabe, Ms. Hinata Shiba, Mr. Keisuke Yoshikawa, Mr. Ryo Shiraishi, Mr. Yuki Nishinaka, Mr. Tomoki Fuji, Mr. Hajime Tamura, and Mr. Satoshi Yamamoto. I thank Aichi Synchrotron Radiation Center and National Institute for Materials Science (NIMS) Battery Research Platform for providing the materials characterization facilities. I also thank Dr. Kazutaka Ikeda, High Energy Accelerator Research Organization (KEK), for helping with the Neutron Diffraction measurement facility. I also extend my thanks to the Yoshida Scholarship Foundation for the award of the "YKK Leaders 21" Scholarship for financial support.

I genuinely thank Prof. Ramaswamy Murugan, Department of Physics, Pondicherry University, for being a great support. I am very much thankful to my Parents, Sister, and Brother-in-law for giving me this opportunity and for their constant support. I also extend my thanks to my lab mates of Prof. Murugan's lab for their support. I also thank my relatives and friends for encouraging me. All my praises will always be to GOD for giving me the strength to complete my Doctoral Course successfully.

Manoj Krishna Sugumar